2021

Global neural rhythm control by local neuromodula

BOSTON UNIVERSITY

COLLEGE OF ENGINEERING

Dissertation

GLOBAL NEURAL RHYTHM CONTROL BY

LOCAL NEUROMODULATION

by

ERIK ANDREW ROBERTS

B.S., University of California San Diego, 2012

Submitted in partial fulfillment of the

requirements for the degree of

Doctor of Philosophy

2019

Approved by

First Reader
_____

Nancy J. Kopell, Ph.D.
Professor of Mathematics & Statistics
Professor of Pharmacology & Experimental Therapeutics

Second Reader
_____

Michelle M. McCarthy, M.D., Ph.D.
Research Assistant Professor of Mathematics & Statistics

Third Reader
_____

Kamal Sen, Ph.D.
Associate Professor of Biomedical Engineering

Fourth Reader
_____

John A. White, Ph.D.
Professor and Chair of Biomedical Engineering

Fifth Reader
_____

Emery N. Brown, M.D., Ph.D.
Edward Hood Taplin Professor of Computational Neuroscience
and Health Sciences & Technology
Massachusetts Institute of Technology
Warren M. Zapol Professor of Anaesthesia
Harvard Medical School

Acknowledgments

There are many folks to whom I owe a debt of gratitude to for generously providing mentorship during my graduate training. My thesis advisor, Nancy Kopell, taught me the value of collaborative science and the mindset of a computational neuroscientist. Both she and Michelle McCarthy provided essential guidance as well as words of encouragement. My rotation and coursework with Uri Eden taught me the language and skills of statistics. These proved immensely useful during the collaboration I had with Xue Han and her post-doctoral researcher Krishnakanth Kondabolu. They supplemented my computational training with an understanding of the methods and culture of animal-based research.

I am also grateful for all the fruitful discussions I have had with members of the Kopell group, both regarding projects and neurophilosophy in general. Jason Sherfey created our modeling tool, DynaSim, and shared great wisdom about the philosophy of neural modeling. Austin Soplata taught me the jedi-like arts of being a computational "power user," the importance of open-source software, and how to use DynaSim. Benjamin Pittman-Polletta provided great insights about mathematical concepts. Dave Stanley created the Multi-Dimensional Dictionary (MDD) for Matlab, which formed the foundational datatype for my GIMBL-Vis toolbox. Most of all, I am thankful to have them as lifelong friends and colleagues.

iv

GLOBAL NEURAL RHYTHM CONTROL BY

LOCAL NEUROMODULATION

ERIK ANDREW ROBERTS

Boston University, College of Engineering, 2019
Ph.D. degree requirements completed in 2019
Dual M.D./Ph.D. degrees expected in 2021

Major Professor: Nancy J. Kopell, Ph.D.
Professor of Mathematics & Statistics
Professor of Pharmacology & Experimental
Therapeutics

ABSTRACT

Neural oscillations are a ubiquitous form of neural activity seen across scales and modalities. These neural rhythms correlate with diverse cognitive functions and brain states. One mechanism for changing the oscillatory dynamics of large neuronal populations is through neuromodulator activity. An intriguing phenomenon explored here is when local neuromodulation of a distinct neuron type within a single brain nucleus exerts a powerful influence on global cortical rhythms.

One approach to investigate the impact of local circuits on global rhythms is through optogenetic techniques. My first project involves the statistical analysis of electrophysiological recordings of an optogenetically-mediated Parkinsonian phenotype. Empirical studies demonstrate that Parkinsonian motor deficits correlate with the emergence of exaggerated beta frequency (15-30 Hz) oscillations throughout the cortico-basal ganglia-thalamic network. However, the mechanism of these aberrant oscillatory dynamics is not well understood. A previous modeling study predicted that

cholinergic neuromodulation of medium spiny neurons in the striatum of the basal ganglia may mediate the pathologic beta rhythm. Here, this hypothesis was tested using selective optogenetic stimulation of striatal cholinergic interneurons in normal mice; stimulation robustly and reversibly amplified beta oscillations and Parkinsonian motor symptoms.

The modulation of global rhythms by local networks was further studied using computational modeling in the context of intrathalamic neuromodulation. While intrathalamic vasoactive intestinal peptide (VIP) is known to cause long-lasting excitation *in vitro*, its *in vivo* dynamical effects have not been reported. Here, biophysical computational models were used to elucidate the impact of VIP on thalamocortical dynamics during sleep and propofol general anesthesia. The modeling results suggest that VIP can form robust sleep spindle oscillations and control aspects of sleep architecture through a novel homeostatic mechanism. This homeostatic mechanism would be inhibited by general anesthesia, representing a new mechanism contributing to anesthetic-induced loss of consciousness.

While the previous two projects differed in their use of empirical versus theoretical methods, a challenge common to both domains is the difficulty in visualizing and analyzing large multi-dimensional datasets. A tool to mitigate these issues is introduced here: GIMBL-Vis is a Graphical Interactive Multi-dimensional extensiBLe Visualization toolbox for Matlab. This toolbox simplifies the process of exploring multi-dimensional data in Matlab by providing a graphical interface for visualization and analysis. Furthermore, it provides an extensible open platform for distributed development by the community.

Contents

4   GIMBL-Vis: a Graphical Interactive Multi-dimensional extensiBLe Visualization Toolbox for Matlab   121

List of Tables

List of Figures

List of Abbreviations

AC	....	Adenylate Cyclase
ACh	....	Acetylcholine
Ca	....	Calcium
cAMP	....	Cyclic Adenosine Monophosphate
CBT	....	Cortico-Basal ganglia-Thalamic [circuit]
CMT	....	Centromedial Thalamus
CTC	....	Communication-Through-Coherence [hypothesis]
E	....	Excitatory [cortical neuron]
EEG	....	Electroencephalogram
EPSP	....	Excitatory Post-Synaptic Potential
FS	....	Fast-Spiking [cortical interneuron]
g[Ch]	....	Conductance of [an Ion Channel]
GABA	....	Gamma-Aminobutyric Acid
GUI	....	Graphical User Interface
GV	....	GIMBL-Vis
I	....	Inhibitory [cortical interneuron]
IPSP	....	Inhibitory Post-Synaptic Potential
K	....	Potassium
LFP	....	Local Field Potential
LTS	....	Low-Threshold Spike
M1	....	Primary Motor Cortex
MUA	....	Multi-Unit Activity
NREM	....	Non-Rapid Eye Movement [sleep]
PACAP	....	Pituitary Adenylate Cyclase-Activating Polypeptide
PD	....	Parkinson's Disease
PDE	....	Phosphodiesterase
PHI	....	Peptide Histidine Isoleucine
PRC	....	Phase Response Curve
PSP	....	Post-Synaptic Potential
REM	....	Rapid Eye Movement [sleep]
RS	....	Regular Spiking [cortical pyramidal neuron]
SChI	....	Striatal Cholinergic Interneuron
SEM	....	Standard Error of the Mean
SUA	....	Single-Unit Activity

TC   . . . .   Thalamocortical [relay neuron]
TRN   . . . .   Thalamic Reticular Nucleus
VIP   . . . .   Vasoactive Intestinal Peptide

Chapter 1

Introduction

1.1 Neural Rhythms

Neural rhythms are a ubiquitous form of neural activity seen across scales and modalities. While neurons are commonly thought of and statistically modeled as randomly firing, the average rate of spiking activity may be modulated rhythmically (Kramer and Eden, 2016). In addition to single cell rhythms, neurons can synchronize activity such that the average population spiking activity has oscillatory features (Buzsaki, 2006). Neural electrical activity can be recorded extracellularly at different locations, including within the brain and on the scalp, corresponding to the local field potential (LFP) and electroencephalogram (EEG), respectively. These signals are thought to correspond to a transformed summation of membrane voltage potentials from many individual neurons during synaptic and spiking activity (Buzsaki et al., 2012). The oscillatory components of these signals are commonly examined using a power spectrum, involving a Fourier transform from the time to frequency domain. Neural rhythms are revealed as peaks at different frequency bands in the power spectrum.

1.1.1 Cognitive Rhythms

Many neural rhythms correlate with diverse cognitive functions, brain states, or disease symptoms (Traub and Whittington, 2010)—those of the first category are often referred to as cognitive rhythms. For example, transient basal ganglia beta (15–30 Hz) rhythms occur during specific phases of animal behavioral tasks (Leventhal et al.,

2012; Feingold et al., 2015; Schmidt et al., 2013). In contrast, the exaggerated beta oscillations discussed in chapter 2 correlate with the motor deficits of Parkinson's Disease and diminish with common treatments (Brown, 2007; Little et al., 2012).

Since the function and relevance of neural rhythms is still debated, important questions are: (1) what mechanisms underly these rhythms; and (2) do these mechanisms represent physiology useful for cognitive functions.

Some proposed mechanisms of rhythm generation have been described directly in terms of neuronal biophysics and neurophysiology. For example, the thalamocortical neurons of chapter 3 generate a bursting delta (1–4 Hz) rhythm from the interaction between the hyperpolarization-activated non-selective cation HCN channels and the transient T-type calcium channels. Based on their input-output transfer function relationship and downstream effects (Sherman, 2001), these thalamocortical bursts are thought to be important for awake attention and memory consolidation during sleep (Llinas and Steriade, 2006).

1.2   Neuromodulation

Neuromodulators provide an effective means to alter the activity of large cell populations, including neural rhythms. Furthermore, they can do so over longer periods of time than the temporospatially precise neurotransmitters. While the synaptic *neurotransmitters* typically act as ligands for ionic transmembrane receptors that trigger immediate ionic currents, *neuromodulators* release from both synaptic and extrasynaptic sources and tend to activate metabotropic receptors; these receptors trigger indirect effects through amplifying second messenger cascades that can affect various aspects of cellular function, from gene transcription to ion channel conductance. Note that some ligands can serve as either neurotransmitters or neuromodulators, depending on the source and receptor type (e.g., glutamate and epinephrine). Neuromodula-

tors include norepinephrine, dopamine, serotonin, acetylcholine (ACh), and vasoactive intestinal peptide (VIP). The latter two modulate M-current and H-current, and are studied in chapters 2 and 3, respectively.

An intriguing phenomenon explored here is when local neuromodulation, potentially of a distinct neuron type, within a single brain nucleus exerts a powerful influence on global cortical rhythms. In particular, chapter 2 describes how the interaction between acetylcholine and M-current forms a mechanism to generate beta oscillations in the cortico-basal ganglia-thalamic (CBT) circuit. Chapter 3 discusses how VIP may transform the thalamocortical delta (1–4 Hz) rhythm to an alpha (8–12 Hz) rhythm by modulating H-current.

1.2.1   Optogenetics

In the past, neuromodulation was studied via techniques like pharmacologic infusions combined with implanted electrode recordings. These methods suffered from imprecise spatial control, as drugs would spread to neighboring areas and affect multiple cell types. In addition, the experiments were temporally imprecise since the drugs diffuse for a variable amount of time before an effect is seen. Furthermore, effects persist even after termination of infusion, until the drugs are metabolized. Precise temporospatial control became possible with the introduction of optogenetics (Boyden et al., 2005; Kondabolu et al., 2015). This technique involves the expression of light-sensitive ion channels, analogous to those found in the retina, in a cell type of interest using viral or transgenic means of gene delivery. Light is delivered to activate the new ion channels in a region of interest. Excitatory or inhibitory effects are possible depending on the type of channel expressed. Unlike pharmacologic techniques, optogenetics can control cells of a specified type with millisecond precision over a small volume. Thus, one approach to investigate the impact of local circuits on global rhythms is through optogenetic techniques.

1.2.2 Experimental Optogenetics Study: Parkinsonism and the Intrinsic Striatal Acetylcholine System

Chapter 2 describes how optogenetics was used to modulate acetylcholine in the striatum of the basal ganglia in order to create a Parkinsonian phenotype. Empirical studies demonstrate that Parkinsonian motor deficits correlate with the emergence of exaggerated beta frequency (15-30 Hz) oscillations throughout the cortico-basal ganglia-thalamic network. However, the mechanism of these aberrant oscillatory dynamics is not well understood. A previous modeling study predicted that cholinergic neuromodulation of medium spiny neurons in the striatum of the basal ganglia may mediate the pathologic beta rhythm. Here, this hypothesis was tested using selective optogenetic stimulation of striatal cholinergic interneurons in normal mice. My role was to analyze the electrophysiological recordings. Stimulation robustly and reversibly amplified beta oscillations and Parkinsonian motor symptoms.

1.3 Theoretical Models

Theoretical computational models provide another method to study neuromodulation, explored in chapter 3.

1.3.1 Biophysical Modeling

In general, a model is an abstraction of a feature of the real world. Biophysical models utilize techniques from physics to simulate aspects of biology. Given the breadth of physics and biology, there are many types of biophysical models, including systems biology models of intracellular networks, finite element models of tissues to whole bodies (Roberts et al., 2011), and protein folding models. Within the context of neuroscience, models span the scale of nanometers to centimeters, ranging from neurotransmitter release at single synapses to the dynamics of whole brains. Within

the scope of neural networks, models range in complexity from neural mass models of average population firing rates to linear integrate-and-fire point neurons to whole brain networks of multi-compartment Hodgkin-Huxley style conductance-based neurons with morphology derived from electron microscopy data.

The model of interest in chapter 3 is one of intermediate complexity: synaptically-connected single-compartment Hodgkin-Huxley style conductance-based point neurons, the most parsimonious spiking neuron model with parameters that represent measurable biophysical quantities. These models are conductance-based in the sense that they derive from a resistor-capacitor (RC) electrical circuit representation of the neuron's electrical activity. This type of model was used by Hodgkin and Huxley to describe the flow of electrical current through the squid giant axon and led to a Nobel prize in 1963 (Hodgkin and Huxley, 1952). It is called a "point" neuron because it does not explicitly model volume in its equations. Instead, the model has the simplification of being composed of one of more points or compartments. A small number of compartments is commonly used to model proximal versus distal synapses. However, a large number of compartments approaches a more realistic representation of volume with current flowing through various branches in the neural morphology.

Mathematically, conductance-based point neurons are composed of systems of ordinary differential equations that must be solved numerically. In contrast, models with continuous volume representation are composed of partial differential equations of much greater complexity and parameterization, and hence are more challenging to parameterize accurately and simulate.

Note on Statistical Models

There is great interest today across domains in statistical models, e.g. deep learning. Statistical models can be useful for summarizing data and making decisions, but they often lack interpretability. Even if interpretable, they tend to summarize correlative

features but do not provide the mechanistic insights that biophysical models can. Thus, there is a role for them in experimental science, but it is one that does not substitute for biophysical models.

1.3.2 Harmony of Theory and Empiricism

While empiricism is the cornerstone of modern science, experimental investigations often yield surprising or unexpected results with unclear mechanisms. Biophysical computational models can provide desirable explanatory power for these elusive mechanisms. Different experimental conditions and manipulations can be tested computationally, yielding a range of predictions. These predictions can then be tested experimentally, leading to new insights and validation of the theoretical mechanism. Thus, an effective way to study vexing scientific problems is to use a collaborative dual process of empirical studies and computational models informing one another with their complementary strengths.

Harmony of Models and Experiments: A Case-Study

An illustrative example of the interplay between theoretical models and empirical studies in neuroscience is the study featured in chapter 2. This empirical investigation was motivated by the predictions from an *in silico* modeling study, supported by preliminary *in vivo* experiments (McCarthy et al., 2011; Pittman-Polletta et al., 2018). Previously, it was known that enhanced beta oscillations correlate with Parkinsonian features (Brown, 2007; Little et al., 2012), but the source and mechanism of beta oscillations was unclear. After synthesizing the results of relevant studies and considering the neural architecture, Michelle McCarthy realized that the core mathematical mechanism of paradoxical anesthetic beta oscillations was applicable to the Parkinsonian beta rhythm. She demonstrated this with the computational modeling study, which was subsequently supported by several experimental studies involving

multiple techniques (McCarthy et al., 2011; Pittman-Polletta et al., 2018).

1.3.3 Biophysical Computational Modeling Study: Dynamic Effects of Intrathalamic VIP in Sleep and Anesthesia

A similar although slightly different process inspired the computational model described in chapter 3. While intrathalamic vasoactive intestinal peptide (VIP) neuromodulation has been known to cause long-lasting excitation *in vitro*, its *in vivo* dynamical effects have not been reported. By combining knowledge of thalamus from other studies and considering VIP's known *in vitro* effects, it was possible to build a biophysical computational model of intrathalamic VIP's effects on thalamocortical dynamics during sleep and propofol general anesthesia. The modeling results suggest that VIP can form robust sleep spindle oscillations and control aspects of sleep architecture through a novel homeostatic mechanism. This homeostatic mechanism would be inhibited by general anesthesia, representing a new mechanism contributing to anesthetic-induced loss of consciousness.

1.4 Software Tools

Several tools were essential to this work. In particular, optogenetics and biophysical modeling are the key methods of chapters 2 and 3, respectively. While these two projects differed in their use of empirical versus theoretical methods, a challenge common to both domains is the difficulty in visualizing and analyzing large multi-dimensional datasets, especially within the Matlab software environment. For example, when developing biophysical models one tests a range of values for different parameters, both to explore different regimes of dynamics and to check the robustness of findings. However, there did not yet exist an efficient Matlab workflow for visualizing the results of model simulations when varying over multiple parameters. To solve this problem, I created GIMBL-Vis: a GUI-based Interactive Multi-dimensional

extensiBLe Visualization toolbox for Matlab (Roberts, 2017). Described in chapter 4, this toolbox simplifies the process of exploring multi-dimensional data in Matlab by providing a graphical interface for visualization and analysis. Furthermore, it provides an extensible open platform for distributed development by the community.

1.5 Summary Overview

This dissertation describes three computational projects which center on the theme global neural rhythm control by local neuromodulation.

Chapter 2 reports the statistical analysis of an experimental dataset involving cholinergic neuromodulation. Specifically, local optogenetic activation of mouse striatal cholinergic interneurons induced a Parkinsonian-like state while globally elevating cortico-basal ganglia-thalamic (CBT) loop beta (15-30 Hz) oscillations characteristic of Parkinson's Disease (Brown, 2007; Little et al., 2012). Since this beta rhythm was reversibly generated in normal mice and transient CBT beta oscillations are associated with normal cognitive function, the exaggerated Parkinsonian beta oscillation is hypothesized to result from the aberration of a normal physiological process due to pathological changes in the neuromodulatory milieu.

Chapter 3 describes a computational model of vasoactive intestinal peptide (VIP) neuromodulation of H-current local to thalamus during sleep and general anesthesia, leading to global changes in cortical rhythms. The modeling results suggest that VIP can form robust sleep spindle oscillations and control aspects of sleep architecture through a novel homeostatic mechanism. This homeostatic mechanism would be inhibited by general anesthesia, representing a new mechanism contributing to anesthetic-induced loss of consciousness.

Chapter 4 introduces GIMBL-Vis, a GUI-based Interactive Multi-dimensional extensiBLe Visualization toolbox for Matlab. This tool supports the visualization and

analysis of the multi-dimensional datasets generated by electrophysiological studies of neuromodulation, whether experimental or computational.

Chapter 2

Optogenetic Activation of Striatal Cholinergic Interneurons

Note: this chapter is derived from a previously published article (Kondabolu et al., 2016).

2.1   Abstract

Cortico-basal ganglia-thalamic (CBT) neural circuits are critical modulators of cognitive and motor function. When compromised, these circuits contribute to neurological and psychiatric disorders, such as Parkinson's disease (PD). In PD, motor deficits correlate with the emergence of exaggerated beta frequency (15–30 Hz) oscillations throughout the CBT network. However, little is known about how specific cell types within individual CBT brain regions support the generation, propagation, and interaction of oscillatory dynamics throughout the CBT circuit or how specific oscillatory dynamics are related to motor function. Here, we investigated the role of striatal cholinergic interneurons (SChIs) in generating beta and gamma oscillations in cortical-striatal circuits. We found that selective stimulation of SChIs via optogenetics in normal mice robustly and reversibly amplified beta and gamma oscillations that are supported by distinct mechanisms within striatal-cortical circuits. Whereas beta oscillations are supported robustly in the striatum and all layers of primary motor cortex (M1) through a muscarinic-receptor mediated mechanism, gamma oscillations are largely restricted to the striatum and the deeper layers of M1. Finally, SChI acti-

vation led to parkinsonian-like motor deficits in otherwise normal mice. These results highlight the important role of striatal cholinergic interneurons in supporting oscillations in the CBT network that are closely related to movement and parkinsonian motor symptoms.

2.2 Introduction

Exaggerated beta oscillations (15–30 Hz) within the cortico-basal ganglia-thalamic (CBT) neural network are putative electrophysiological correlates of bradykinesia and rigidity in Parkinson's disease (PD) (Brown, 2007; Little et al., 2012; Brown and Williams, 2005; Kuhn et al., 2006). Therapies that effectively manage PD motor symptoms, such as dopamine replacement therapy and deep brain stimulation, are associated with a suppression of the exaggerated beta oscillations (Kuhn et al., 2006; Kuhn et al., 2008). Beta oscillations are also found in the CBT circuits of patients with other movement-related disorders, such as epilepsy and dystonia (Herrojo Ruiz et al., 2014; Sochurkova and Rektor, 2003), and in normal, nonhuman primates (Bartolo and Merchant, 2015; Courtemanche et al., 2003) and normal rodents (Leventhal et al., 2012; Berke et al., 2004). Moreover, brief elevations (≤200 ms) of beta oscillations are observed in the basal ganglia of task-performing nonhuman primates and rodents during specific phases of behavioral tasks (Leventhal et al., 2012; Feingold et al., 2015; Schmidt et al., 2013), indicating that beta oscillations may be important for motor and nonmotor functions. In contrast to the regulated temporal variability of beta oscillations in normal motor functions, temporal stability is correlated with the Parkinsonian motor symptoms of bradykinesia and rigidity (Little et al., 2012). Together, these findings suggest that brief epochs of beta oscillations are a normal aspect of basal ganglia dynamics, their temporal modulation is important for movement regulation, and loss of regulation or uncontrolled expression of beta oscillations

may contribute to movement deficits, such as those observed in PD.

Despite the clear link between CBT beta oscillations and movement, the mechanisms underlying their generation remain elusive. Dopamine clearly modulates the generative mechanisms of CBT beta oscillations and beta frequency coherence between CBT structures. A hallmark of PD pathology is chronic reduction of dopamine input to CBT circuits due to midbrain dopaminergic neuron loss. Loss of midbrain dopamine increases beta oscillation power and coherence in PD animal models (Sharott et al., 2005; Mallet et al., 2008). Similarly, acute reduction of dopamine locally in the striatum increases striatal beta oscillations (Costa et al., 2006). Systemic dopaminergic drugs decrease beta oscillation power and coherence in PD patients (Brown et al., 2001), and also increase finely tuned gamma oscillations in the basal ganglia and thalamus, although we know little about the functional significance of these finely tuned gamma oscillations in PD (Brown et al., 2001; Kempf et al., 2009). Because of the dense innervation of the striatum by the midbrain dopaminergic system (Gerfen and Surmeier, 2011), we have recently proposed that dopamine may modulate basal ganglia beta oscillations by acting on the striatum, in particular via the striatal cholinergic system. Dopamine, acting on D2 receptors, provides tonic suppression of acetylcholine (ACh) release in the striatum (DeBoer et al., 1996). Under conditions of low striatal dopaminergic tone, such as in PD, increased cholinergic tone may play a more prominent role in modulating striatal dynamics, such as supporting the generation of exaggerated beta oscillations (Ikarashi et al., 1997; Ding et al., 2006; McCarthy et al., 2011). Additionally, the striatum contains high levels of cholinergic markers (Pisani et al., 2007), highlighting a prominent role for cholinergic regulation in striatal function.

Recently, we demonstrated that direct local infusion of the cholinergic agonist carbachol into the striatum of normal mice can generate robust beta oscillations within

the striatum (McCarthy et al., 2011). Using computational approaches, our previous study predicted that increased striatal cholinergic tone could lead to elevated beta oscillations through activation of muscarinic receptors that lead to the suppression of M current in the striatal medium spiny neurons. Here, to further demonstrate the function of the intrinsic striatal cholinergic system in modulating neural dynamics of the CBT network and the related receptor mechanisms, we selectively activated striatal cholinergic interneurons (SChIs) by using optogenetic techniques, while simultaneously recording local field potentials (LFPs) in the striatum and the primary motor cortex (M1), with or without local infusion of selective cholinergic receptor antagonist. We found that brief optogenetic stimulation of SChIs acutely elevated beta oscillations in the striatum and all cortical layers of M1, and gamma oscillations in the striatum and deeper layers of M1. Increased oscillations were accompanied by increased coherence between striatum and M1 in a layer-dependent manner. In addition, local striatal infusion of the muscarinic receptor blocker scopolamine, but not the nicotinic receptor blocker mecamylamine, reduced striatal beta oscillations. Finally, we assessed the effect of SChI stimulation on locomotion and found that activation of SChIs decreased movement, increased immobility, and increased rotation. Together, these results demonstrate that activation of SChIs can generate elevated beta and gamma oscillations and coherence in the cortico-striatal network in a cortical layer-dependent manner via muscarinic receptors, and alter locomotion behavior.

2.3 Methods

2.3.1 Experimental Preparation

All animal procedures were approved by the Boston University Institutional Animal Care and Use Committee (IACUC). Surgically implanted adult mice were recorded awake, head-fixed. Recordings were made simultaneously in the striatum [stereotac-

tic coordinates 0 anterior-posterior (AP), 2.5–3 medial-lateral (ML), 2–2.5 depth] by using a glass pipette to avoid photoelectric effects during optogenetic laser illumination, and in the primary motor cortex (M1) by using laminar electrodes containing 16 electrode contacts spaced at $100\,\mu$m, positioned across the entire cortical depth (coordinates 1.5–2 AP, 1.25–1.5 ML). To optogenetically activate SChIs, a fiber was coupled to a 473-nm laser.

Greater detail of the animal procedures, behavioral analysis, and histology is available in the Supporting Information Methods Summary of the original paper (Kondabolu et al., 2016).

2.3.2   Electrophysiological Data Analysis

All data analysis were performed by using Matlab. LFPs were first bandpass filtered between 0.5 and 500 Hz with a second-order Butterworth filter to eliminate low frequency drifts, and then down-sampled to 250 Hz by using Matlab's resample function. The resulting LFPs were passed through a 60 Hz notch filter by using Matlab's *iirnotch* function. To reduce edge artifacts, 300 ms of data were removed from the beginning and end of every trial for all subsequent analysis.

In awake, head-fixed recordings, there were occasional motion artifacts that influenced spectral analysis. Trials with artifacts were rejected according to the following method. LFPs recorded in each trial were first bandpass filtered with a second-order Butterworth filter from 1 to 100 Hz. Trials where LFPs had a maximum amplitude greater than 7.5 SDs from the mean or a minimum amplitude greater than 5 SDs from the mean were rejected.

At the onset of optogenetic laser stimulation, LFPs exhibited large deflections, which were likely due to synchronized current influx into stimulated neurons and their downstream targets. At the offset of optogenetic laser stimulation, LFPs also exhibited large deflections, likely due to the current efflux from activated neurons.

Because these large LFP deflections interfere with spectral analysis, we excluded the 500 ms immediately after laser onset and offset from further analyses. To estimate the power spectrum and coherence for different M1 layers, recordings from different laminar electrode contacts were grouped according to anatomical locations based on the electrode intercontact distance and histological findings. We grouped the recordings into superficial layers (0–500 μm from the cortical surface, electrode contacts 2–6), middle layers (500–800 μm, contacts 7–10), and deep layers (900–1200 μm, contacts 11–13).

We used the multitaper Fourier method for all spectral analysis, because it reduces noise through spectral smearing by obtaining multiple independent estimates from the data. Spectrums and spectrograms were calculated by using the *mtspectrumc* and *mtspecgramc* functions of the Chronux toolbox, respectively (Bokil et al., 2010). There was a frequency smear of ± 2 Hz, corresponding to 17–19 tapers, depending on period length. For spectrograms, a sliding 1 sec window with 20% overlap and three tapers was chosen. The log normalized power during and after laser illumination was computed from the natural logarithm of the quotient from division by the prelaser baseline power. The power spectrum was calculated by averaging across each electrode group (M1 only) and then across trials for each animal. The population power spectrum was obtained by averaging across animals. For the 1 sec stimulation protocols used in Figure S2, because of the 500 ms data removal immediately after laser onset and offset, we did not have enough time points left for power spectrum analysis during laser stimulation. Hence, we only examined the 1 sec period starting 500 ms after laser offset.

For statistical testing, alpha was 0.05 and not corrected. For nondrug data, a Wilcoxon signed-rank test was performed against the null hypothesis of no laser-induced power change for each frequency band. Bar plot 95% confidence intervals

were estimated with a bootstrap method by using 1000 resamples with replacement. For the drug infusion bar plots, nonoverlap of the confidence intervals indicated a significant difference in laserinduced power changes preinfusion to postinfusion. For the scopolamine drug infusion bar plots, preinfusion and postinfusion were tested separately by using a bootstrap resampling test against 0 laser-induced power change because scopolamine reduced the prelaser baseline power. For mecamylamine and ACSF, baseline power was not affect by infusion, so preinfusion to postinfusion laser-induced power changes were compared with a paired signed-rank test.

The coherence and coherograms were computed by averaging trials from all animals with Chronux's *coherency* and *cohgramc* functions, respectively. The same frequency smear, window, and resulting tapers from the power analysis were used. For coherence, after a Fisher z-transformation, the prelaser baseline was subtracted from the coherence estimates for the other periods. Population estimates were calculated by averaging across M1 channel groups. The jackknifed 95% confidence intervals were used to test for significance of laser-induced coherence changes at the 0.05 alpha level.

2.4   Results

2.4.1   Selective Optogenetic Activation of SChIs Increased Striatal Alpha, Beta, and Gamma Oscillations

We recently demonstrated that the striatal cholinergic system can support the generation of beta oscillations by using a combination of mathematical modeling and experimental techniques that combined in vivo electrophysiology with local infusion of the nonselective cholinergic agonist carbachol (McCarthy et al., 2011). To further explore the ability of intrinsic SChIs in modulating beta oscillations throughout the CBT network, we recorded LFPs in the striatum and the primary motor cortex

(M1), while optogenetically activating SChIs in transgenic choline acetyltransferase promoter (Chat)-Channelrhodopsin-2 (ChR2) mice (Figure 2·1A). Chat-ChR2 mice were generated by crossing Chat-Cre mice with Cre-regulated ChR2-reporter mice (Ai32), resulting in selective ChR2 expression in Chat-positive SChIs (Figure 2·1B). Control groups consisted of Ai32 transgenic littermates that did not express ChR2 protein because of the lack of Cre recombinase expression, despite the presence of ChR2 genes in the genome. An optical fiber coupled to a glass electrode was positioned in the dorsal striatum for simultaneous optogenetic stimulation and LFP recordings. Glass electrodes were used to record LFPs at the site of laser illumination to avoid photoelectric effects that are routinely observed on electrodes made of other materials (Figure 2·1A) (Han et al., 2009).
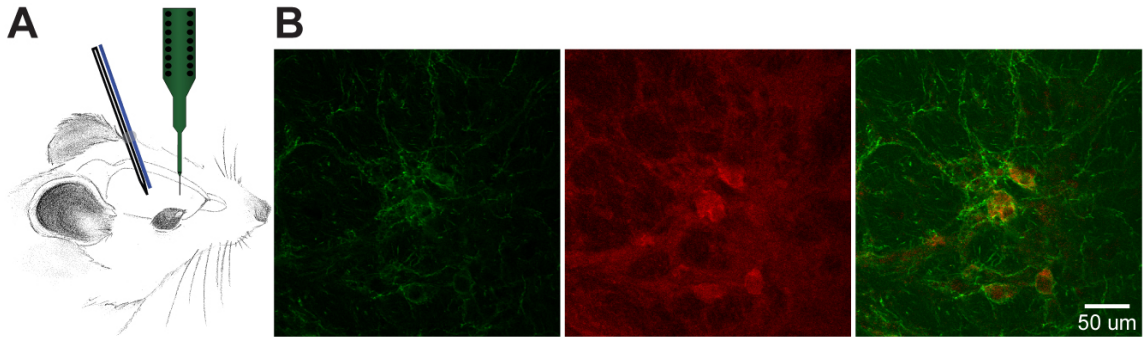
Figure 2·1: Experimental setup and protocols. (A) Illustration of the recording configuration. The recording pipette was coupled to an optical fiber and a laminar probe containing 16 electrode contacts, positioned in the M1. (B) A representative image of the striatum showing ChR2-eYFP fluorescence (green; Left), immunofluorescence of ChAT (red; Middle), and co-localization (Right).

Optogenetic activation of SChIs with a Poisson-distributed 40 Hz laser light pulse train robustly increased oscillations across broad frequencies in the striatum (Figure 2·2C and D). The increase in oscillation power persisted for several hundred milliseconds after laser offset (Figure 2·2C and D), suggesting that direct patterning of SChIs by laser pulses was unlikely to account for the elevated oscillations at these frequencies. To further evaluate the changes at specific frequency bands, we calculated the normalized spectrum before, during, and after laser stimulation. We found that

optogenetic stimulation of SChIs robustly increased oscillation power across higher frequency bands conventionally defined as alpha (8–15 Hz), beta (15–30 Hz), low gamma (30–60 Hz), and high gamma (60–100 Hz), but not lower frequency bands of delta (1–4 Hz)or theta(4–8 Hz)(Figure 2·2E and F; n = 7 mice). A similar laser illumination protocol in Ai32 control mice failed to alter oscillation power at any frequency (n = 5 mice, P > 0.05 for all bands, signed-rank test), confirming that the observed changes in Chat-ChR2 mice are due to optogenetic activation of SChIs.

To further rule out the possibility that the observed oscillation changes were due to direct activation of SChIs, we tested a set of seven additional laser illumination parameters, including 5-s-long constant laser illumination, 1-s-long fixed interval pulse trains at 50 and 100 Hz, as well as Poisson-distributed pulse trains at 4, 9, 20, and 40 Hz. Because of the large LFP deflections induced by optogenetic stimulation of SChIs during the 1-s stimulation, it was difficult to reliably estimate the power changes during laser stimulation. Thus, we analyzed the 1-s period immediately following laser offset. In general, we observed similar increases in beta and gamma oscillations by using these stimulation patterns (Figures 2·3B and 2·42; n = 5 mice, P ≤ 0.05, signed-rank test). Together, these results demonstrate that direct activation of SChIs generates robust beta and gamma oscillations within the striatum that are independent of the particular optogenetic stimulation pattern and persist for an extended period after the offset of light illumination, suggesting that these oscillations emerge from dynamic network interactions upon an increase in the striatal cholinergic tone.

2.4.2 SChI Activation Leads to Layer-Dependent Beta and Gamma Oscillation Changes in the M1

To understand the influence of the oscillations induced by optogenetic stimulation of SChIs on the rest of the CBT network, we performed simultaneous recordings in M1 by
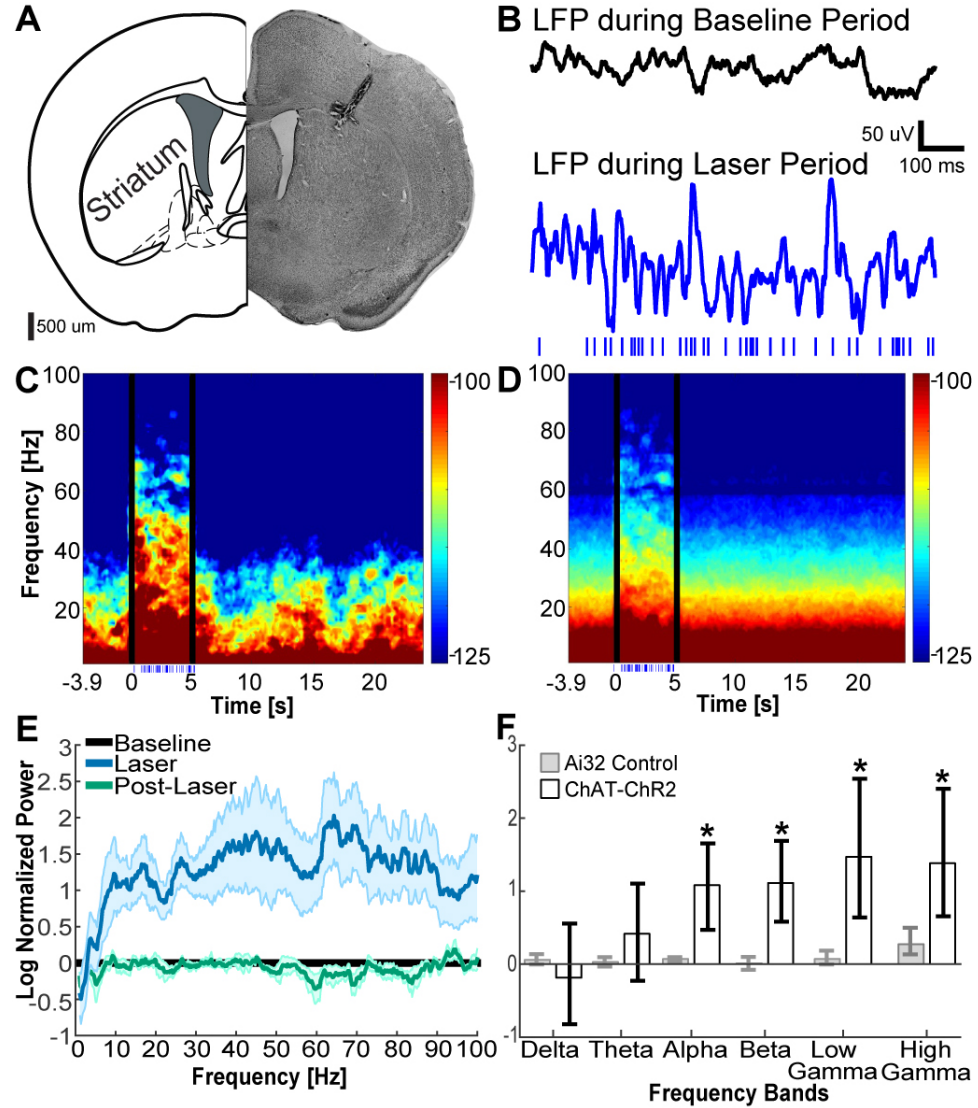
Figure 2·2: Poisson-distributed 40 Hz optogenetic activation of SChIs increased striatal alpha, beta, and gamma oscillations. (A) Representative coronal histological section showing an electrode and optical fiber track into the striatum. (B) Representative 1-s LFPs recorded in the striatum before (Top) and during (Bottom) laser stimulation at Poisson-distributed 40 Hz (Bottom; blue dashes indicate the time of laser pulses). (C) Representative spectrogram from one mouse, aligned to laser onset and averaged over all trials. The 500 ms immediately after laser onset and offset were excluded from the corresponding statistics because of strong LFP deflections. (D) Population spectrogram upon optogenetic stimulation of SChIs in ChAT-ChR2 mice (n = 7 mice). (E) Population power spectrum normalized to baseline, across frequencies before (Baseline, black), during (blue), and after laser stimulation (green), in the Chat-ChR2 mice (n = 7 mice). The shaded area around each solid line represents the SEM. (F) Bar plots comparing changes upon laser stimulation in different frequency bands between the Chat-ChR2 experimental group and the Ai32 control group for delta (1–4 Hz), theta (4–8 Hz), alpha (8–15 Hz), beta (15–30 Hz), low gamma (30–60 Hz), and high gamma (60–100 Hz) oscillations. The error bars represent the bootstrapped 95% confidence intervals (*P $\leq$ 0.05, nonparametric signed-rank test).
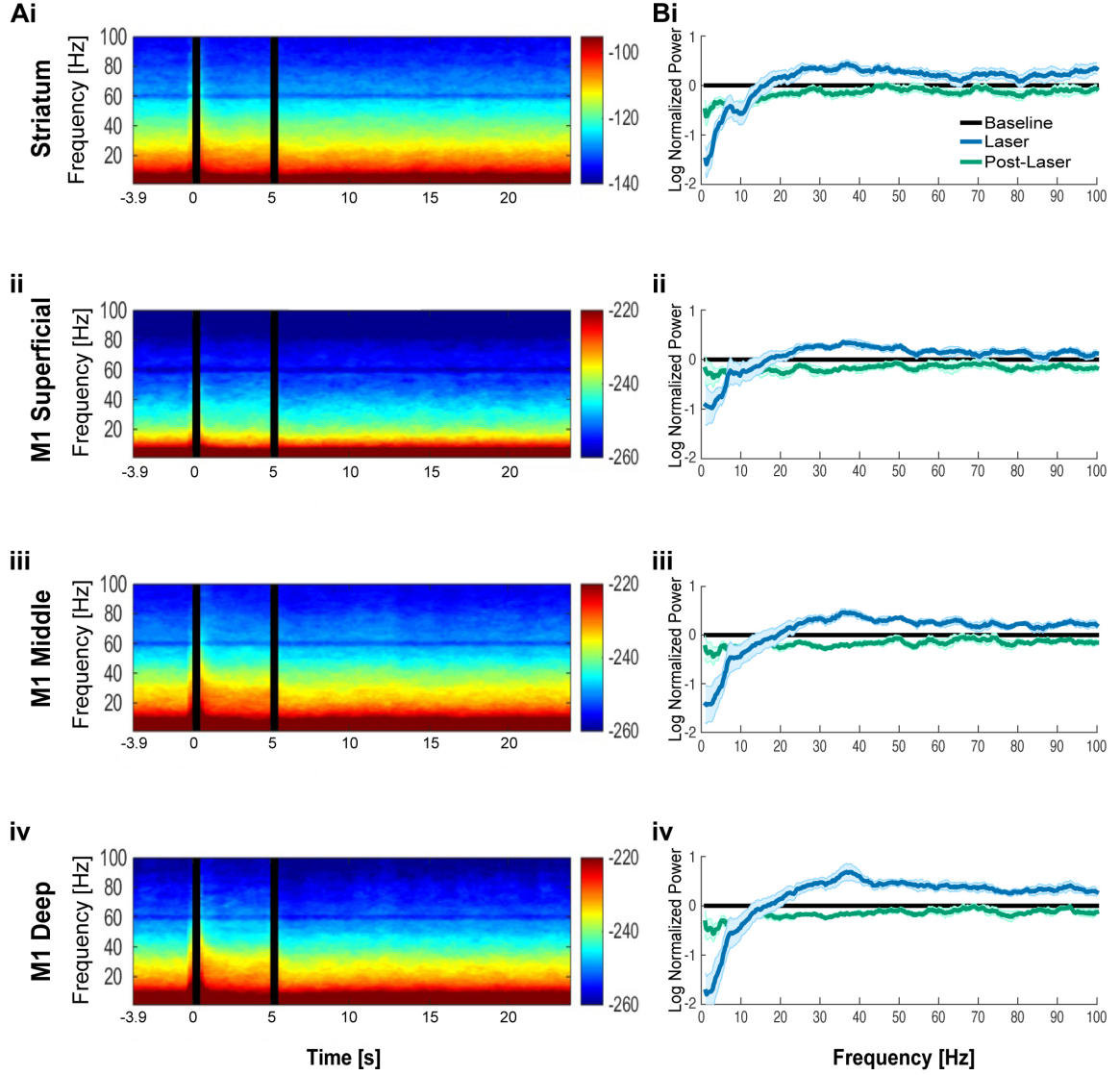
Figure 2·3: Oscillations induced by SChI optogenetic stimulation with a constant, 5-s-long laser illumination pattern. (A) Spectrograms before, during, and after optogenetic stimulation in striatum (i), as well as superficial (ii), middle (iii), and deep (iv) M1 layers. Laser was on at 0–5 s. (B) Normalized spectral power to prelaser baseline period in striatum (i), as well as the superficial (ii), middle (iii), and deep (iv) layers of M1. Constant light illumination patterns elicited increases in beta and gamma oscillations in striatum, as well as all layers of motor cortex. The shaded region represents the SEM.
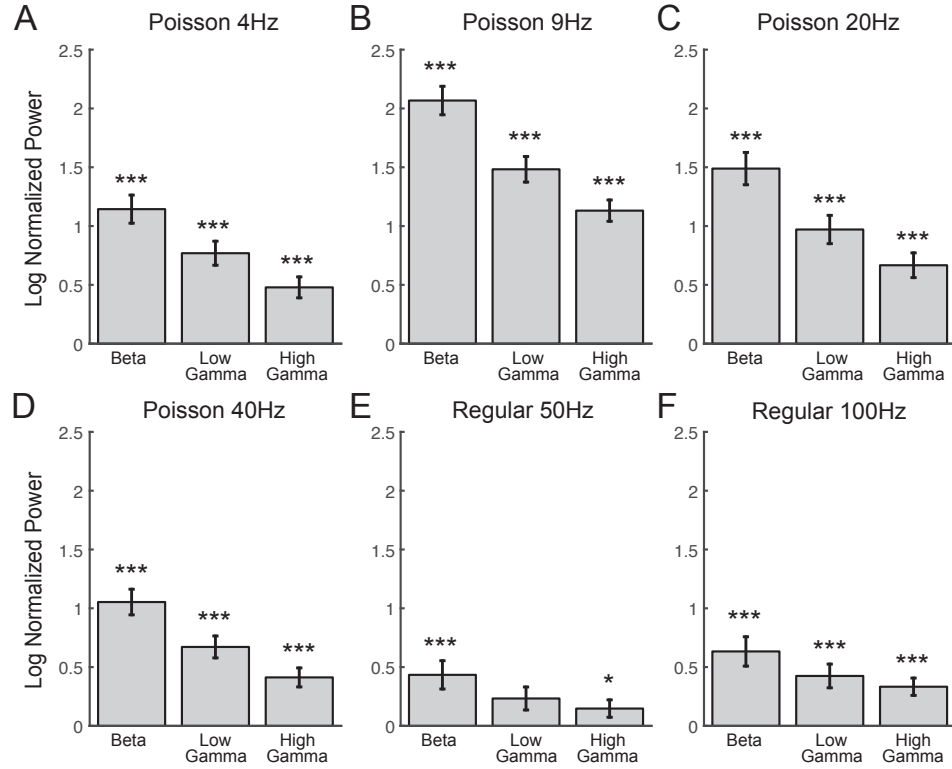
Figure 2·4: Optogenetic stimulation of SChIs increased striatal beta and gamma oscillatory power by using 1-sec-long laser illumination patterns, pulsed at Poisson-distributed 4 Hz (A), Poisson-distributed 9 Hz (B), Poisson-distributed 20 Hz (C), Poisson-distributed 40 Hz (D), regular 50 Hz (E), and regular 100 Hz (F). These stimulation protocols elicited increases in beta (15–30 Hz), low-gamma (30–60 Hz), and high-gamma (60–100 Hz) oscillations in striatum. The bars are the natural logarithm of the quotient of the power during the 1-s period starting 500 ms after laser offset divided by the prelaser baseline power. The error bars represent the SEM. (*P < 0.05, ***P < 0.001, nonparametric signed-rank test).

using a laminar electrode containing 16 contacts spaced at 100 µm, which can identify cortical layer-dependent changes (Figure 2·5A and B). We did not observe laser-induced photoelectric artifacts on the laminar electrodes in M1. Because they were 2 mm away from the striatal laser illumination site, <0.1% of laser light was expected to reach M1 (Han et al., 2009). Optogenetic activation of SChIs in the striatum coincided with robust LFP voltage deflections across all cortical depths in M1 (Figure 2·5B), and oscillation power consistently increased with cortical depth (Figure 2·5C). To compare the difference in LFPs across anatomically defined cortical layers, we averaged the power spectra recorded at different depths, with the first 500 µm corresponding to the superficial layers, 500–800 µm corresponding to the middle layers, and 900–1200 µm corresponding to the deep layers.

Beta frequency power consistently increased in all M1 layers during SChI stimulation. In contrast, gamma frequency power, both high gamma and low gamma, were selectively increased in the deep layers, but not the superficial layers (Figure 2·5 D-F). In the middle layers, high gamma power was elevated, but not low gamma power. We observed small but nonsignificant changes in delta, theta, and alpha frequencies across all layers. Together, these results provide direct evidence that SChI activation can enhance beta oscillations in all M1 layers, and gamma oscillations in a cortical layer-dependent manner. These SChI activation-induced beta and gamma oscillations across different M1 layers suggest that beta oscillations can be widely expressed by neuronal ensembles within different M1 cortical layers, whereas gamma oscillations are selectively expressed in deeper layers, although it is unknown how different cell types within each M1 layer uniquely support these oscillations.
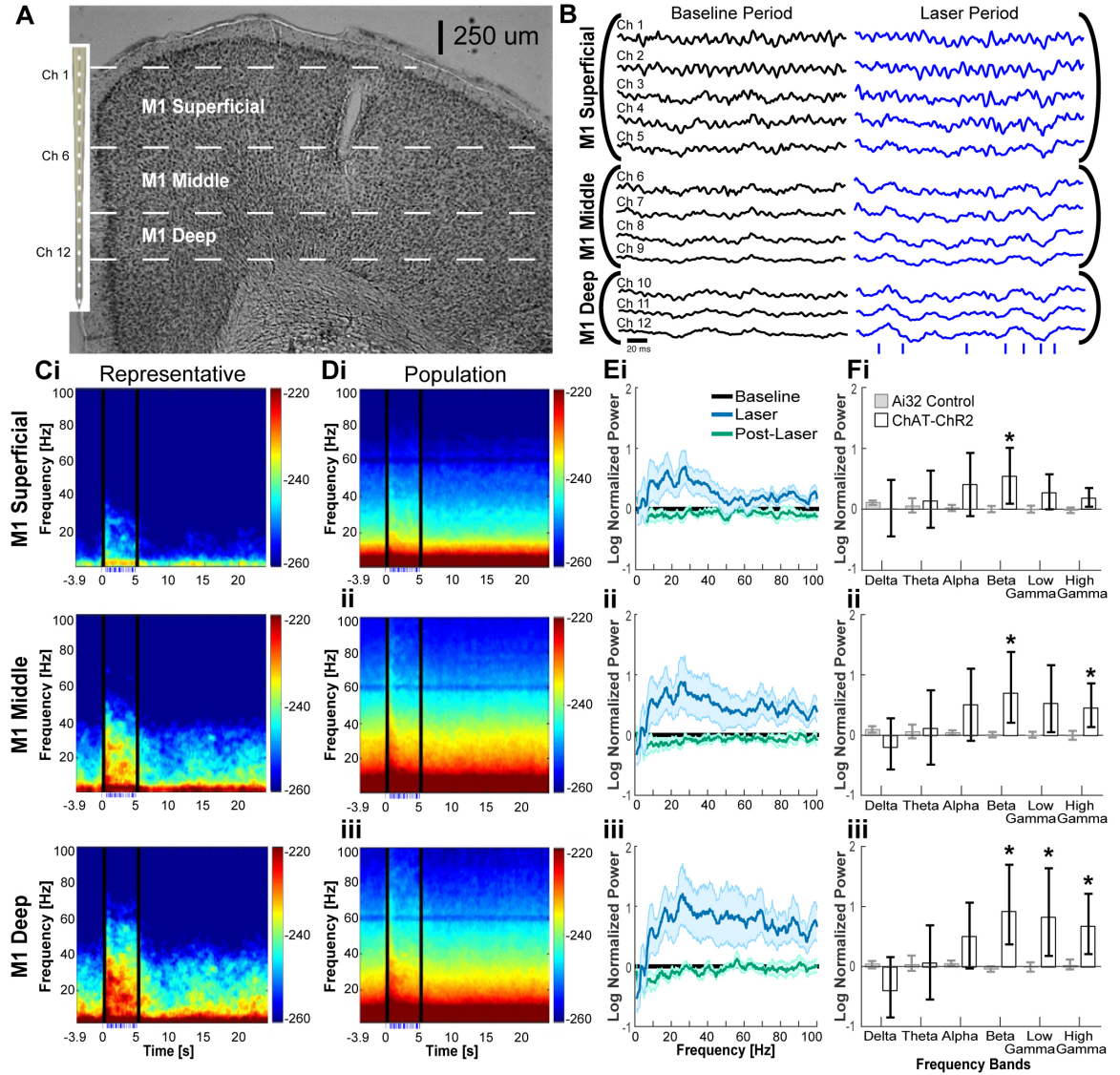
Figure 2·5: SChI activation led to layer-dependent beta and gamma oscillation changes in the M1. (A) Representative coronal section demonstrating the position of laminar electrodes in M1. (B) Representative 200-ms LFPs during the baseline period before laser simulation (black) and during laser stimulation period (blue). (C) Representative power spectrum from an individual mouse for superficial layers (C, i, averaged across Ch1–Ch5), middle layers (C, ii, averaged across Ch6–Ch9), and deep layers (C, iii, averaged across Ch10–Ch12). The 500 ms immediately after laser onset and offset were excluded from the corresponding statistics because of strong LFP deflections. (D) Population spectrograms aligned to laser onset for superficial layers (D, i), middle layers (D, ii), and deep layers (D, iii) (n = 7 mice). Bottom, blue dashes indicate the timing of laser light pulsed at Poisson-distributed 40 Hz, for 5 s. (E) Population spectrum for M1 superficial layers (E, i), middle layers (E, ii), and deep layers (E, iii). (F) Bar plots comparing oscillation powers at different frequencies in superficial (F, i), middle (F, ii), and deep (F, iii) layers for delta (1–4 Hz), theta (4–8 Hz), alpha (8–15 Hz), beta (15–30 Hz), low gamma (30–60 Hz), and high gamma (60–100 Hz). Error bars represent the bootstrapped 95% confidence intervals (*P ≤ 0.05, nonparametric signed-rank test).

### 2.4.3   SChI Activation Modulates Coherence Between the Striatum and M1

To evaluate the synchronization of oscillations between the striatum and M1 upon optogenetic activation of SChIs, we calculated the coherence of the LFPs recorded in these two structures before and during laser stimulation. We found an increase in coherence during laser stimulation between deep layers of M1 and the striatum at both beta and low gamma frequencies, but not at high gamma frequencies (Figure 2·6; $P \leq 0.05$, jackknife test). This increased coherence is consistent with the idea that deep M1 layers contribute to M1-striatal coordination through direct axonal projections. However, we note that although the coherence at beta frequencies below 23 Hz is maintained throughout the simulation, coherence at higher beta frequencies dissipates rapidly after the first second of stimulation, suggestive of multiple independent beta oscillations within the 15–30 Hz range defined here.

The lack of coherence changes at high gamma frequencies suggests that the observed increase in high gamma power may be due to increased local neuronal activity within M1 (Manning et al., 2009). In the middle layer, where both beta and high gamma power increased, we observed a significant increase in coherence at beta frequency, but not at high gamma frequencies (Figure 2·6). Considering that middle layers of M1 do not directly connect to the striatum, the observed increase in coherence at beta frequencies are likely coordinated or relayed through other structures, such as the thalamus that directly project to the middle layer, especially layer 4. Surprisingly, despite the increase in superficial layer beta power, activation of SChIs resulted in significant attenuation of coherence at beta and gamma frequencies (Figure 2·6; $P \leq 0.05$, jackknife test), suggesting that oscillations within the striatum and superficial M1 are independently regulated. In summary, activation of SChIs in the striatum appears to engage multiple independent beta generators that interact in the
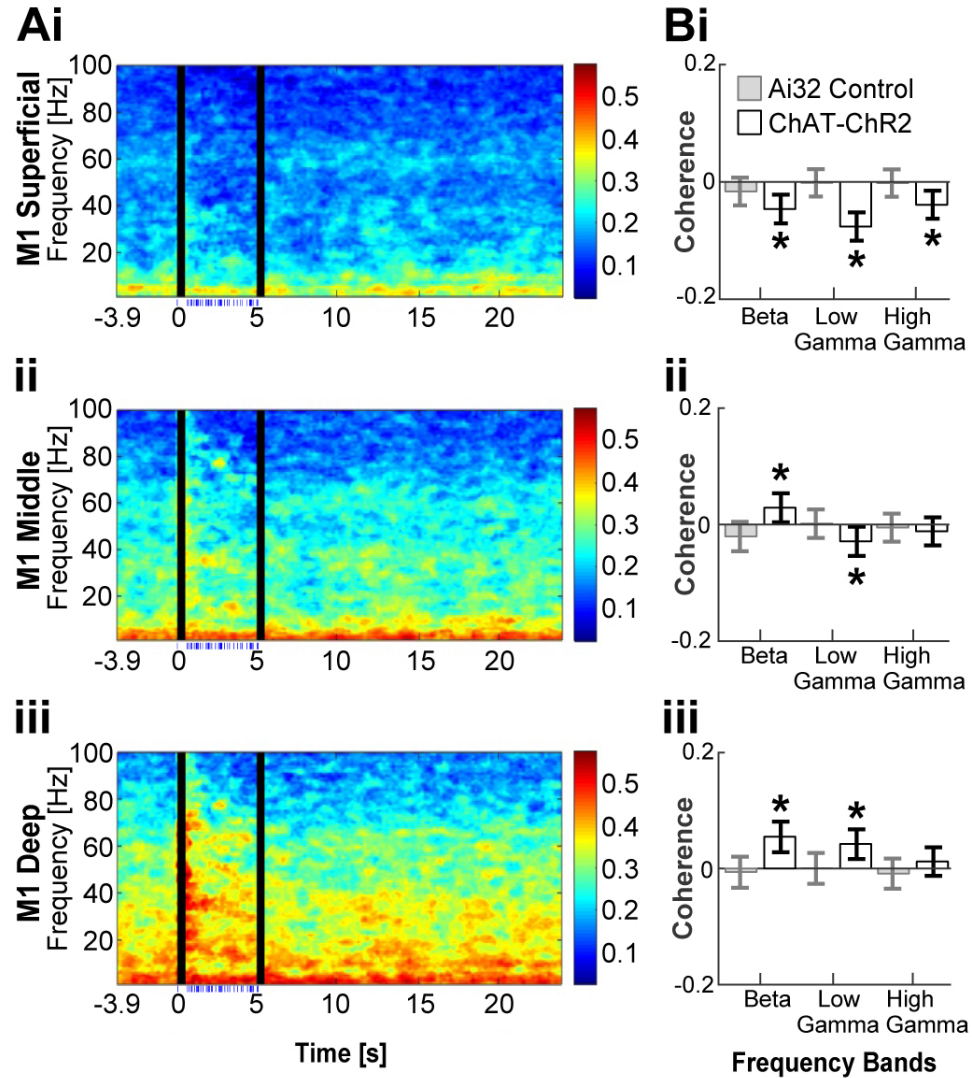
Figure 2·6: SChI activation modulated coherence between the striatum and M1. (A) Population coherograms show coherence between the striatum and superficial (i), middle (ii), and deep layers (iii) of M1 before, during, and after laser stimulation. Laser stimulation was pulsed at a Poisson-distributed 40 Hz, during 0–5 s (bottom, blue dashes indicate the timing of laser pulses, n = 7 mice). The 500 ms immediately after laser onset and offset were excluded from the corresponding statistics because of strong LFP deflections. (B) Bar plots comparing the coherence between the striatum and M1 superficial (B, i), middle (B, ii), and deep (B, iii) layers before and during laser stimulation for beta (15–30 Hz), low gamma (30–60 Hz), and high gamma (60–100 Hz) frequencies. Error bars indicate the jackknifed 95% confidence interval error bars (*P ≤ 0.05, nonparametric jackknife test).

CBT network in a cortical layer-dependent manner, whereas high gamma oscillations are locally generated.

2.4.4 Striatal Muscarinic Receptors Mediate SChI-Induced Beta and Low Gamma Oscillations in the Corticostriatal Network

To understand the receptor mechanism by which SChIs engage the striatum and M1 to generate beta and gamma oscillations, we combined optogenetic activation of SChIs with local intracranial infusion of selective cholinergic receptor antagonists. We infused either the muscarinic antagonist scopolamine (100 µm/µL) or the nicotinic antagonist mecamylamine (10 µm/µL) into the striatum, and optogenetically activated SChIs while simultaneously recording LFPs in the striatum and M1.

We observed that scopolamine infusion in the striatum broadly decreased oscillation power in the striatum across all frequencies analyzed (approximately from 2 to 100 Hz, Figure 2·7A; n = 8 mice; >2 SEM). A similar reduction in oscillation power was also observed in the middle and deep layers of M1, although not at very low frequencies of 2-5 Hz, (Figure 2·7B; n = 8 mice). Interestingly, no change in power was observed in the superficial layers of M1, suggesting that oscillatory dynamics in the superficial layers are only loosely coupled to the CBT network (Figure 2·7 B, i). Together these results demonstrate that intrinsic striatal muscarinic tone is responsible for basal levels of oscillations across broad frequencies in the striatum and deeper layers of M1.

We next tested the effectiveness of optogenetic activation of SChIs in generating oscillations in the presence of muscarinic or nicotinic receptor blockers. Because of the reduction of oscillation power across all frequencies upon scopolamine infusion, we cannot directly compare the effects of optogenetic stimulation in the presence of scopolamine to that observed in the absence of scopolamine. We thus compared the effect of optogenetic activation of SChIs in the presence of scopolamine and found
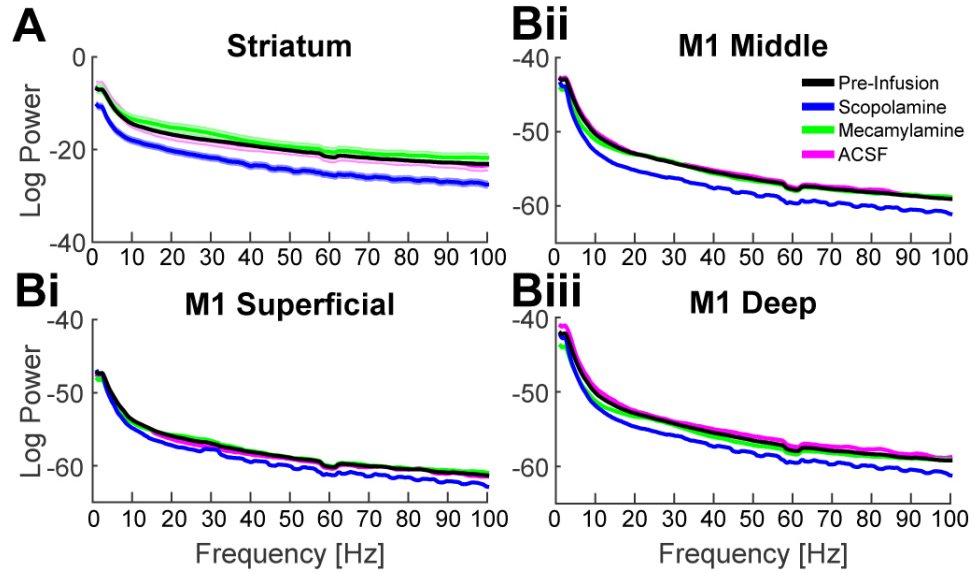
Figure 2·7: Striatal muscarinic receptors modulated basal levels of beta and gamma oscillations in the striatum and deeper layers of M1. After striatal drug infusion, population power spectrums in the striatum (A), and different layers of M1 [superficial (B, i), middle (B, ii), and deep layers (B, iii)]. The shaded area around each solid line represents the SEM. Scopolamine infusion reduced oscillation power in the striatum, middle layers of M1, and deep layers of M1.

that activation of SChIs in the presence of the muscarinic blocker scopolamine remained effective at inducing beta, low gamma, and high gamma oscillations in the striatum (Figure 2·8 B, i and C, i; $P \leq 0.05$, bootstrap test). However, the increases were relatively weaker compared with that observed without scopolamine (Figure 2·8 A, i). In M1, SChI stimulation in the presence of scopolamine failed to alter beta, low gamma, or high gamma power from the prestimulation baseline in any cortical layer (Figure 2·8 B, ii-iv and C, ii-iv; $P > 0.05$, signed-rank test). Infusion of artificial cerebrospinal fluid (ACSF) or the nicotinic antagonist mecamylamine failed to alter oscillation power at any frequency in the striatum or M1, compared with the preinfusion baseline (Figures 2·7 and 2·9, n = 6 mice infused with mecamylamine; and Figure S4, n = 5 mice infused with ACSF; $P > 0.05$, signed-rank test). Together, these results suggest that cholinergically induced elevation of beta and gamma oscillations in the striatum is mediated by striatal muscarinic receptors, but not by striatal

nicotinic receptors. The fact that in the presence of scopolamine, SChI activation only elevated striatal oscillations, but not M1 oscillations, suggests that striatal beta oscillations are independent of phasic beta input from M1, supporting the existence of a basal ganglia generator of beta oscillations. These results further suggest that the elevation in M1 beta oscillations depends on active muscarinic mechanisms in the striatum.

2.4.5 Unilateral SChI Activation Decreases Locomotion and Increases Rotation Behavior

To evaluate whether a transient increase in striatal cholinergic tone is sufficient to alter locomotion, we optogenetically stimulated SChIs in another group of freely moving mice. To optimize the illumination volume, we designed a fiber array containing four optical fibers unilaterally targeting a large fraction of the dorsolateral striatum that receives M1 inputs (Ramanathan et al., 2002) in Chat-ChR2 mice (n = 5 mice), or control Ai32 mice (n = 5 mice). We monitored the locomotion in a custom arena while optogenetically stimulating SChIs by using the same light illumination pattern at Poisson-distributed 40 Hz, but illuminated for 2 min to better quantify behavioral effects (Figure 2·11A). Locomotion was monitored for 8 min/d, over 7 consecutive days.

We first estimated the overall effect of stimulating SChIs on locomotion by calculating the total distance traveled during each 2-min period before, during, and after laser illumination and found that optogenetic activation of SChIs significantly reduced the total distance traveled compared with the pre-laser baseline period (Figure 2·11B and C; $P \leq 0.001$, Bonferroni-corrected nonparametric paired signed-rank tests). This reduction persisted for an additional 2 min immediately after laser offset (post-laser 1) ($P \leq 0.001$, paired signed-rank test) and returned to baseline in the subsequent 2-min interval (Post-Laser 2) ($P > 0.05$, paired signed-rank test). Further analysis
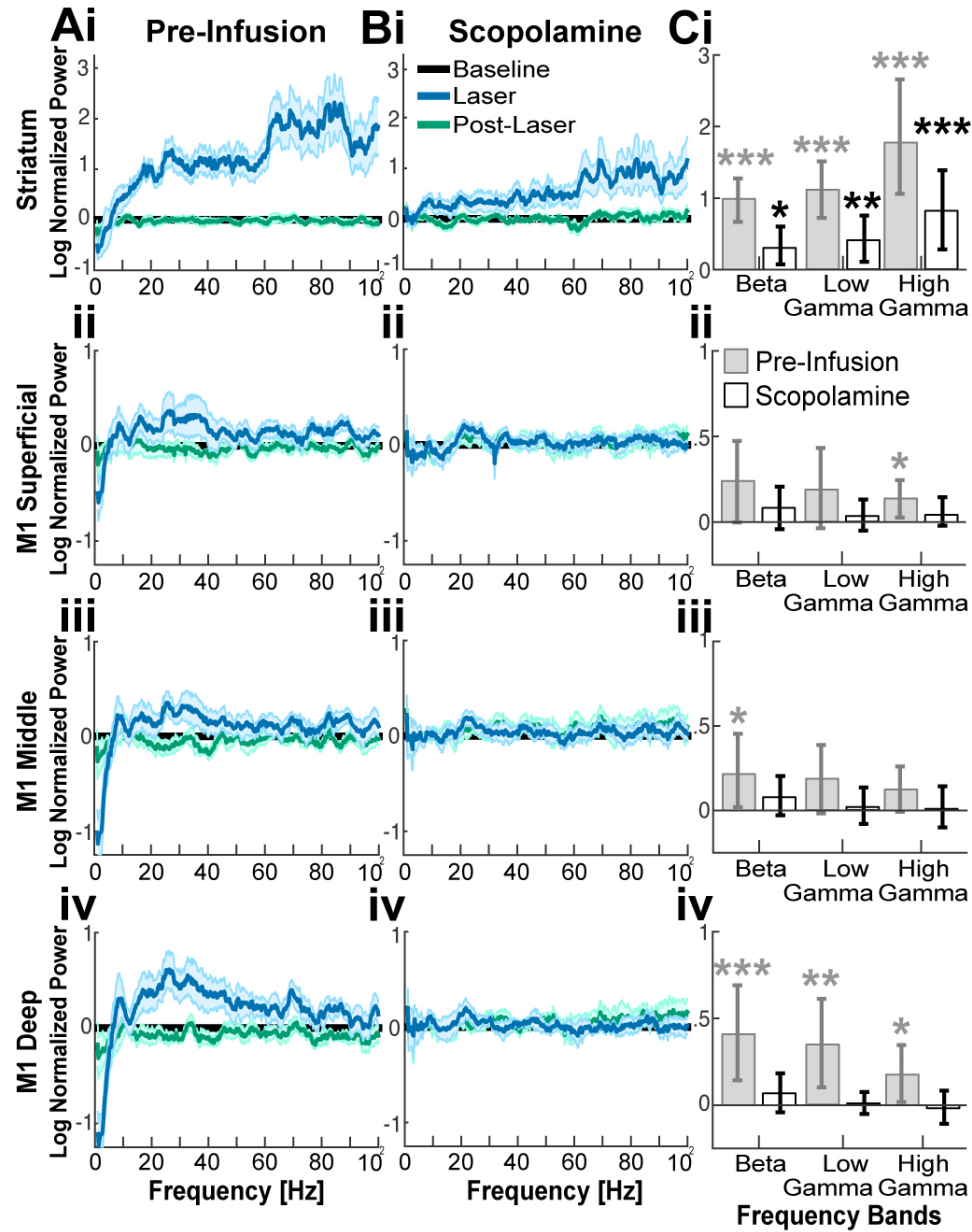
Figure 2·8: Striatal muscarinic receptors mediated SChI-induced beta and gamma oscillations in the striatum and M1. (A and B) Optogenetic stimulation induced changes in the power spectrum before (A) and after (B) scopolamine infusion (n = 8 mice), in the striatum (i), superficial (ii), middle (iii), and deep layers of M1 (iv). The power spectrum during laser stimulation (blue) and after laser stimulation (green) was normalized to the baseline (black). (C) Bar plot comparison of oscillation power changes in beta (15–30 Hz), low gamma (30–60 Hz), and high gamma (60–100 Hz) frequencies, before (gray) and after (white) scopolamine infusion. Error bars are the bootstrapped 95% confidence intervals (*P ≤ 0.05; **P ≤ 0.01; ***P ≤ 0.001; nonparametric bootstrap test).
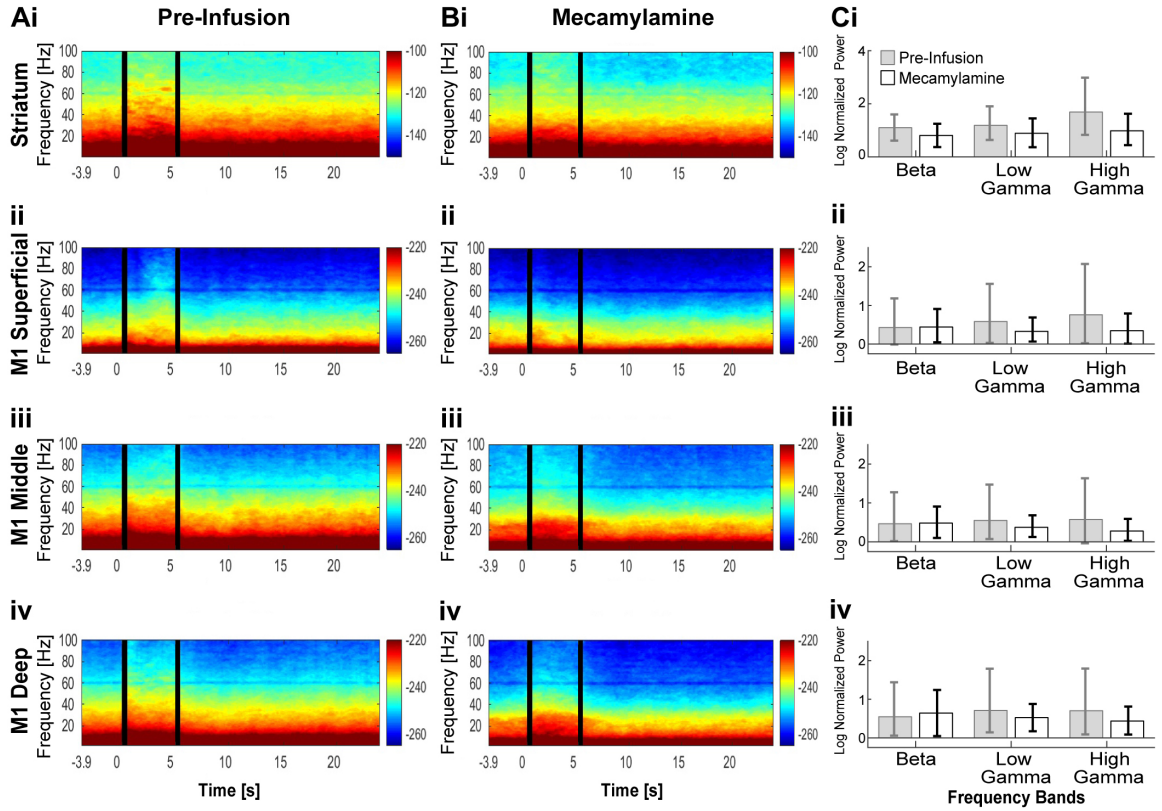
Figure 2·9: Oscillations induced by optogenetic stimulation of SChIs, in the presence of the nicotinic receptor antagonist mecamylamine in the striatum (i) as well as superficial (ii), middle (iii), and deep (iv) M1 layers. (A) Preinfusion spectrogram demonstrating increased beta and gamma oscillations in the striatum, as well as elevated beta oscillations in all layers of M1 and gamma oscillations in deeper layers of M1. (B) Postinfusion spectrograms showing increased beta and gamma oscillations in striatum and M1. (C) Bar plot comparing SChI stimulation-induced oscillation changes between preinfusion and postinfusion periods. There were no significant changes in beta and gamma power when comparing premecamylamine with postmecamylamine infusion laser-induced power in the striatum. The error bars represent the 95% confidence intervals (*P < 0.05; ***P < 0.001; non-parametric paired signed-rank test). Beta, 15–30 Hz; low gamma, 30–60 Hz; high gamma, 60–100 Hz.
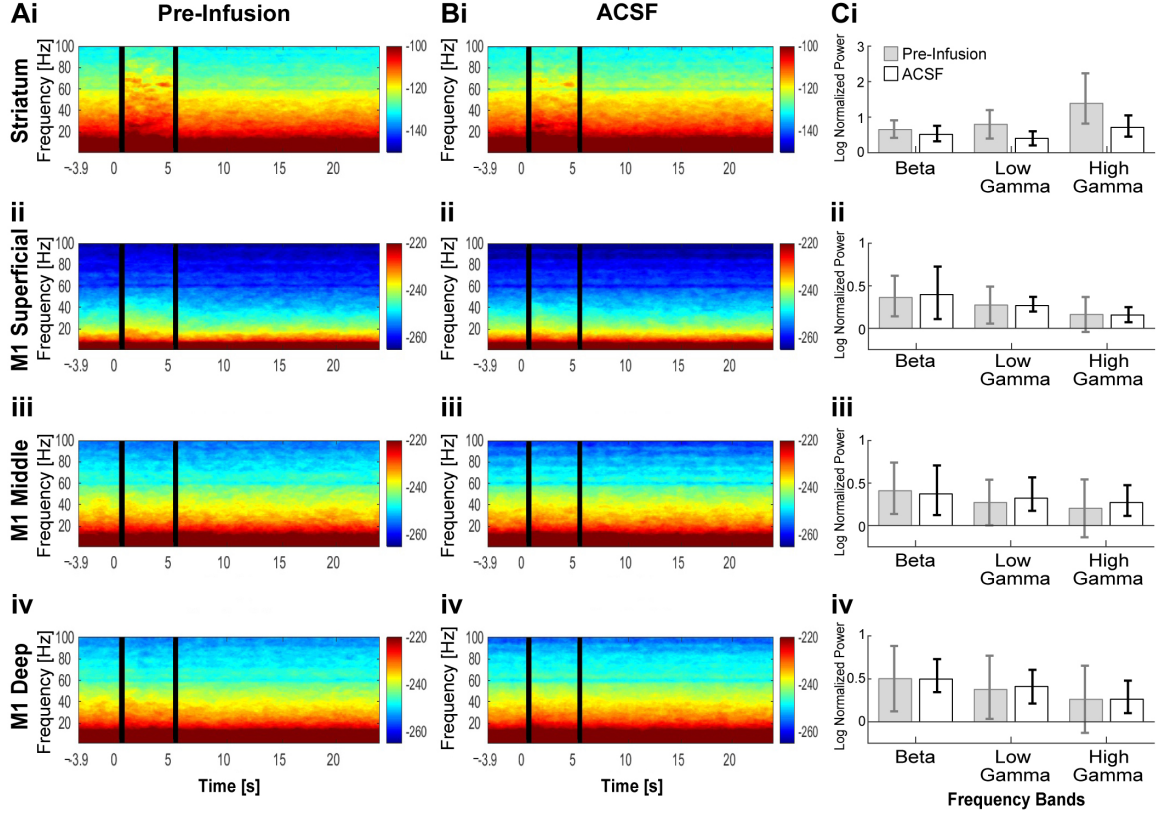
Figure 2·10: Oscillations induced by optogenetic stimulation of SChIs upon infusion with ACSF in the striatum (i) as well as the superficial (ii), middle (iii), and deep (iv) M1 layers. (A) Preinfusion spectrogram. (B) Postinfusion spectrogram. (C) Bar plot comparing laser-induced oscillation power normalized to the prelaser baseline during preinfusion and postinfusion period. Laser stimulation was effective at inducing beta and gamma oscillations. There were no significant differences between preinfusion and postinfusion in striatum. The error bars represent the 95% confidence intervals. (*P < 0.05; ***P < 0.001; nonparametric paired signed-rank test). Beta, 15–30 Hz; low gamma, 30–60 Hz; high gamma, 60–100 Hz.
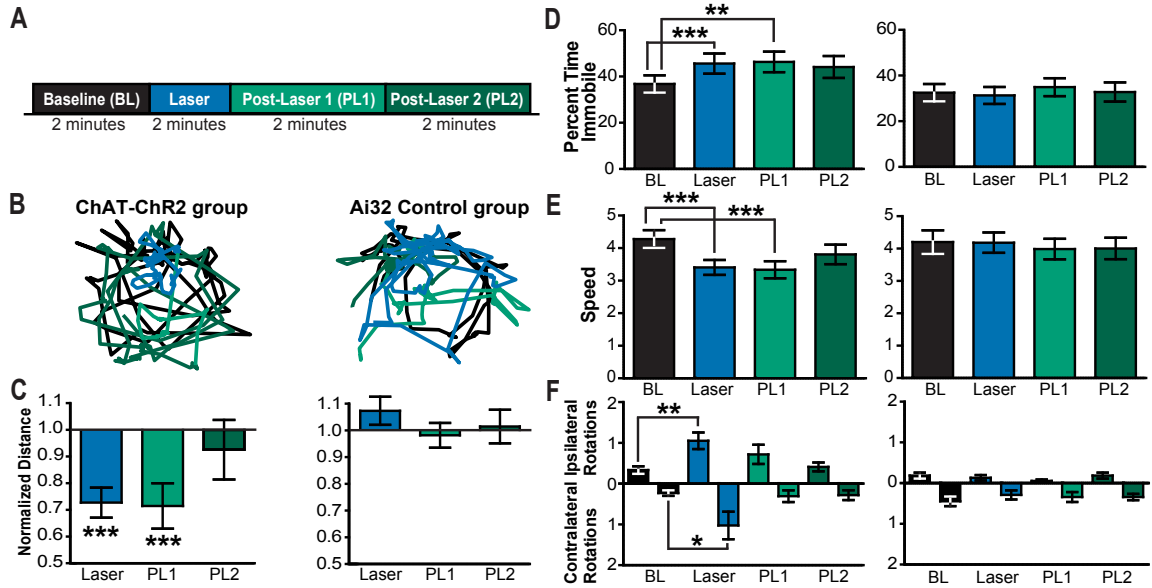
Figure 2·11: Unilateral SChI activation decreased locomotion and increased rotation behavior. (A) Behavioral optogenetic experimental protocol consists of a baseline period, laser period, and two post-laser periods (2 min per period). (B) Representative positions of a ChAT-ChR2 mouse (Left) and a control Ai32 mouse (Right) before (black trace), during (blue trace), and post-laser periods (green traces) after laser illumination. (C–E) Bar plot comparison of locomotor activity measures, including baseline-normalized distance (C), percent time immobile (D), and movement speed when mobile (E). (F) Bar plot comparison of rotation in the Chat-ChR2 group (Left) and the control Ai32 group (Right) (n = 5 mice for Chat-ChR2 group; n = 5 mice for control Ai32 group). Error bars indicate the SEM (*P ≤ 0.05; **P ≤ 0.01; ***P ≤ 0.001; Bonferroni-corrected nonparametric paired signed-rank tests).

indicated that locomotion reduction resulted from in- creased immobility, defined as the percentage of time when movement was smaller than 1.5 cm/s (Figure 2·11D; $P \leq$ 0.001, paired signed-rank test), as well as decreased movement speed (Figure 2·11E; $P \leq 0.001$, paired signed-rank test). The same optogenetic analysis in control Ai32 mice did not produce any change in locomotion, immobility, or movement speed (n = 5, $P > 0.05$ for all periods analyzed, paired signed-rank test), confirming that the observed locomotion deficit was due to optogenetic activation of SChIs.

To further assess whether unilateral optogenetic stimulation of SChIs biases movement direction preference, we assessed rotation behavior. Interestingly, we found that stimulation of SChIs in one hemisphere resulted in a significant increase in both ipsilateral and contralateral rotations during the laser period (Figure 2·11F; $P \leq 0.01$ and $P \leq 0.05$, respectively, paired signed-rank test). Similar analysis in control Ai32 mice did not yield any change in rotation behavior ($P > 0.05$, paired signed-rank tests). In the context of our experimental protocol, these results suggest that optogenetic activation of SChIs is not sufficient to bias movement direction preference in freely moving mice, but instead leads to an overall increase in rotation behavior. In summary, our results suggest that SChIs are critically involved in modulating locomotion, and that a selective increase in striatal cholinergic tone leads to direct motor behavioral deficits.

2.5 Discussion

We tested the role of intrinsic physiological striatal ACh release in modulating beta and gamma oscillations within cortico-striatal circuits. Combining optogenetics, pharmacology, and electrophysiology in mice, we show that SChI activation reliably and reversibly increased alpha, beta, and gamma oscillations in the striatum. In M1, SChI stimulation increased beta power in all layers and gamma power in a layer-

dependent manner. SChI-induced striatal and M1 beta and low gamma oscillations critically depended on striatal muscarinic receptors. Furthermore, SChI activation correlated with decreased locomotion and increased rotation behavior. Together, these results demonstrate that SChIs mediate changes in beta and gamma oscillations within the CBT circuit that are relevant to movement and movement deficits.

Activation of SChIs selectively increased higher frequency oscillations in the striatum, including alpha, beta, and gamma oscillations, but not lower frequency theta or delta oscillations. In our previous work, we found beta oscillations were elevated in striatum in response to the local infusion of the cholinergic agonist, carbachol (McCarthy et al., 2011). However, this study did not look at gamma oscillations and, thus, more work is needed to determine whether carbachol also elevates gamma frequency rhythms in striatum. In M1, SChI activation increased beta oscillations in all layers, and gamma oscillations only in middle and deep layers. Interestingly, despite the increase in beta, low gamma, and high gamma oscillations in the striatum and M1 deeper layers, the coherence between these two structures remained unchanged at high gamma frequencies during SChI activation, further confirming that these oscillations are supported by distinct mechanisms, with high gamma oscilations likely representing a local increase in neuronal excitability (Manning et al., 2009). Using conventionally defined frequency bands, we find SChI stimulation increased alpha oscillations (8–15 Hz) in striatum but not in M1. Interestingly, the PD motor symptoms of bradykinesia and rigidity are correlated with elevated beta oscillations in basal ganglia that can extend down to 8 Hz and, thus, includes the alpha frequency range (Kuhn et al., 2006; Kuhn et al., 2009).

To determine the contributions of cholinergic receptor subtypes toward beta oscillation generation, we incorporated pharmacological techniques into our present study. Local infusion of scopolamine, a muscarinic receptor antagonist, in the striatum not

only reduced oscillation powers across all frequencies analyzed, but also drastically reduced the evoked beta and gamma oscillations upon optogenetic stimulation of SChIs.

In contrast, scopolamine did not alter SChI-induced high gamma oscillations, suggesting a mechanistic separation between the generators of beta/low gamma and high gamma oscillations. In contrast, the nicotinic receptor antagonist mecamylamine failed to change SChI-induced elevation of beta, low gamma, or high gamma oscillations in either the striatum or M1. These results demonstrate that SChIs exert rapid and powerful control over the dynamic generation of beta and gamma oscillations both within the striatum and throughout the CBT network through muscarinic mechanisms.

Beta frequency oscillations are found in the basal ganglia and the cortex of PD patients (Stein and Bar-Gad, 2013; Pollok et al., 2012) and PD animal models (Mallet et al., 2008; Stein and Bar-Gad, 2013; Devergnas et al., 2014). Beta elevation correlates with the PD motor symptoms of bradykinesia and rigidity. The multiple plastic changes seen throughout the CBT loop due to chronic loss of dopamine are not present in our current experiments, and we do not consider the SChI stimulation state equivalent to the Parkinsonian state. Nevertheless, it is interesting that some Parkinsonian phenomenology (elevated beta and hypokinetic movement) was evident during SChI stimulation despite normal dopaminergic function and lack of Parkinsonian plastic changes. Interestingly, one recent study demonstrated that optogenetic inhibition of SChIs alleviated some Parkinsonian motor symptoms in 6-hydroxydopamine (6-OHDA) mice (Maurice et al., 2015). Together, these findings suggest that the CBT network components that modulate beta oscillations in normal states may be operational, but unmodulated, in PD states.

Striatal manipulations often produce alterations in behavior that generally can be

classified as either hyperkinetic or hypokinetic. Examples of striatal perturbations resulting in hyperkinesia include inhibition of striatal fast spiking (FS) interneurons (Gittis et al., 2011), optogenetic stimulation of D1 medium spiny neurons (MSNs) (Kravitz et al., 2010), and intrastriatal infusion of amphetamine (Wang and Rebec, 1993). In contrast, hypokinetic movements are produced by optogenetic stimulation of striatal D2 MSNs (Kravitz et al., 2010). Here, we demonstrated that stimulation of SChIs also resulted in hypokinetic movements, highlighting a prominent role of SChIs in modulating basal ganglia network dynamics. We note that a recent study reported a lack of movement changes upon optogenetic simulation of SChIs in virally labeled animals (Maurice et al., 2015). It is possible that sufficient activation of SChIs is needed to produce an observable behavioral effect, and our experimental conditions using transgenic mice may allow us to activate sufficient numbers of SChIs to bias behavior.

Interestingly, we observed unexpected changes in rotational behavior in both directions after unilateral SChI stimulation. It is possible that unilateral stimulation of SChIs could engage not only the ipsilateral CBT loop but also the contralateral CBT loop through M1 bilaterally projecting intra-telencephalic neurons (Shepherd, 2013). Alternatively, because both ACh and glutamate are released from SChIs (Higley et al., 2011) and can potentially activate both D1 and D2 populations of MSNs, it is also possible that the direction of rotation depends on the relative excitation level of these two populations.

Although the source of the exaggerated beta oscillations in PD has not yet been established, we suggest here that it may consist of multiple, interacting sources. At least two independent beta generators are suggested by the distinct time course of coherence between deep layers of M1 and the striatum upon SChI activation, with coherence at higher beta frequencies of 22–30 Hz increasing and then rapidly dissipat-

ing, and coherence at lower beta frequencies of 15–22 Hz staying elevated throughout SChI activation. The dissipating coherence in the high beta frequency range despite consistently elevated beta power suggests at least two independent sources of high frequency beta, possibly one from basal ganglia networks and another in M1. An independent beta generator in M1 is consistent with in vitro work, demonstrating that deep layers of M1 can generate high frequency beta oscillations (27 Hz) in layer V in the presence of carbachol and kainate (Yamawaki et al., 2008). Additionally, we observed decreased coherence between striatum and superficial M1 throughout the entire beta frequency range (15–30 Hz) despite significant increases in beta power in these structures upon SChI stimulation, suggesting an additional source of beta oscillations within the CBT loop. It has been observed that both high and low frequency beta oscillations are elevated in the basal ganglia in Parkinsonian states and are correlated with different PD motor symptoms (Toledo et al., 2014). The observed dissociation of different frequency beta oscillations here, in normal mice with elevated striatal cholinergic tone, may indicate possible distinct network sources that generate PD-related betaband oscillations.

Whereas the literature proposes several putative mechanisms of CBT loop beta oscillation generation, our previous work suggests that networks of striatal MSNs can produce beta oscillations with sufficient MSN excitation (McCarthy et al., 2011). Because muscarinic receptors can increase MSN excitability by decreasing the M-current, our computational model predicts that muscarinic receptor blockade will interfere with the beta-producing mechanism in the striatum. This mechanism is supported by the experimental results of the present study demonstrating that striatal muscarinic blockade significantly decreases SChI stimulation-induced beta oscillations in the striatum. If the beta-producing mechanism of high striatal cholinergic tone plays a role in PD, our work suggests that modalities reducing striatal cholinergic tone

may be instrumental in alleviating excessive beta oscillations in the Parkinsonian CBT loop, along with their correlated motor symptoms. In fact, systemic antimuscarinic drugs were the sole pharmacologic treatment for PD until the late 1960s, when L-dopa was introduced (Fox, 2013), although their clinical use is limited by neuropsychiatric and cognitive side effects (Katzenschlager et al., 2003).

The literature proposes two other origins of pathologic beta oscillations in PD: the subthalamic nucleus (STN)-globus pallidus externa (GPe) circuit (Holgado et al., 2010) and M1 (Yamawaki et al., 2008). The former hypothesis depends on the presence of plastic changes attributable to chronic loss of dopamine in the STN-GPe network. Such mechanisms may be applicable to the Parkinsonian state. However, our results suggest that neither chronic plastic changes nor chronic low dopamine is needed to produce robust beta oscillations within the CBT loop upon SChI stimulation. We note that a similar finding is evident in M1, where robust beta oscillations can emerge in nonParkinsonian M1 slices in the presence of sufficient excitation with carbachol and kainate (Yamawaki et al., 2008; Lacey et al., 2014). Excitation of M1 neurons occurs in response to increased D1 MSN spiking and can also occur transiently to a subset of M1 neurons in response to D2 MSN spiking (Oldenburg and Sabatini, 2015). To what extent M1 generated beta oscillations are induced under the conditions of SChI stimulation is an interesting topic of future study. Excitation to M1 during SChI stimulation may depend on the amount and timing of excitation provided to D1 versus D2 MSNs (Oldenburg and Sabatini, 2015).

Recent studies (Bar-Gad et al., 2004; Tachibana et al., 2011) showed that microinfusions of GABAergic antagonists in GPe failed to reduce beta oscillatory activities at the site of infusion in 1-methyl-4-phenyl-1,2,3,6tetrahydropyridine (MPTP) neurotoxin-induced Parkinsonian monkeys, although infusion of glutamatergic antagonists in GPe and STN reduced beta oscillations. These results are consistent

with the view that the striatum is a source of beta oscillations, whereas the STN-GPe network serves as an amplifier of the striatally generated oscillations. In our framework, mechanisms that decrease the activity of STN or GPe will compromise the beta amplification mechanism and, thus, decrease beta oscillations. Correspondingly, mechanisms that increase the connectivity of STN and GPe (e.g., suppression of GPe lateral inhibition with GABAergic antagonist) may increase beta oscillations. This observation, taken together with the fact that microinfusion of GABAergic antagonists blocks a small amount of striatal inputs to GPe, suggests that substantial change to GPe beta oscillatory activity would not be expected with the microinfusion experiments performed in refs: (Bar-Gad et al., 2004; Tachibana et al., 2011).

Although much of the oscillatory spectrum in striatum is elevated during SChI stimulation, these elevations do not occur across the entire frequency range and, thus, are not considered a broadband increase in power. In contrast, scopolamine infusion decreased power at all frequencies, as expected with a broadband decrease (Figure 2·7A). However, in the presence of scopolamine, SChIs remained as effective as in the absence of scopolomine in elevating high gamma oscillations, but not beta or low gamma, suggesting a mechanistic separation between the generators of these frequencies. Additionally, coherence between striatum and the deep layers of M1 increased for beta and low gamma, but not high gamma, despite increases in power in both structures in all these frequency bands. Thus, beta and low gamma elevations appear to be both selectively elevated and coordinated in the CBT circuit during SChI stimulation, whereas high gamma may represent increased neuronal excitability (Manning et al., 2009).

SChI activation also produced electrophysiological effects that are not commonly observed in PD, including gamma power (30–100 Hz) elevation in cortex and striatum. Finely tuned gamma oscillations in the range of 60–90 Hz are a consistent feature of

basal ganglia and thalamic recordings (Jenkinson et al., 2013) that are diminished in PD patients in the absence of dopaminergic replacement (Brown et al., 2001; Kempf et al., 2009). However, rather than an increase in finely tuned gamma, here we observed a broader-band gamma power increase, which may represent a general increase in neuronal activity (Manning et al., 2009). Laserinduced striatal high gamma oscillations remained elevated after either muscarinic or nicotinic blockade, suggesting that ACh is not involved in the generation of striatal high gamma oscillations. Glutamate, which is also coreleased from SChIs, may be responsible for the increase in high gamma oscillations during SChI stimulation (Higley et al., 2011). Striatal low gamma oscillations, however, are more correlated with beta in our current study, consistent with that observed in the basal ganglia of rats (Leventhal et al., 2012). While it is unclear how low gamma is generated in the CBT circuits, evidence from the ventral striatum of rats have suggested that low and high gamma have distinct sources, with dopaminergic drugs selectively diminishing the power of low gamma and enhancing the power of high gamma (Berke, 2009). In addition, low and high gamma oscillations are increased at different times during a spatial decision task (van der Meer, 2009), likely coordinated by different sets of FS interneurons (Berke, 2009; van der Meer, 2009). Further work is required to delineate the mechanisms that result in increased M1 low and high gamma oscillatory activity due to increased striatal cholinergic tone.

Interneurons represent a small proportion of striatum, but these neurons can strongly modulate striatal output. The proportion of interneurons in striatum is 4-5% in mouse, >23% in monkey (Graveland et al., 1985), and up to at least 25% in human (Graveland et al., 1985), suggesting a more prominent role for striatal interneurons in nonhuman primates and humans. The majority of GABAergic interneurons in the striatum are parvalbumin-positive FS interneurons, which project primarily to the MSNs. Although FS interneurons are excited by nicotinic agonists (Koos and Tep-

per, 2002), optogenetic activation of SChIs failed to increase FS interneuron spiking in one study (English et al., 2011). Additionally, optogenetic stimulation of SChIs in ChAT-ChR2 mice elicits both fast and slow inhibitory postsynaptic potentials in MSNs by nicotinic-mediated GABA release from dopamine projections to striatum (Nelson et al., 2014) and neuropeptide Y-expressing neurogliaform GABAergic interneurons, resulting in inhibition of MSNs (English et al., 2011). However, nicotinic receptors generally quickly desensitize and, thus, we did not expect GABAergic blockade of MSN spiking to continue through the 5 s of stimulation used in our current study. Accordingly, our study reveals that nicotinic receptor blockade by mecamylamine did not change the spectral profile of either beta or gamma oscillations in the striatum or cortex over 5-s periods. This result suggests that SChI-induced GABA release does not exert long-term control over the SChI-induced oscillations along the corticostriatal circuit.

In contrast, we show that SChI-induced elevation of beta and low gamma oscillations depends on muscarinic receptors, because striatal scopolamine infusion lowered SChI-induced spectral power elevations of these oscillations. ACh acts through muscarinic receptors present on MSNs to decrease the activity of KCNQ (M-current) and Kir2.3 channels, thereby increasing MSN excitability (Shen et al., 2005; Shen et al., 2007). In addition, ACh also works through muscarinic receptors to inhibit the release of glutamate from corticostriatal terminals and GABA from striatal FS cells (Koos and Tepper, 2002; Higley et al., 2009). Thus, muscarinic receptor activity diminishes the impact of glutamatergic and GABAergic input on MSNs while simultaneously increasing the excitability of MSNs. Therefore, muscarinic receptor activation could potentially accentuate the intrinsic dynamics of the MSN network.

It is surprising that stimulation of a single interneuron type, SChIs, can reversibly reproduce some of the key electrophysiological and behavioral manifestations of PD in

normal mice, including increased beta oscillations in corticostriatal circuits, increased coherence between the cortex and the basal ganglia, and decreased mobility. SChI stimulation also increased rotational behavior, a phenotype often observed in mice rendered Parkinsonian by a 6-OHDA lesion (Deumens et al., 2002). These results suggest that the exaggerated beta oscillations in PD may reflect an uncontrolled expression of a normal dynamical state of the CBT network, a state that is directly modulated by SChI excitability.

In summary, we provide evidence supporting the existence of a beta frequency pacemaker within the CBT loop that can be activated by stimulation of striatal cholinergic interneurons via striatal muscarinic receptors. Our results suggest that the beta oscillations in PD may be an overexpression of normal CBT network dynamics due to a striatal dopamine/ACh imbalance, rather than a de novo oscillation due to a PD-induced network pathology.

Chapter 3

A Computational Study of Intrathalamic Vasoactive Intestinal Peptide

3.1 Abstract

Studies examining neural mechanisms of sleep and general anesthesia typically ignore the presence of intrinsic neuromodulation in thalamus. The thalamic reticular nucleus (TRN) is considered a source of inhibition for thalamus, yet it releases the neuromodulator vasoactive intestinal peptide (VIP) that depolarizes thalamocortical neurons *in vitro*. Specifically, VIP activates the cyclic adenosine monophosphate (cAMP) pathway known to augment the excitatory H-current of HCN pacemaker channels. While intrathalamic VIP is known to cause long-lasting excitation *in vitro*, its *in vivo* dynamical effects have not been reported. Here, biophysical Hodgkin-Huxley-like conductance-based computational models are used to elucidate the impact of intrathalamic VIP on thalamocortical dynamics during sleep and propofol general anesthesia. Importantly, multiple timescales of VIP effects are included to represent different cAMP actions within the cell. The findings suggest that VIP homeostatically drives thalamus toward the edge of a firing mode transition between the burst mode, characteristic of sleep and anesthesia, and the tonic relay mode of awake states. This mechanism contributes to different features of sleep depending on the timescale of intracellular effects. Multi-hour timescale effects lead to the empirically observed trend of decreasing ratio of stage 3 non-rapid-eye-movement sleep

(NREM3) to NREM2 sleep during successive sleep cycles. Effects on the 90 minute timescale cause NREM3 to NREM2 transitions. Seconds timescale effects represent a new biological spindle mechanism that enhances spindle robustness compared to previous computational models. Finally, propofol anesthesia both directly and indirectly counteracts VIP's effects, maintaining thalamus in a sustained burst mode unsupportive of consciousness. Inhibition of intrathalamic VIP homeostasis represents a novel mechanism contributing to propofol-induced loss of consciousness.

3.2   Introduction

Research on the neuromodulatory mechanisms of sleep and general anesthesia has often focused on changes in brainstem neuromodulators affecting the thalamus and cortex. For example, the effects of acetylcholine, adenosine, dopamine, histamine, norepinephrine, and serotonin on cortex and thalamus have been studied extensively (McCormick, 1992; Franks, 2008; Brown et al., 2010). However, the presence of intrinsic thalamic neuromodulators like vasoactive intestinal peptide (VIP) has been mostly neglected, despite several papers reporting VIP-mediated long-lasting thalamic excitation and firing mode changes (Lee and Cox, 2008; Lee and Cox, 2006; Lee and Cox, 2003; Sun et al., 2003). While several papers have explored these potent VIP effects *in vitro*, no experiments have examined the effects of intrathalamic VIP *in vivo*.

In addition, VIP may affect multiple intracellular targets with differing kinetics. However, it would be difficult using current experimental methods to separately examine VIP's effects on different timescales. This provides an opportunity to use computational models to explore the impact of different timescales of VIP activity on thalamocortical dynamics.

Here, biophysical Hodgkin-Huxley-like conductance-based computational models

are used to determine the implications of multiple timescales of VIP effects on thalamocortical dynamics during sleep and propofol general anesthesia. To the best of my knowledge, the modeling of multiple timescales of a single neuromodulator is a novel technique for this branch of computational neuroscience that simulates conductance-based models. An additional advantage of starting with a computational model is that it inspires specific predictions that can guide judicious use of physical resources when testing new hypotheses and exploring new areas, as in this case.

3.2.1 VIP Co-release from TRN

The thalamic reticular nucleus (TRN), the thin outer shell of thalamus, is the only thalamic nucleus that lacks efferent connections to regions outside of thalamus. Instead, it uniquely projects widely within thalamus and via GABAergic inhibition serves a synchronizing role similar to that of inhibitory interneurons in other brain regions like cortex (Pinault, 2004). This inhibition is mediated by γ-aminobutyric acid (GABA)-A and -B receptors on other TRN and thalamocortical (TC) relay neurons, with timescales of tens and hundreds of milliseconds, respectively (Destexhe et al., 1994).

Complicating this standard inhibitory TRN perspective, TRN co-transmits excitatory vasoactive intestinal peptide (VIP) (Kaneko et al., 1985)(see section 3.2.5). VIP mediates its excitatory effects in TC relay cells on the timescale of seconds to minutes, and likely hours as well (Lee and Cox, 2003; Sun et al., 2003). The latter timeframe is plausible, given that VIP-mediated effects in other nuclei last up to a week (Bourgin et al., 1997).

Even though other brain circuits (including those related to arousal) also co-transmit traditional neurotransmitters along with neuropeptides, the functional implications of this phenomenon remain poorly understood (Vaaga et al., 2014). Here, the potential impact of thalamic dual neurotransmitter-release on thalamocortical

dynamics is described.

3.2.2 VIP's Intracellular Mechanism

Synaptic VIP from TRN produces its effects via G protein-coupled transmembrane receptors on TC cells. VPAC1 and VPAC2 are the predominant VIP receptor types in relay thalamus, although other receptors including PAC1 are also present (Joo et al., 2004; Laburthe et al., 2002). VIP-mediated G protein activation increases the concentration of cyclic adenosine monophosphate (cAMP), a ubiquitous mediator of many cellular signaling cascades (Sun et al., 2003); intracellular calcium can also increase cAMP (Luthi and McCormick, 1999). These two methods of cAMP amplification will be compared regarding their ability to regulate thalamic spindle dynamics in section 3.3.1.

Among its diverse effects, cAMP augments the excitatory hyperpolarization-activated non-selective cation H-current of HCN channels, the same pacemaker channel responsible for the funny current in the heart (Budde et al., 1997)(Figure 3·1). This effect is mediated by cAMP binding the HCN cyclic nucleotide binding domain (CNBD) (He et al., 2013).
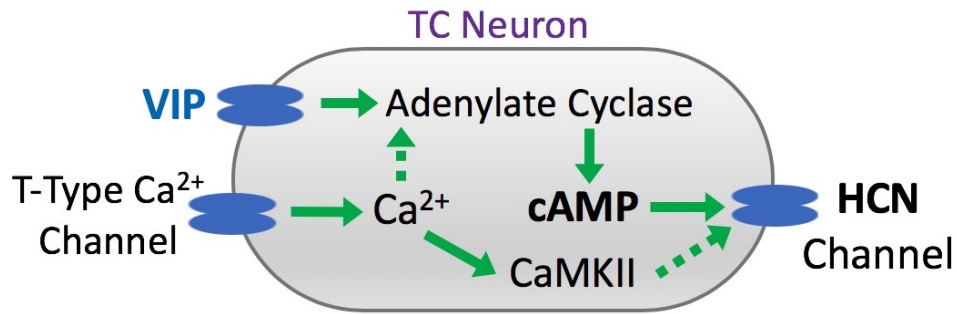
Figure 3·1: Intracellular mechanisms of HCN modulation in thalamocortical neurons. VIP stimulates adenylate cyclase (AC) to produce cAMP. cAMP increases the H-current conductance of HCN channels. In a separate mechanism, calcium influx from T-type calcium channels can also activate some adenylate cyclase isoforms to produce cAMP. Alternatively, calcium may modulate HCN channels directly via complexing with a protein like CaMKII. Solid lines are known interactions, while dashed lines are plausible interactions relevant to HCN modulation.

3.2.3 Multiple cAMP Timescales From Compartmentalization

Consistent with the notion that cAMP molecules are able to simultaneously control different functional pathways in cells with temporal and spatial precision, a given stimulus can generate differing cAMP responses in different microdomains (Zaccolo et al., 2000; Rich et al., 2001; DiPilato et al., 2004). Specifically, cAMP has varying concentration ranges and kinetics in different subcellular compartments or microdomains (Wachten et al., 2009; Zaccolo, 2011; Lefkimmiatis and Zaccolo, 2014), as outlined in Figure 3·2. This supports the incorporation of multiple cAMP timescales in my model, further discussed in sections 3.2.4 and 3.2.7.

As depicted in Figure 3·3, subcompartments are created by varying combinations of cAMP buffers, various isoforms of transmembrane and soluble adenylate cyclases that make cAMP, different phosphodiesterases (PDEs) that degrade cAMP, and protein scaffolds that bind cAMP protein machinery in a local area (Calebiro and Maiellaro, 2014). For example, experimental data depicted in Figure 3·4 demonstrates that two different adenylate cyclase (AC) isoforms both located at the cell membrane respond to VIP stimulation with differing kinetics, and lead to different cAMP concentrations over time (Zaccolo et al., 2000).

cAMP concentrations can oscillate intrinsically or due to external inputs. While differing oscillatory frequencies of cAMP can yield unique intracellular effects (Dyachok et al., 2006), even the same cAMP input frequency can have heterogeneous effects at different intracellular targets (Ni et al., 2010). This is relevant since the different sleep stages examined here correspond to differing synaptic input frequencies to thalamic cells, and secondly because the main results correspond to different oscillatory frequencies of cAMP. This corresponds to modulation of HCN channels at different timescales simmutaneously.
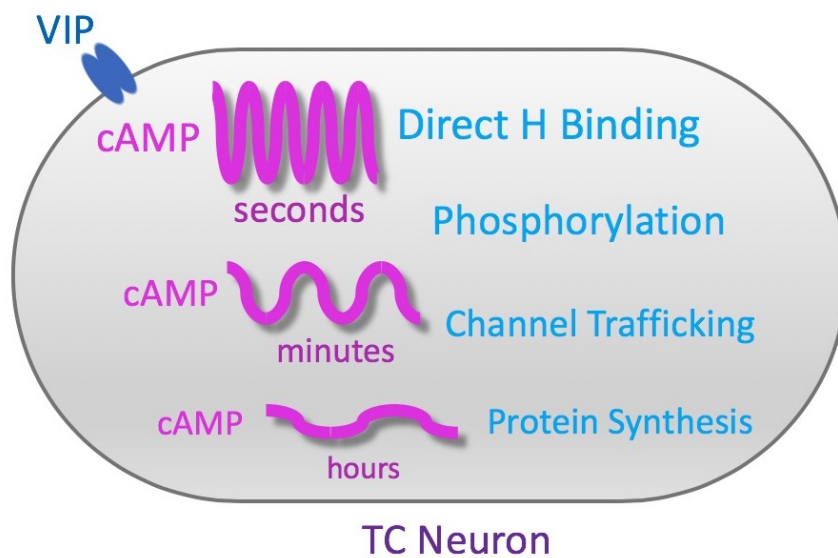
Figure 3·2: Different timescales of VIP's intracellular actions. VIP activity on TC cells leads to cAMP production. cAMP has been observed to maintain different kinetics and concentration ranges in different subcellular compartments, including different parts of the cell membrane, cytoplasm, mitochondria, and the nucleus. In addition to different cAMP timescales, cAMP's intracellular actions possess different intrinsic timescales (example actions in blue text; H binding refers to HCN channel binding). This 2-stage mixing of timescales (cAMP microdomain concentrations and actions) may enable cells to have diverse output activity timescales.
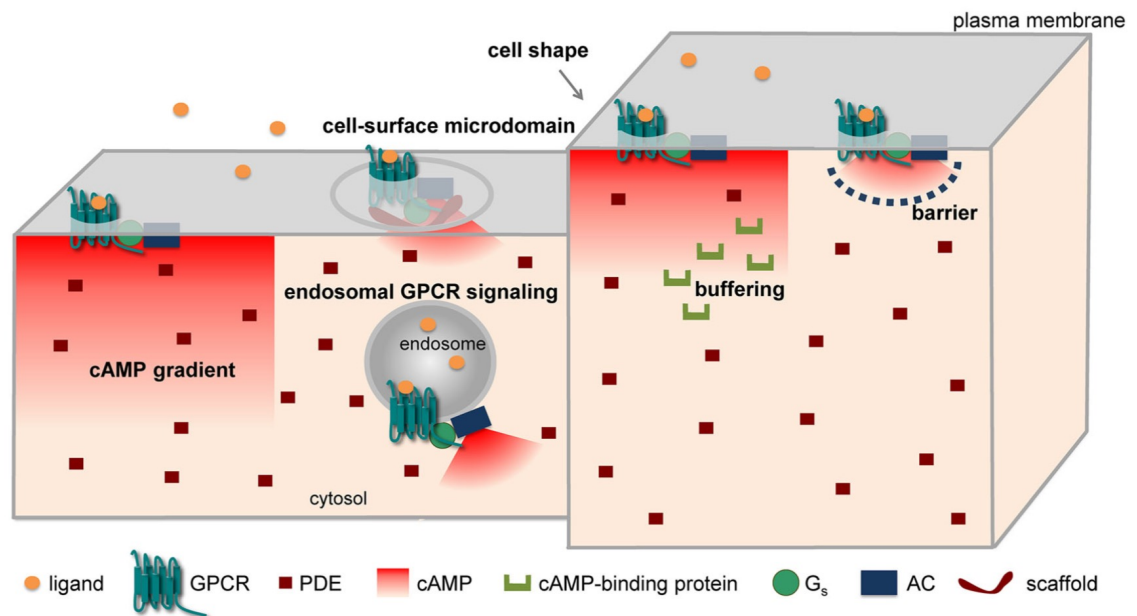
Figure 3·3: Major mechanisms implicated in cAMP compartmentation. "Different mechanisms have been put forward to explain the compartmentation of cAMP/PKA signaling in spite of the high diffusibility of cAMP in solution. These include the formation of cAMP gradients due to reaction-diffusion mechanisms, a different subcellular localization of signaling molecules (receptors, ACs, PDEs, etc.), factors (e.g., phyisical barriers, buffering, higher viscosity) capable of hindering the diffusion of cAMP, and the association of signaling molecules into supramolecular complexes, often through the intervention of scaffolding proteins" (Calebiro and Maiellaro, 2014).
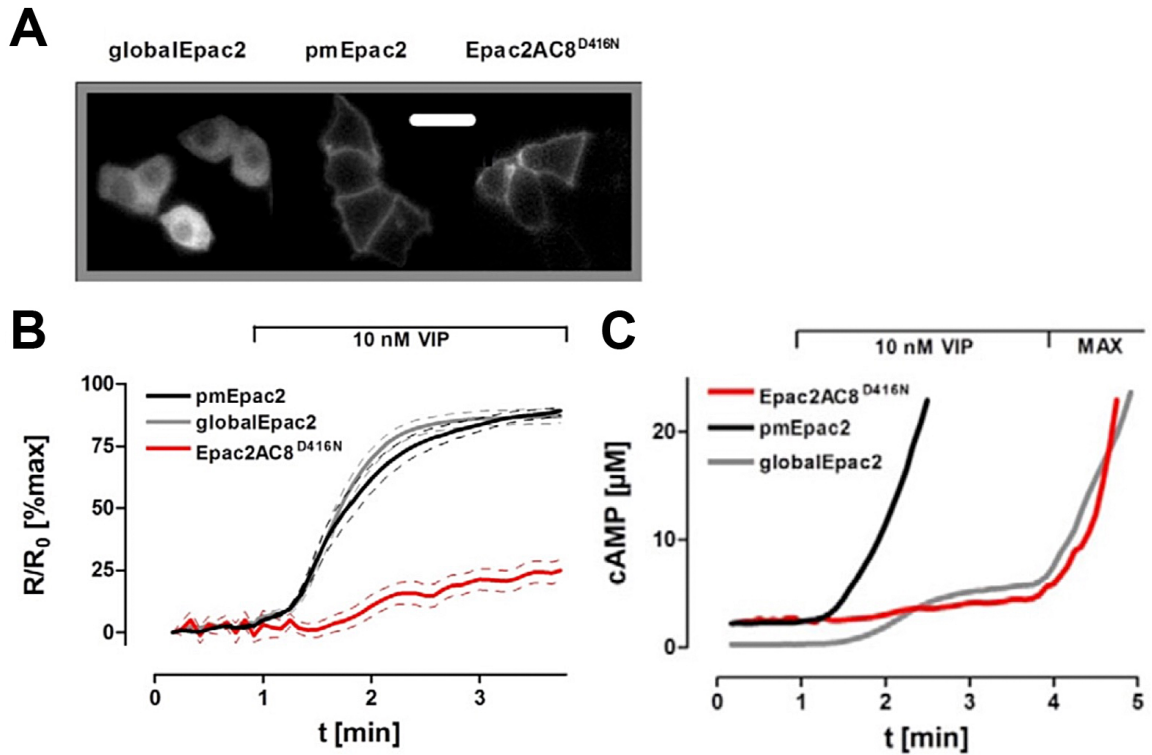
Figure 3·4: Differing kinetics of *in vitro* cAMP microdomains in pituitary cells. (A) Adenylate cyclase (AC) protein expression detected by fluorescence resonance energy transfer (FRET). globalEpac2 is found throughout the cytosol whereas pmEpac2 and Epac2AC8 isoforms are both localized to the cell membrane. (B) Change in AC FRET response after treatment with 10 nM VIP. (C) Change in calculated [cAMP] after treatment with 10 nM VIP. In both B and C, notice that the membrane-associated isoforms have differing kinetics. Adapted from (Zaccolo et al., 2000)

3.2.4 Multiple Timescales of H-Current Modulation by cAMP

In addition to the differing cAMP concentration kinetics due to subcompartments, cAMP's intracellular actions possess differing intrinsic timescales. Hence, HCN modulation by cAMP could involve several mechanisms of different timescales, including phosphorylation, receptor trafficking (Shah et al., 2010), and nuclear transcription/-translation. HCN channels can be reversibly inactivated via phosphorylation (Jung et al., 2010; Arinsburg et al., 2006; Yu et al., 2004), a process that takes seconds or less (Sitaramayya and Liebman, 1983). HCN channels can also be reversibly trafficked from the membrane to intracellular vesicles, also referred to as endocytosis or internalization (Santoro, 2004; Hardel et al., 2008; Lewis et al., 2009). An example of the timing of ion channel trafficking is shown in Figure 3·5—internalization of potassium channels in hippocampal neurons took several minutes to achieve a large effect (Kim et al., 2007). The transcription, translation, and trafficking of new HCN proteins to the membrane would presumably take even longer, potentially hours. Hence, it is conceivable that VIP's modulation of H-current could have multiple components that span the time scale of seconds to hours. This key insight motivated my decision to include multiple timescales of intracellular second messenger activity here, discussed further in section 3.2.7. In the context of the model described here, the terms "VIP effects" and "cAMP" will be used interchangeably since they are combined into a single state variable.

3.2.5 *In Vitro* VIP Studies

To date, no studies have explored the specific effects of intrathalamic neuromodulation by VIP *in vivo*, although global VIP infusions demonstrate sleep architecture changes (see section 3.4.5). However, several *in vitro* studies using rat thalamic slices (Lee and Cox, 2008; Lee and Cox, 2006; Lee and Cox, 2003; Sun et al., 2003) have revealed
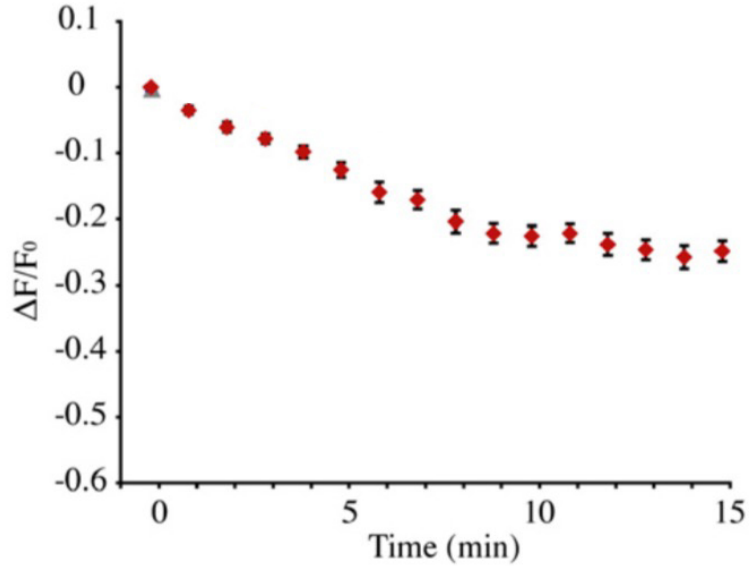
Figure 3·5: Voltage-gated A-type K^+ channel (Kv4.2) clathrin-mediated endocytotic internalization takes minutes to acheive a large effect in hippocampal neurons. "Time course of averaged fractional fluorescent changes ($\Delta F/F_0$) of Kv4.2g in spines. AMPA stimulation resulted in a progressive decrease of Kv4.2g-specific fluorescent intensity in spines." Modified from (Kim et al., 2007).

long-term depolarizations sufficient to cause firing mode changes (see section 3.2.6). The earliest paper to study VIP's effects on thalamic slices documented an increase in membrane potential that peaked at 6-8 mV and lasted 20 minutes after a 4 minute VIP infusion, shown in Figure 3·6B (Sun et al., 2003). VIP selectively depolarized TC but not TRN cells, suggesting that recurrent TRN connections lack VIP effects. The depolarization was reproduced by a similar set of experiments involving a 1 minute bolus infusion of VIP, leading to at least 5 minutes of increased membrane potential before washout (Figure 3·6A)(Lee and Cox, 2003).

In general, the higher VIP concentrations led to longer-lasting depolarizations of greater amplitude. Later work demonstrated a dose-dependence of the cAMP analog, 8-cpt-cAMP, on membrane depolarization amplitude and length, reaching up to 5 minutes with the tried doses (Lee and Cox, 2006). This study also implicated VPAC2 as the functionally dominant receptor of the VIP effects in thalamus.

Importantly, infusions with greater VIP concentrations revealed the presence of multiple timescales of depolarization (Lee and Cox, 2008). A 1 min 0.2 μM VIP infusion yielded a rise and fall of membrane potential lasting 2 minutes. Similarly, a 1 min 3 μM infusion showed a similar waxing and waning voltage, but maintained a slowly decaying voltage plateau that lasted at least 5 minutes. The presence of multiple voltage decay timescales supports the notion that VIP activates heterogenous cAMP targets within TC neurons, leading to H-current augmentation at different timescales.

These results were extended to peptide histidine isoleucine (PHI), a peptide sharing the same precursor as VIP, which is co-localized with VIP in the reticular nucleus (Lee and Cox, 2008) and also activates VPAC2 receptors, but with greater affinity (Harmar et al., 2012). Another homologous neuropeptide with similar actions is pituitary adenylate cyclase-activating polypeptide (PACAP), which has greater binding affinity for PAC1 receptors found in select thalamic regions, but equivalent affinity for VPAC1/2 receptors common in thalamus (Sun et al., 2003). Interestingly, VIP is located primarily in the dorsal sensory relay thalamus (Burgunder et al., 1999), while the more potent PACAP is found predominantly in the central thalamic nuclei involved in arousal (see section 3.2.11)(Koves et al., 1991), suggesting that VIP-mediated H-current modulation is more critical to the arousal system considered here. For the purposes of this model, PHI, PACAP, and VIP are considered equivalent and collectively referred to as VIP since they have equivalent actions given the model's granularity.

In addition, TC neurons from different thalamic nuclei and with differing morphologies responded to VIP similarly (Sun et al., 2003); thalamic regions tested included ventral posteromedial and ventral posterolateral (somatosensory), ventral lateral and ventral medial (motor), lateral geniculate (vision), as well as posterior

(i.e., pulvinar; visual attention)(Lee and Cox, 2008; Sun et al., 2003). While VIP's effects in intralaminar thalamus have not yet been reported, the presence of VIP in TRN regions projecting to intralaminar thalamus (Burgunder et al., 1999) as well as within intralaminar thalamus (Koves et al., 1991; Kaneko et al., 1985) suggests it would have similar effects. Thus, this H-current augmentation by intrathalamic VIP is likely a ubiquitous feature of non-TRN thalamus.
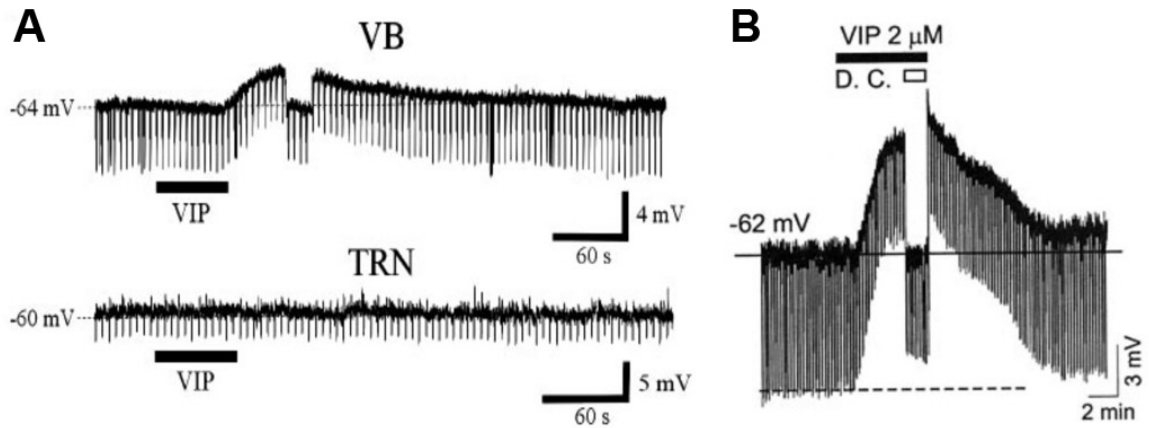
Figure 3·6: VIP depolarizes TC neurons *in vitro* for minutes. (A) 5 minutes of increased membrane potential after a 1 minute infusion of 0.5 μM VIP. Adapted from (Lee and Cox, 2003). (B) increase in membrane potential that peaked at 6-8 mV and lasted 20 minutes (beyond figure timespan) after a 4 minute 2 μM VIP infusion. Adapted from (Sun et al., 2003). Note that hyperpolarizations at peaks are due to injected current checking input resistance.

3.2.6 Thalamic Firing Modes

Thalamocortical neurons exhibit two firing modes, relay and burst (examples in Figure 3·7). In thalamus, relay mode is associated with depolarization and larger H-current characteristic of wakefulness, while burst mode is associated with hyperpolarization and lower H-current typical of non-rapid eye movement (NREM) sleep and anesthesia (Weyand et al., 2001). Incidentally, bursts also occur sporadically during wakefulness and may be important for attention (Llinas and Steriade, 2006).

The thalamic differences and switch between bursting/sleep and relay/awake states are commonly attributed to changing levels of brainstem neuromodulators that af-

fect multiple ion channels, especially the potassium leak currents that strongly affect membrane potential (McCormick and Huguenard, 1992). However, *in vitro* studies of intrathalamic VIP revealed an additional mechanism: VIP-mediated thalamic depolarization can shift firing mode from burst to tonic firing (Sun et al., 2003)(Figure 3·8). This is an exciting finding, since the literature otherwise discusses the switch between thalamic firing modes in the context of factors external to the thalamus, especially brainstem (McCormick, 1992; Sherman, 2001).
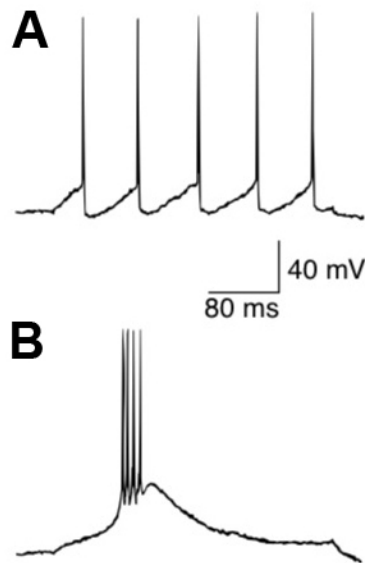
Figure 3·7: Intracellular recordings of a thalamocortical neuron from a cat thalamic lateral geniculate nucleus (LGN) *in vitro* slice. (A) Tonic spikes in relay mode. (B) Low-threshold spiking (LTS) in burst mode. Adapted from (Sherman, 2001).

In general, the level of thalamic depolarization determines the mode of thalamic spiking (Sherman, 2001). Awake states are associated with a depolarized thalamic relay mode, in which thalamus responds to weak inputs with single spike outputs (Ramcharan et al., 2000). In contrast, non-rapid eye movement (NREM) sleep and general anesthesia are characterized by a hyperpolarized burst mode consisting of low-threshold spiking (LTS), in which thalamus intrinsically oscillates with bursts of multiple spikes (Swadlow and Gusev, 2001). These bursts originate from an interac-
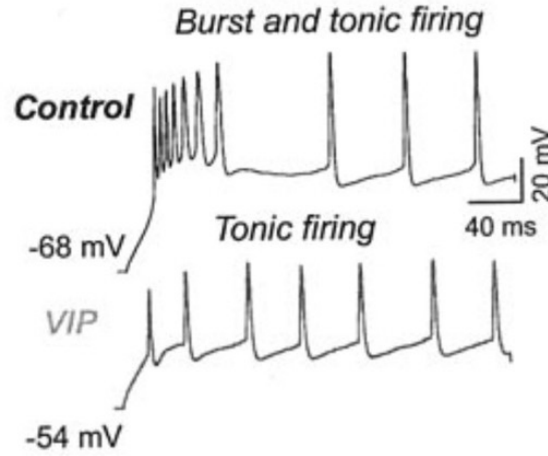
Figure 3·8: VIP induces a thalamic firing mode switch for *in vitro* thalamocortical neurons. The firing mode is revealed by a depolarizing step current after starting from a silent baseline state. Note the 6 mV difference in baseline voltage after the 2 μM VIP application. Adapted from (Sun et al., 2003).

tion between the positive cation pace-making H-current and T-type calcium channels (mechanism diagram and description in Figure 3·9)(McCormick and Pape, 1990).

3.2.7 Thalamocortical Computational Models

Previously, the thalamocortical circuit has been modeled extensively by Bazhenov, Destexhe, Kopell, McCormick, Rinzel, Sejnowski, Timofeev, and Wang (Bazhenov et al., 2002; McCormick and Huguenard, 1992; Destexhe et al., 1993a; Destexhe et al., 1993b; Wang et al., 1995; Destexhe et al., 1996; Terman et al., 1996; Lytton et al., 1997; Ching et al., 2010; Vijayan and Kopell, 2012; Soplata et al., 2017). These models have been useful for exploring mechanisms of sleep spindles (Destexhe et al., 1993b), absence seizures (Lytton et al., 1997), alpha-delta sleep common in fibromyalgia (Vijayan et al., 2015), awake alpha oscillations (Vijayan and Kopell, 2012), anesthetic alpha oscillations (Ching et al., 2010), and anesthetic phase-amplitude coupling (Soplata et al., 2017). Additionally, a recent modeling study simulated changes between sleep stages using simulated changes in brainstem neurotransmitters onto
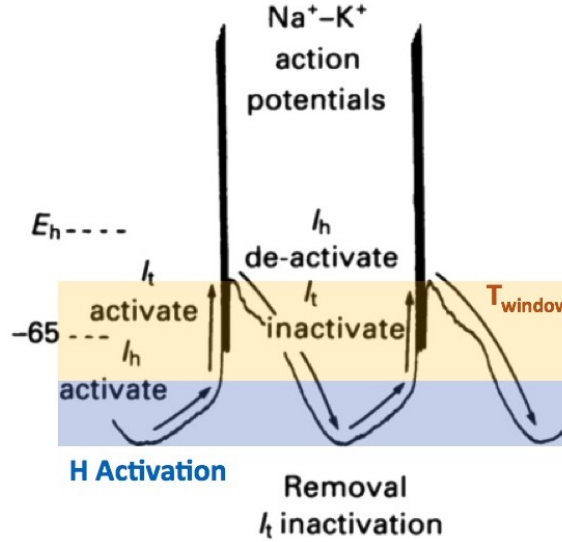
Figure 3·9: Low-threshold spiking (LTS) burst mechanism. The H-current pacemaker raises membrane potential (blue region) to the threshold for T-type calcium current activation (orange region). T-current creates to a plateau of depolarization crowned by sodium-potassium spikes. H-current deactivates and T-current inactivates from the high membrane potential. Resulting hyperpolarization removes T-channel inactivation (bottom edge of blue region) and H-current reactivates, leading to another cycle. Adapted from (McCormick and Pape, 1990).

cortex and thalamus (Krishnan et al., 2016); this model compressed hours of sleep into a 5 minute simulation, similar to the approach used here which is described in the methods section 3.6.1.

Importantly, these prior thalamic computational models have not included intrathalamic VIP-mediated modulation of H-current. Instead, the models made the simplification of directly modulating H-current conductance by calcium. The authors of these previous works recognized that calcium doesn't actually modify HCN channels directly in thalamus (Destexhe and Sejnowski, 2001), as demonstrated in rat thalamic neurons (Budde et al., 1997). Calcium does indirectly modulate HCN channels though, since it affects cAMP production via adenylate cyclase stimulation (Luthi and McCormick, 1999). However, the relative efficacy of calcium versus cAMP for modulating H-current is unknown. Incidentally, one study reported that in heart cells calcium may directly increase H-current conductance while cAMP may affect

HCN kinetics (Hagiwara and Irisawa, 1989).

Canonical Spindle Model

The calcium-mediated H-current augmentation model represents the canonical spindle mechanism (Destexhe et al., 1996)(Figure 3·10). Spontaneous continuous thalamic bursting during burst mode is silenced by T-current inactivation due to depolarization from calcium-mediated H-current augmentation. T-current is necessary for creating the depolarized plateaus that trigger bursts of spikes (see Figure 3·9). T-current is a key source of calcium, so its inactivation leads to calcium decay along with progressive hyperpolarization. With sufficient hyperpolarization T-current is de-inactivated, leading to the reemergence of a spontaneous bursting segment characteristic of spindles.
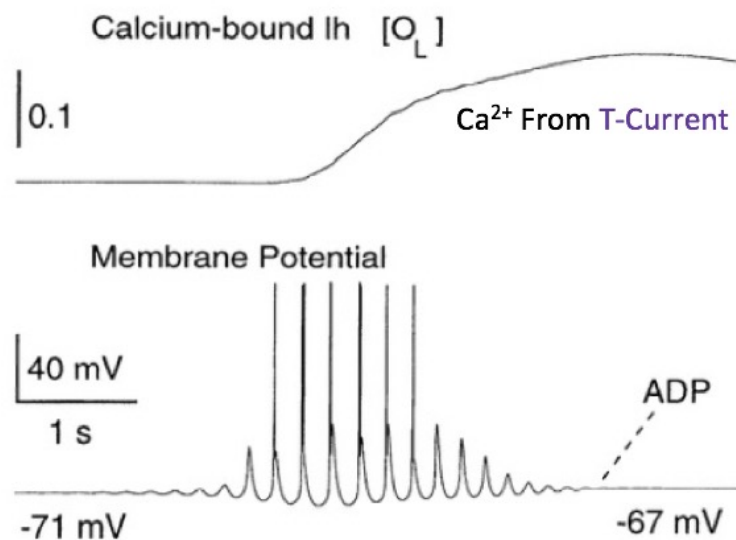
Figure 3·10: Calcium-mediated upregulation of thalamocortical cell H-current terminates spindles in a computational model. The top panel shows the trace for the calcium-bound open state which has twice the modulation capacity as the non-calcium-bound open state. See section 3.6.3 for more information. Adapted from (Destexhe et al., 1996).

3.2.8   Sleep

VIP's long-lasting thalamic depolarization in simple *in vitro* assays raise the question of how it affects *in vivo* thalamic dynamics. One interesting regime is that of sleep, since lower levels of excitation lead to a switch in thalamic firing mode to bursting, the firing mode associate with slow-wave sleep (section 3.2.6).

One question examined here is how VIP affects the sleep spindle oscillations characteristic of stage 2 non-rapid-eye-movement (NREM2) sleep. Spindles are α frequency (8-12 Hz) wave groups lasting several seconds and recurring periodically on the seconds timescale (Contreras et al., 1997). They have interested researchers since they correlate with declarative memory, learning capacity, and intelligence measures (Luthi, 2014; Fogel et al., 2007). While TRN bursting is important for spindling (Steriade et al., 1987; Halassa et al., 2011; Bartho et al., 2014), several computational models have focused on mechanisms within TC cells that control spindles (Destexhe et al., 1998; Destexhe et al., 1996; Wang et al., 1995; Destexhe et al., 1993b; Destexhe et al., 1993a). The canonical spindle mechanism (Destexhe et al., 1996) involves initiation by spontaneous TC bursting that terminates within several seconds after a depolarizing mode transition due to calcium-mediated H-current augmentation (see section 3.2.7).

Previous models have also demonstrated the capacity of thalamus to generate synchronized δ (1-4 Hz) oscillations, common in deeper NREM3 but also found sparsely in shallower NREM2 sleep (Destexhe et al., 1996). These models switch between the continuous bursts of NREM3 and the spindles of NREM2 by modulating H-current (Destexhe et al., 1993a). Notably, thalamic neurons empirically depolarize 8-12 mV when switching NREM to REM/wakefulness (Hirsch et al., 1983), which is a depolarization magnitude VIP is capable of achieving *in vitro*. Since VIP modulation of H-current can depolarize thalamic neurons enough to match changes between sleep

stages, another question addressed here is how VIP affects transitions between sleep stages.

Another phenomenon that VIP may impact is the trend of decreasing depth of sleep, i.e. decreasing NREM3 : NREM2 ratio, between successive ≈ 90 minute NREM–REM sleep cycles during the course of human sleep (depicted in Figure 3·11)(Scammell et al., 2017). Here, the question of whether long-term, i.e. multi-hour, timescales of VIP effects may contribute to this feature of sleep is evaluated. It is important to note that sleep architecture is species-specific (Genzel et al., 2014), and that this work focuses on human sleep.
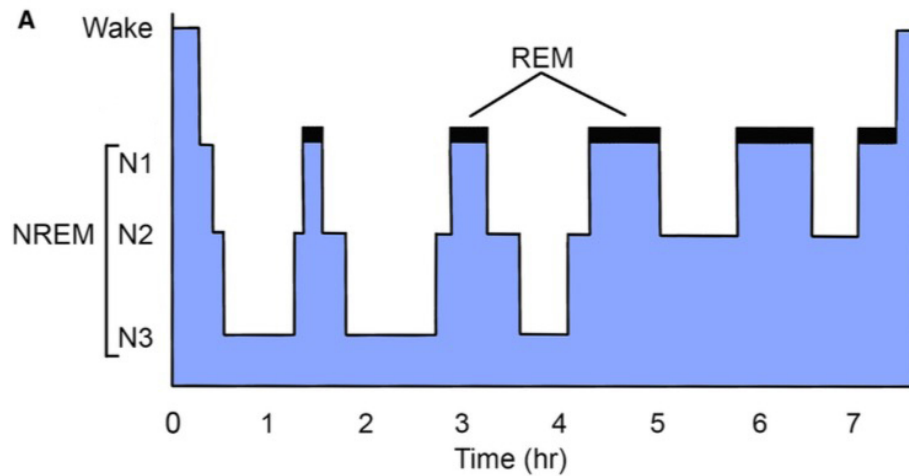
Figure 3·11: Diagram of human sleep architecture. During the course of sleep, there is a trend of decreasing depth revealed as a shift toward higher NREM sleep stages, increasing REM length, and increasing REM : NREM time ratios with each NREM–REM cycle. Adapted from (Scammell et al., 2017).

3.2.9 Sleep Regulation

There is an immense literature dissecting the circuit mechanisms of sleep. This has led to conceptual models implicating key regulatory roles for multiple brainstem nuclei as well as forebrain structures like the cholinergic basal forebrain and hypothalamus (Weber and Dan, 2016). However, while thalamus' role in arousal is often discussed

(see section 3.2.11), I am unaware of any theories of direct thalamic control of sleep architecture, a hypothesis explored here. What follows in this section is a summary of the sleep regulation literature to permit comparison with the notion of sleep architecture control by thalamus.

Sleep-Wake Control

Different neural regions promote wakefulness, NREM sleep, and REM sleep. Wake-promoting nuclei include the noradrenergic locus coeruleus (LC), serotoninergic dorsal raphe (DR), and histaminergic tuberomammilary nucleus (TMN); sleep-promoting populations include the GABAergic ventrolateral and medial preoptic areas (VLPO, mPOA) (Saper et al., 2001; Booth and Diniz Behn, 2014). Incidentally, while wakefulness and REM sleep are similar electrophysiologically, a key difference is that the ascending monoaminergic inputs (LC, DR, TMN) are silent in REM (Saper et al., 2001).

Mutually inhibitory connections between the wake- and sleep-promoting populations led to the bistable "flip-flop switch" hypothesis of wake-sleep control, with orexinergic neurons in lateral hypothalamus supporting the stability of each state (Saper et al., 2001). Improper orexinergic function causes narcolepsy, a medical condition characterized by aberrant transitions into REM sleep during wakefulness (Saper et al., 2001).

REM Control

Several nuclei are associated with REM sleep. Separate populations in hypothalamus are associated with NREM versus REM (Lu et al., 2000; Chen et al., 2018). Also, optogenetic activation of cholinergic pedunculopontine tegmentum (PPT) and laterodorsal tegmentum (LDT) neurons induces REM sleep (Van Dort et al., 2015). Conversely, activation of GABAergic neurons in the midbrain ventrolateral periaque-

ductal gray suppresses REM in favor of NREM sleep (Weber et al., 2018). Thus, one hypothesis is that mutually inhibitory REM-off and REM-on areas in the mesopontine tegmentum create a bistable "flip-flop switch" for NREM-REM control (Lu et al., 2006), separate from the "flip-flop switch" hypothesis of wake-sleep control.

A recent theory unifying sleep-wake and NREM-REM control is the arousal-action model (Liu and Dan, 2019). It expands upon the mutually inhibitory flip-flop models mentioned previously to include two classes of mutually excitatory wake-promoting neurons: *arousal* neurons that increase neural activity, and *action* neurons that both increase neural activity and activate muscles.

Local Cortical Sleep

The notion of local cortical control of sleep is an alternative although not mutually exclusive concept to that of brainstem control (Siclari and Tononi, 2017). This has been motivated by studies showing local cortical slow oscillations or cortical deactivations during prolonged wakefulness in various species. For example, during prolonged wakefulness in rats, localized cortical slow waves with neuronal deactivation are seen (Vyazovskiy et al., 2011). Similarly, local cortical deactivations have been seen in monkeys (Pigarev et al., 1997). Moreover, some species of birds and ocean mammals can maintain wakefulness while having one hemisphere engage in sleep (Lyamin et al., 2008). In humans, different regions of cortex enter sleep at different times, local "awakenings" can occur, and sleep tends to be fragmented across cortex (Nobili et al., 2012). The model here produces local spindles that suggest a role of local thalamic activations in local cortical sleep.

Computational Models of Sleep Regulation

A critical challenge in sleep physiology research is the limitations from *in vivo* protocols as well as the absence of sleep dynamics with *in vitro* assays. While investigations

have yielded conceptual models, the models lack a detailed description of network dynamics and temporal interactions. Computational models can overcome these obstacles and integrate different sources of information to improve understanding of sleep dynamics (Booth and Diniz Behn, 2014). They can demonstrate how interactions between different neural populations shape dynamics to achieve the observed sleep architectures. A brief history of sleep architecture models follows.

Early mathematical models were phenomenological. One example is the "two process model" of sleep regulation, in which a sleep-independent circadian process (Process C) and a sleep-dependent processes (Process S) interact to determine sleep propensity and duration (Borbély, 1982).

Later models represented more physiological detail. One of the first physiologically-based models is McCarley and Hobson's "reciprocal interaction model," which used Lotka-Volterra-type equations that were found in predator-prey models (McCarley and Hobson, 1975). They modeled oscillations between REM and NREM sleep states based on the interactions between the cholinergic pontine gigantocellular tegmental field and the noradrenergic locus coeruleus.

Current models focus on simulating neural population firing rates (Wilson-Cowan-type) or voltage traces (Morris-Lecar-type). Nearly all of these models include mutually inhibitory connections between wake-promoting and NREM sleep-promoting populations following the "flip-flop switch" hypothesis (Booth and Diniz Behn, 2014). Some models do not include REM sleep. Interestingly, one model is able to transition from the stereotyped human sleep structure to the highly-variable rodent architecture with a change of parameters and by increasing stochasticity (Gleit et al., 2013; Diniz Behn and Booth, 2010).

The thalamocortical model introduced here can regulate aspects of sleep architecture and differs critically from previous models of sleep regulation: it has more

biophysical detail and more completely describes the origin of the sleep timescales.

3.2.10   General Anesthesia

As with sleep, general anesthetic states correspond to distinct thalamocortical physiology and rhythms that have been studied extensively with computational models (Soplata et al., 2017; Ching and Brown, 2014; Vijayan et al., 2013; McCarthy and Kopell, 2012; Ching et al., 2012; Ching et al., 2010; McCarthy et al., 2008). Importantly, the cornucopia of general anesthetic agents differ greatly from sleep in their underlying mechanisms and phenotypes (Purdon et al., 2015; Akeju and Brown, 2017). GABA-potentiating anesthetics, like the commonly used propofol, are thought to achieve sedation by activating the endogenous sleep pathway (Nelson et al., 2002) and inhibiting targets across the brain and brainstem (Brown et al., 2010; Franks, 2008). In addition to high amplitude slow/delta waves also found in sleep, the electroencephalogram (EEG) under GABA-ergic anesthetics reveals strong frontal α oscillations (Purdon et al., 2015).

Of relevance to intrathalamic VIP, several anesthetic agents, including propofol, directly inhibit the TC neuron H-current that is normally augmented by VIP (Ying et al., 2006). The question of how propofol interacts with the effects of intrathalamic VIP is investigated here.

3.2.11   Thalamic Control of Arousal

In addition to shaping sleep and anesthetic dynamics, central thalamus is also recognized as exerting control over cortical arousal. For example, electrophysiological changes related to loss of consciousness in natural sleep and propofol general anesthesia have been observed in centromedial thalamus prior to cortex (Magnin et al., 2010; Baker et al., 2014; Gent et al., 2018), suggesting that thalamus plays a key role in controlling cortical arousal. This is reinforced by studies demonstrating the rever-

sal of general anesthesia, NREM sleep, and minimally conscious states by increasing excitation within centromedial thalamus (as opposed to brainstem or systemic alterations)(Gent et al., 2018; Alkire et al., 2009; Alkire et al., 2007; Schiff et al., 2007). GABAergic manipulations of central thalamus were also shown to control arousal and the threshold for seizures originating from other brain regions (Miller and Ferrendelli, 1990). From lesion studies, the degree of impairment to consciousness correlates with the extent of damage to central thalamic nuclei and their connections to other brain regions (Maxwell et al., 2006; Jennett et al., 2001). As for sleep induction, direct optogenetic activation of a portion of awake rat TRN induced a drowsy state (Lewis et al., 2015). Of note, other thalamic nuclei, e.g. somatosensory nuclei, are functionally separated with differing connectivity profiles, such that they do not seem to control arousal (Baker et al., 2014; Gent et al., 2018). However, the thalamic "matrix" regions in non-central thalamus project diffusely similar to central thalamus (Jones, 2001), and may contribute to arousal regulation (Honjoh et al., 2018).

While thalamus' role in arousal is often discussed, it remains unclear which specific aspects of arousal are controlled by the brainstem versus thalamus, and whether they can at least partially substitute for one another, analogous to the various potential pacemakers in the heart. These same questions of thalamus vs. brainstem are also relevant to sleep architecture regulation.

3.2.12 Present Work

While intrathalamic VIP is known to cause long-lasting excitation *in vitro*, its *in vivo* dynamical effects have not been reported. Furthermore, the implications of multiple timescales of VIP intracellular effects on thalamocortical dynamics is unclear.

Here, biophysical Hodgkin-Huxley-like conductance-based computational models are used to elucidate the impact of intrathalamic VIP on thalamocortical dynamics during sleep and propofol general anesthesia. Previous thalamocortical models

(Destexhe et al., 1996; Destexhe et al., 1998; McCarthy et al., 2008) were extended to include intrathalamic VIP as well as multiple timescales of VIP effects, representing different cAMP actions within the cell. The modeling of multiple timescales of a single neuromodulator is a novel technique for conductance-based modeling in computational neuroscience.

The findings suggest that VIP homeostatically drives thalamus toward the edge of a firing mode transition between the burst mode, characteristic of sleep and anesthesia, and the tonic relay mode of awake states. This mechanism contributes to different features of sleep depending on the timescale of intracellular effects. Multihour timescale effects lead to the empirically observed trend increasing ratio of stage 2 non-rapid-eye-movement sleep (NREM2) to NREM3 sleep during successive sleep cycles. Effects on the 90 minute timescale cause NREM2 to NREM3 transitions, typically thought to be controlled by brainstem (Saper et al., 2001). Seconds timescale effects represent a new biological spindle mechanism that enhances spindle robustness compared to previous computational models.

Finally, propofol anesthesia both directly and indirectly counteracts VIP's effects, maintaining thalamus in a sustained burst mode unsupportive of consciousness. Inhibition of intrathalamic VIP homeostasis represents a novel mechanism contributing to propofol-induced loss of consciousness.

3.3   Results

The role of intrathalamic vasoactive intestinal peptide (VIP) was studied using computational simulations of a thalamocortical model. The thalamic model incorporates two neuronal populations corresponding to different thalamic nuclei: (1) thalamocortical (TC) neurons representing the higher-older centromedial nucleus of the intralaminar thalamus important for arousal (Van der Werf et al., 2002; Baker et al.,

2014); and (2) thalamic reticular nucleus (TRN) neurons. This model was extended from the canonical thalamic model (Destexhe et al., 1996) to incorporate VIP activity from TRN, which promotes excitation of TC cells. The TRN model imparts 5 timescales of activity onto TC cells via 3 neurotransmitters: short inhibitory GABA-A ($\approx$10 ms), medium inhibitory GABA-B ($\approx$100 ms), and long excitatory VIP (three timescales ranging from seconds to hours). The cortical model also has two populations, representing excitatory regular spiking (RS) pyramidal neurons and inhibitory parvalbumin-positive fast-spiking (FS) interneurons, referred to as E and I cells, respectively. The model is comprised of 2 (or 20) neurons of each type, corresponding to 4 (8) and 40 (80) cell models for thalamic and corticothalamic models, respectively. For the thalamic model, AMPA-ergic TC relay neurons are mutually connected to GABA/VIP-secreting TRN neurons with all-to-all connections between all cells, except for the absence of TC-TC connections (Figure 3·33A). TC cells have both GABA-A and GABA-B receptors, as well as VIP receptors. The rest of the thalamocortical connections are shown in Figure 3·33B and all are described in more detail in section 3.6.6. In the context of the model described here, the terms "VIP effects" and "cAMP" will be used interchangeably since they are combined into a single state variable.

3.3.1 Short Timescale VIP Effects Create Robust Spindles

Using the isolated thalamus model, the impact of short timescale VIP effects on the order of seconds was investigated. Specifically, a 1 second time constant was used since spindles often last only a couple seconds (Contreras et al., 1997). This short timescale also maximized the separation from other time constants (see methods section 3.6.1). Simulations revealed that intrathalamic VIP represents a new biological mechanism for spindle generation (Figure 3·12), although it is mathematically analogous to the canonical calcium spindle mechanism (introduced in section 3.2.7 and

further described in the next section).

Comparison of VIP versus Calcium Spindle Mechanisms

The VIP and calcium mechanisms share many similarities. At a hyperpolarized membrane potential, continuous bursting starts spontaneously once the pacemaker H-current depolarizes the membrane potential into the window of T-current activation—T-current creates a depolarized plateau that triggers bursts of spikes (see Figure 3·9). Both mechanisms involve H-current augmentation, causing depolarization which inactivates T-current, reducing the depolarized plateau, and causing a period of silence characteristic of the inter-spindle interval.

The calcium mechanism involves the activated T-type calcium current increasing the calcium concentration at the inner membrane. Calcium binds a protein (assumed to be CaMKII), and as a complex allosterically binds to open HCN channels to create a locked-open state. In the model, the HCN conductance is further increased by the locked-open state versus the open state by a multiplicative factor (*caCoop* parameter). This soon depolarizes the cell outside of the T-current window, leading to the T-current inactivation. Calcium concentration decays, which frees calcium from HCN channels, permitting HCN channels to close. This hyperpolarizes the cell, enabling de-inactivation of T-current and a new round of bursting.

The VIP mechanism differs from the calcium one primarily in the biological description, but also in terms of implementation. With each TC burst, TRN also bursts, releasing VIP at the TC cell synapse. VIP increases the cAMP concentration via adenylate cyclase activation. cAMP binds to HCN channels at the cyclic nucleotide binding domain (CNBD), augmenting H-current. This causes depolarization which inactivates T-current and leads to silence of TC and TRN cells. TRN silence permits VIP, cAMP, and H-current decay leading to membrane hyperpolarization before a new bursting cycle.

In the model iH equation, the cAMP binding to HCN channels is not a separate state as with calcium, but instead is represented more parsimoniously by an additive term to the conductance ($campMult1 * campModNorm1$ term), since this avoids specifying two kinetic terms (analogous to $k3$ and $k4$) with unknown values (see appendix A).

Both mechanisms involve H-current augmentation to terminate spindles. Spindle termination is followed by an after-depolarization (ADP) silent period of slow repolarization as the H-current conductance decreases toward baseline due to inactivity. Once the membrane polarizes sufficiently, the T-current is de-inactivated.

Robustness of VIP versus Calcium Spindles

How does the robustness of the new VIP mechanism (Figure 3·13A) compare to the calcium-mediated spindles (Figure 3·13B) of the canonical TC model (Destexhe et al., 1996)?

To answer this question, spindle generation via H-current modulation by VIP, calcium, and their combination was tested over a 2-dimensional parameter space. Specifically, the two key parameters examined are the potassium leak conductance (gLeak; modified by neuromodulators extrinsic to thalamus), and the HCN conductance (gH; modified by both extrinsic and intrinsic neuromodulators like VIP). The leak is important for changing the membrane potential, which H- and T-current activation depends on. The H-current conductance affects not just the membrane potential, but also the TC cell depolarization rate which can affect the inter-burst interval and thus the frequency of bursts. These two currents are recognized in the literature as being efficacious in switching between different firing modes, including spindling (Soplata et al., 2017; Destexhe et al., 1996; Destexhe et al., 1993a).

Results are depicted in Figure 3·14. The VIP mechanism makes spindles much more robust in parameter space than did the calcium one (Figure 3·14, blue versus red
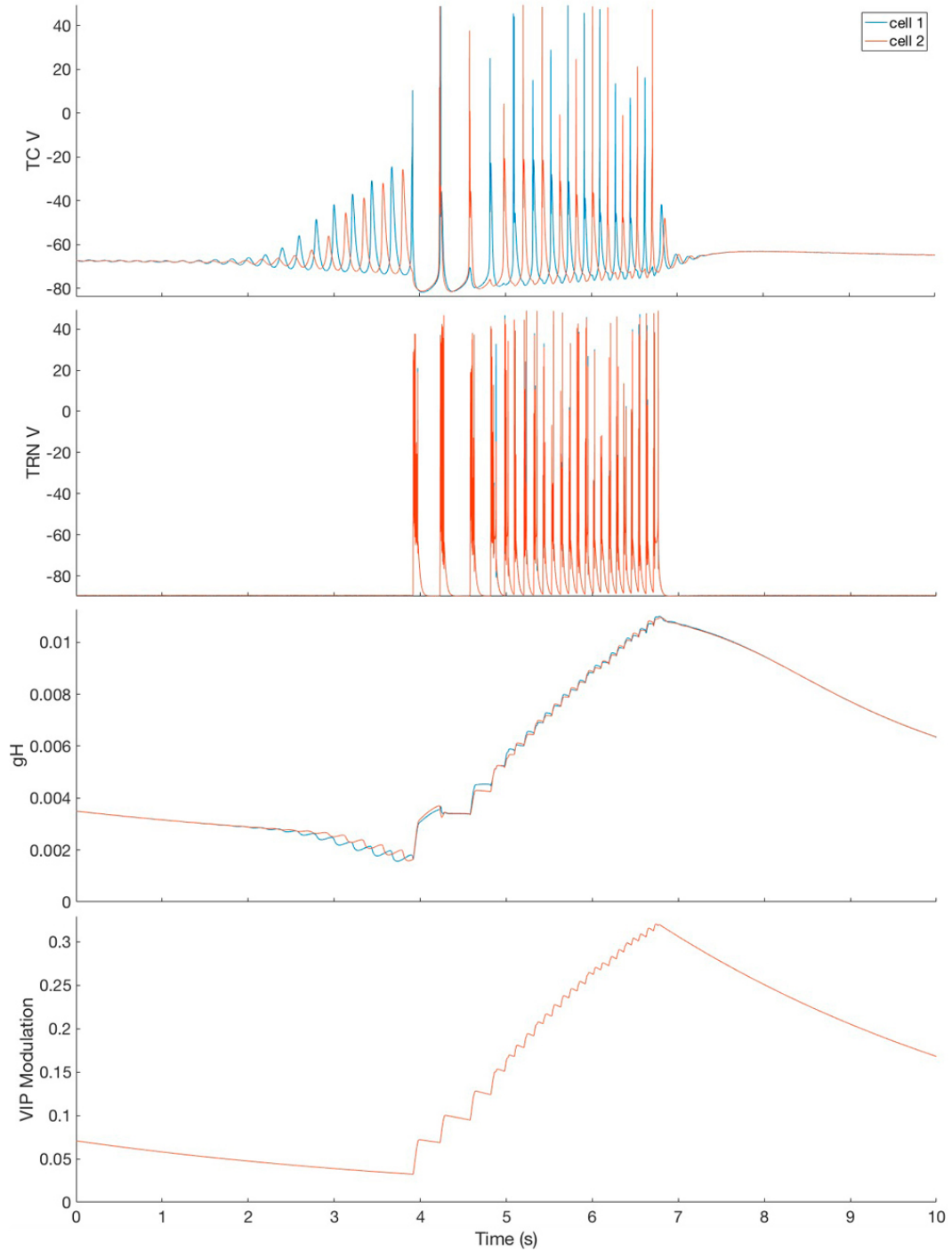
Figure 3·12: VIP HCN-modulation represents a new biological spindle mechanism. VIP augmentation of H-current terminates continuous bursting via depolarization block of the T-current, leading to the formation of a spindle. Pictured here is a 10 sec window around a 3 sec spindle (4–7 sec). Notice the after depolarization (ADP) following the termination of bursting in the top voltage panel. The third panel shows the H-current conductance (gH), which is modulated by VIP activity, shown in the bottom panel.
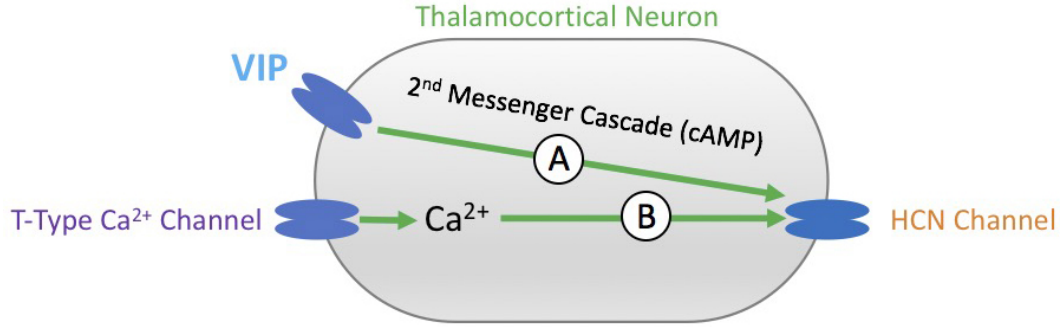
Figure 3·13: Two Types of H-Current Modulation in the TC neuron model. (A) VIP modulates H-current via cAMP. The model uses 1 to 3 cAMP pools with differing kinetics. (B) Calcium modulates H-current via a calcium-bound state.

region). Changing (increasing or decreasing) the magnitude of calcium-mediated H-current augmentation (*caCoop* parameter) in the locked-open state (*OpenCaLocked* state variable) only decreased the spindle robustness further. The addition of the calcium mechanism to the VIP one leads to a slight decrease in spindle robustness over that of VIP alone (Figure 3·14, green region versus blue). This is likely because the excess excitation from combining mechanisms predisposes the TC cells to tonic relay mode, preventing sufficient hyperpolarization to de-inactivate T-current needed for spindle bursts. In summary, VIP not only represents a new biological mechanism of spindle generation, but forms spindles that are much more robust to heterogeneity in key biophysical parameters.

Propagating Regular-Interval Spindles

Since a core aspect of spindles is their traveling wave propagation across thalamus and cortex (Golomb et al., 1996; Destexhe et al., 1996), spindle wave propagation with the new VIP mechanism was examined in the thalamus model with sparse 20% nearest-neighbor connections (instead of all-to-all connectivity). Since spatial wave propagation depends on synapses, two synaptic conductances were varied: TC $\rightarrow$ TRN gAMPA and TRN $\rightarrow$ TRN gGABA-A. These conductances were chosen because
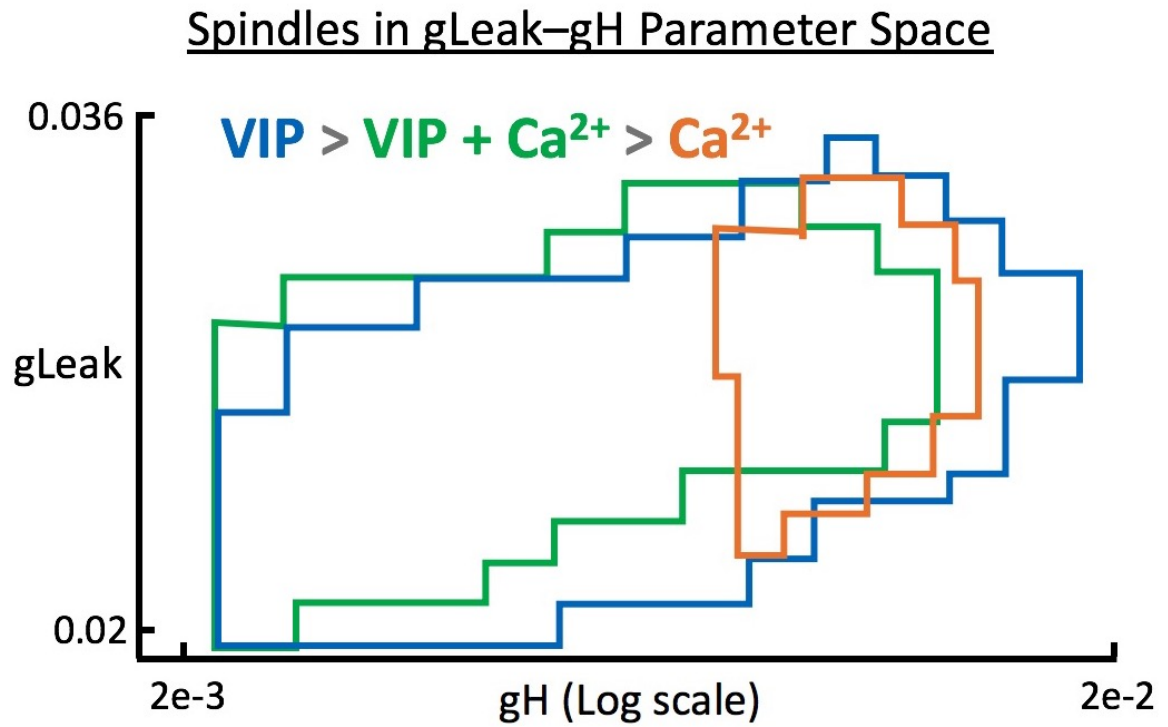
Figure 3·14: VIP HCN-modulation (blue) creates the most robust spindles in gLeak–gH parameter space. This is in comparison to calcium-mediated spindles (red) and the combination of both (green). The exact borders of each region are approximate based on the sparseness of simulations covering the parameter space. Spindles were identified via visual inspection of the simulation voltage traces.

they strongly impacted synchrony in the sparse randomly-connected model, discussed later in section 3.3.3. The addition of 0-mean Gaussian current noise was also tested, since it was expected to impair the traveling waves.

Thus, the presence of spindle waves was tested over a two-dimensional grid of different values for the synaptic strengths of TC → TRN gAMPA and TRN → TRN gGABA-A, both with and without noise (Figure 3·15A). Traveling waves were identified as those that moved smoothly around the circuit with a regular interval for at least a few cycles, as shown in Figure 3·15B and C. These clean traveling waves were identified throughout the parameter space, with some positions changing after the addition of low noise, but without a clear trend.

With greater noise, none of the simulations showed long-lasting spontaneous traveling waves with regular-intervals. A couple simulations did show the start of a regular-interval wave, but these would terminate after 1 cycle. A few simulations revealed noisy wave propagation, but these too did not last more than a cycle.

Notably, there was a sharp increase in spatial wave frequency with higher TRN → TRN gGABA-A values (Figure 3·15B1 vs. B2). In general, higher TRN → TRN gGABA-A was associated with fewer spikes per TRN burst and fewer TRN cells bursting in the model. This leads to less and shorter TC inhibition, so more TC cells can burst, and do so more rapidly after the hyperpolarization. This explains the faster wave propagation with higher TRN → TRN gGABA-A.

3.3.2 Medium Timescale VIP Leads to NREM3 → NREM2 Sleep Cycle Transition

Medium timescale VIP effects on the order of an hour biologically were determined using the isolated thalamic model with 20 cells of each population type (Figure 3·16). Following the time compression technique used here (see methods section 3.6.1), in simulation time the "hour" timescale was modeled using a 10 second timescale.
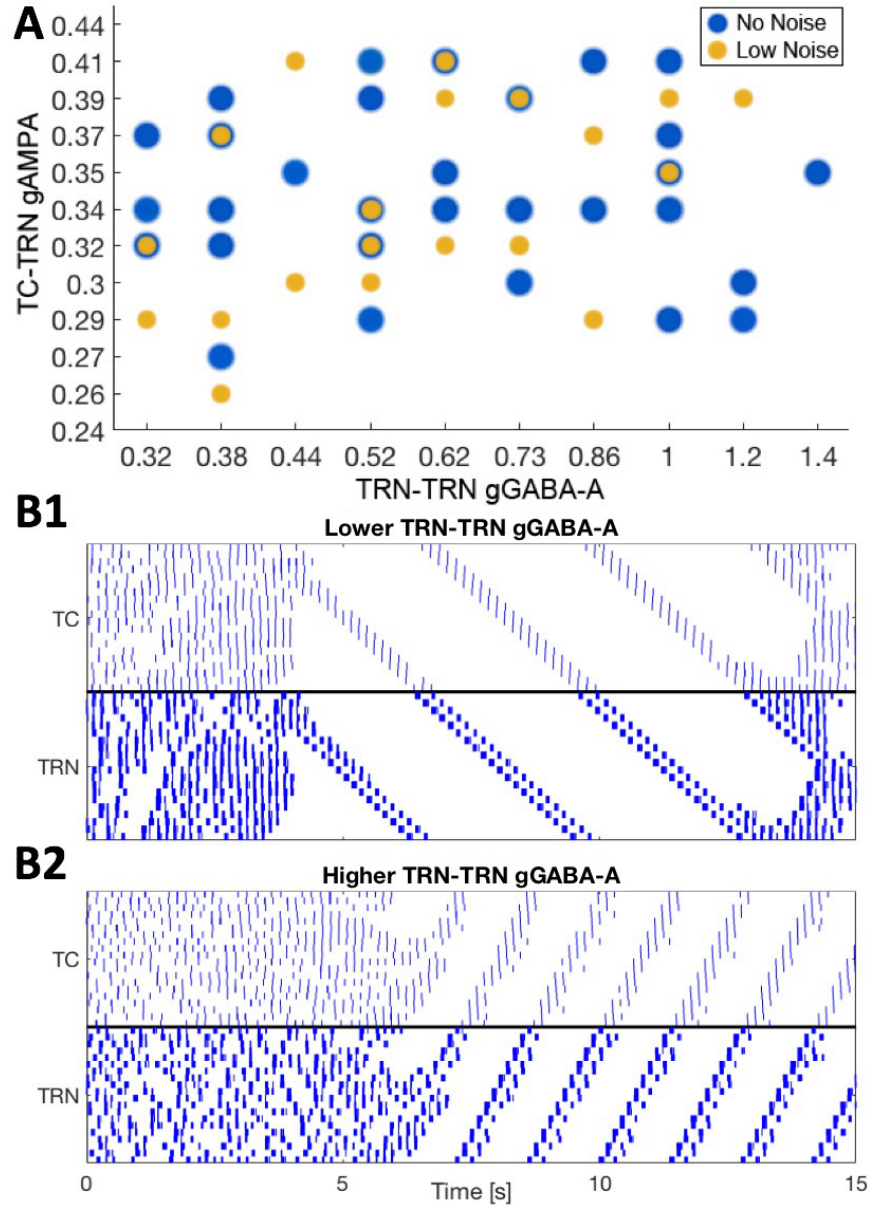
Figure 3·15: Spindle Waves Propagate in a Sparsely-Connected Thalamic Network. (A) Simulations of regular interval traveling waves are identified for different values of TC–TRN gAMPA and TRN–TRN gGABA-A. Blue dots are traveling waves without 0-mean current noise, while orange dots are traveling waves at low (0.5 standard deviation) 0-mean Gaussian-distributed noise. There is some overlap between the no and low noise conditions, but low noise mostly led to different simulations with traveling waves. Overall, low noise reduced the number of simulations with waves. Higher noise (1.5 standard deviations) prevented all regular-interval waves. (B) The wave propagation speed depended on the level of TRN–TRN gGABA-A. Simulations with TRN–TRN gGABA-A $\leq.13$ (B1) had much slower velocity than the waves from the gGABA-A range in panel A (B2). The rasters show a transition from continuous delta bursting to traveling spindle waves due to increasing gH from a slower VIP timescale, discussed in section 3.3.2.
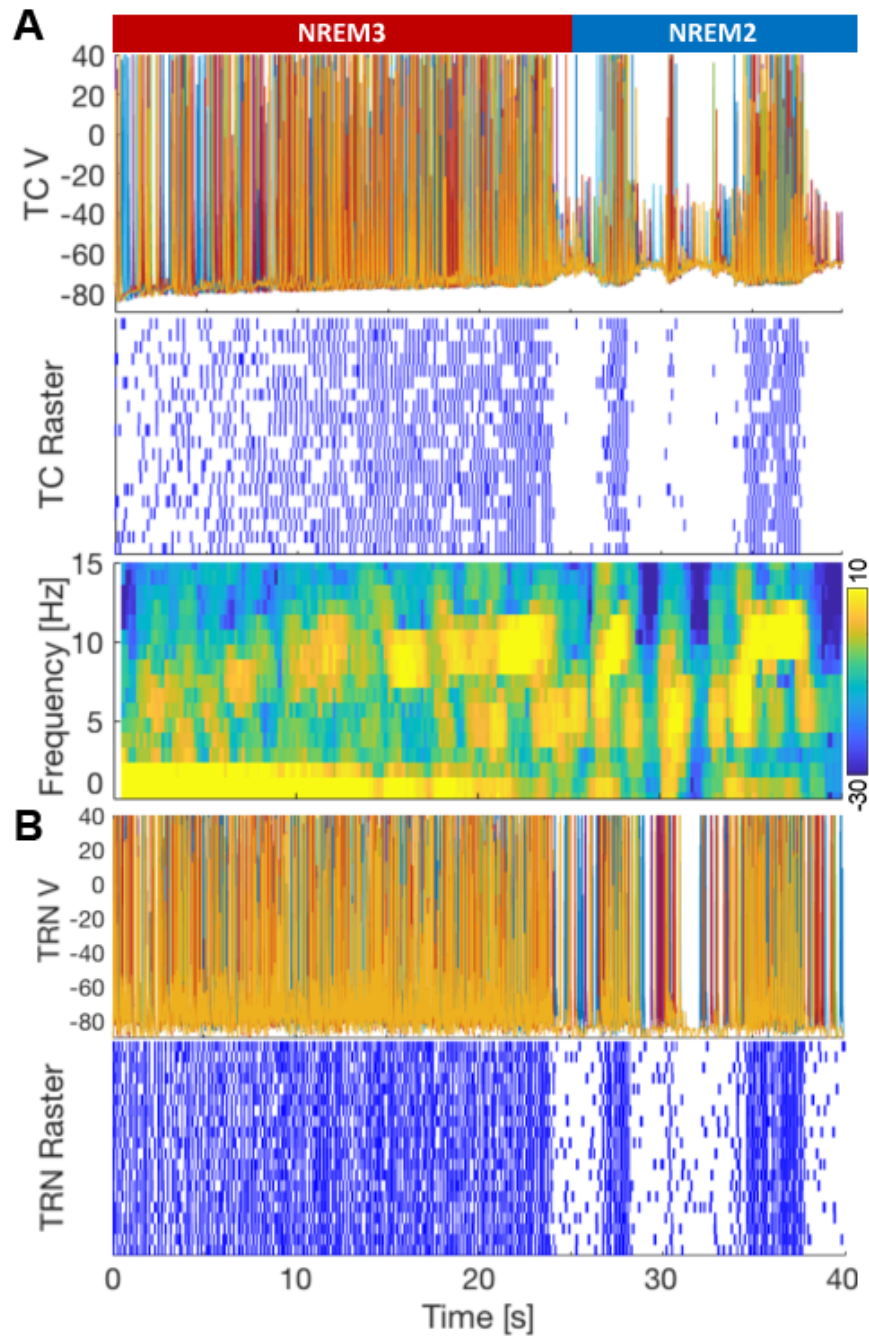
Figure 3·16: Single NREM3 → NREM2 transition in the 40 cell thalamic model. (A) TC cell activity. Top panel shows the voltage trace for the first 10 TC cells. Middle panel shows the spike rastergram for all 20 TC cells. Bottom panel shows the time-frequency spectrogram of the average TC population voltage trace. (B) TRN cell activity. Top panel shows the voltage trace for the first 10 TRN cells. Bottom panel shows the spike rastergram for all 20 TRN cells. Top NREM bar: the red portion shows the timespan of NREM3 continuous bursting, while the blue portion identifies the period of NREM2 spindling. The NREM3→NREM2 transition occurs around 25 seconds.

NREM3 Continuous Bursting

To model larger subpopulations of synchronized cells and facilitate visualization, medium timescale VIP effects were further investigated using a model with 2 cells of each type (i.e., each cell represents a synchronized cell population). As with the 40 cell model, the 4 cell model was initiated with parameters corresponding to the beginning of a deep non-rapid eye movement stage 3 (NREM3) sleep, during which time the whole model was bursting at a slow δ frequency ($\approx$1 Hz) in synchrony (Figure 3·17). As TRN fired bursts of spikes, VIP synaptic activity onto TC cells augmented the H-current. This corresponded to an increase in frequency for the entire circuit to a maximum of $\approx$6 Hz over 25 seconds of simulation time, corresponding to about an hour of biological time.

There is a switch to anti-phase TC activity midway through the NREM3 period, doubling the multi-unit activity (MUA) to an α ($\approx$9 Hz), while the single-unit activity (SUA) stays roughly the same (Figure 3·17). This is true for both the 4 and 20 cell models, although it is most easily seen in the 4 cell model voltage traces. In contrast, TRN stays synchronized throughout. This synchrony switch is discussed more in the synchrony section 3.3.3 below. Unlike with the isolated thalamus model, simulations including cortex maintained TC synchrony throughout the NREM3 period (Figure 3·21B) (see *Corticothalamic Synaptic Strength Modulates Global Synchrony* section). A synchronizing effect of cortex for thalamic oscillations has been reported previously (Destexhe et al., 1998), although at a broader scope in terms of spindle groups instead of the individual bursts considered here.

NREM2 Spindles

Eventually, the increasingly augmented H-current depolarizes the TC cells out of the NREM3 continuous bursting mode into the burst-tonic threshold region. At this time,
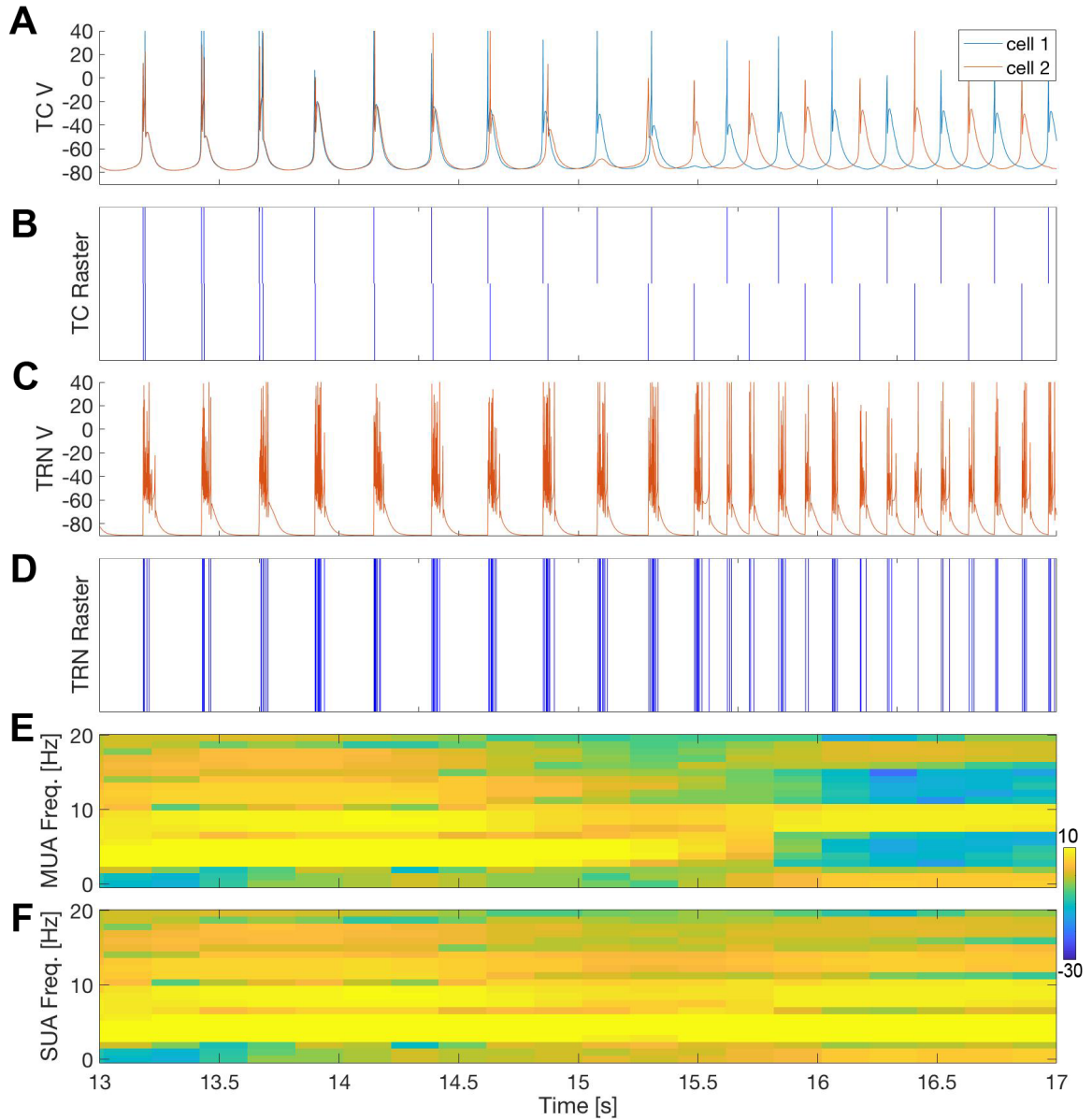
Figure 3·17: Population frequency doubles to anti-phase activity during NREM3 in absence of synchronizing cortical E↔E connections in 4 cell thalamic model. The switch occurs at 15 seconds. (A) TC cell voltage trace. (B) TC cell raster. (C) TRN voltage trace. (D) TRN raster. (E) Spectrogram for TC averaged population activity. (F) Average spectrogram for individual TC cells. Notice the increase in MUA spectrogram in E at around 16 seconds not reflected in the SUA power in F, indicating that the doubling of population frequency is due to a switch to anti-synchrony without a change in single-unit frequency.

the cells cease firing in the absence of external input sources.

To simulate *in vivo* conditions with inputs arriving from brainstem and other non-modeled regions, random Poisson synaptic noise was added to TC cells. Due to the lack of an informed noise model, Poisson noise was used since it is the most agnostic for discrete events.

With this noise added, the silent period is brief since the synaptic noise triggers bursts in a TC cell, which recruits the entire network to engage in a short spindle of a few seconds (Figure 3·19B). As with previous modeling results (Destexhe et al., 1996), the population bursting activity is anti-phase at α frequency, consistent with the empirical observation that TC cells typically fire every 2–3 TRN bursts in ferret lateral geniculate nucleus (LGN) slices (Figure 3·18)(Bal et al., 1995). Furthermore, the interspindle interval is random due to spindles being triggered by Poisson noise. In the absence of noise to the TC cells, VIP acting on the hour timescale maintains the cells in a silent region between excitation-driven spontaneous tonic spiking and burst mode (Figure 3·19A). If the noise is delivered to the TRN neurons instead of TC cells, the TRN cells synchronize the TC cells and cause brief episodes of δ frequency bursts (not shown) (see the synchrony results section 3.3.3 next and the discussion section 3.4.2 for more explanation of this difference).

Unlike the all-to-all connected thalamic model which starts NREM3 with TC synchrony, the sparse 20% nearest-neighbor connected model starts NREM3 with TC anti-synchronous thalamic bursting in the absence of cortex (same finding as in Figure 3·21A for low E→TC gAMPA corticothalamic connectivity). Despite the TC synchrony difference, the population frequency starts in the δ range for both. Previous modeling work only reported the NREM3 continuous bursting condition with a 4 cell all-to-all network, not a sparse network (Destexhe et al., 1996).
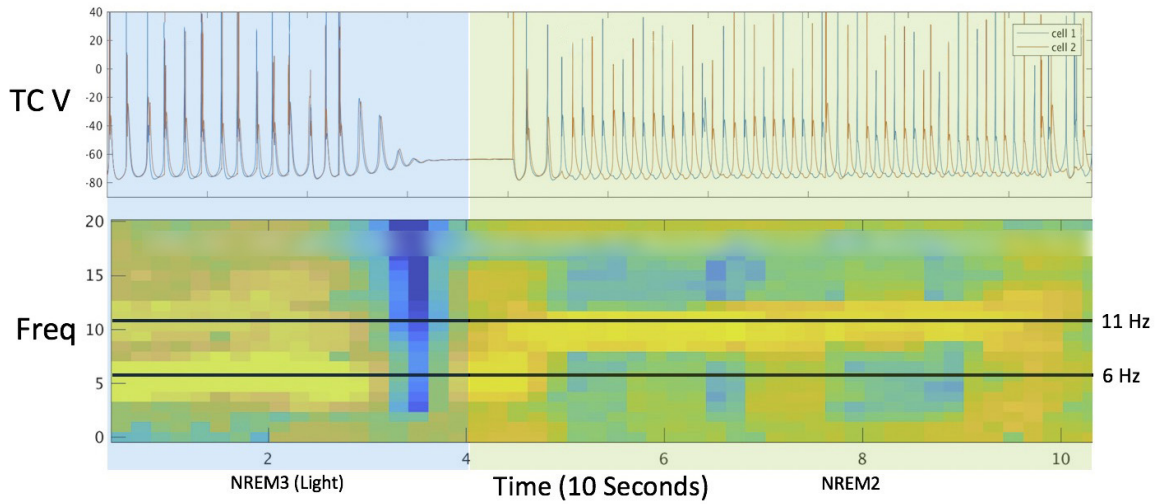
Figure 3·18: Transition from synchronized NREM3 delta bursting (blue background) to anti-phase NREM2 alpha spindling (green background). Top panel is the voltage trace for the 2 TC neurons, while the bottom panel is the multi-unit spectrogram. Notice the shift from 6 Hz bursting to 11 Hz alpha. Note: this particular simulation featured a longer initial spindle that continues past the right edge of the figure before terminating.

Mixed Local and Global NREM2 Spindles

Changing the 40 cell thalamic model's synaptic connectivity from all-to-all to a sparser 20% nearest-neighbor topology leads to traveling spindle waves. As seen in previous experimental (Kim et al., 1995) and modeling (Destexhe et al., 1998) studies, some waves stay local to the region of input, while most propagate globally to all TC cells (Figure 3·20), as well as to all E cells (Figure 3·21A). While Poisson inputs to 1 TC cell or 2 TRN cells yielded global spindles, inputs to only 1 TRN cell did not. This imbalance is likely because a single TC cell can recruit multiple TRN cells. The occurrence of both mixed local and global spindles provides validation of this new model. These local spindles support the notion of thalamic involvement in local cortical sleep (described in the *Introduction*).
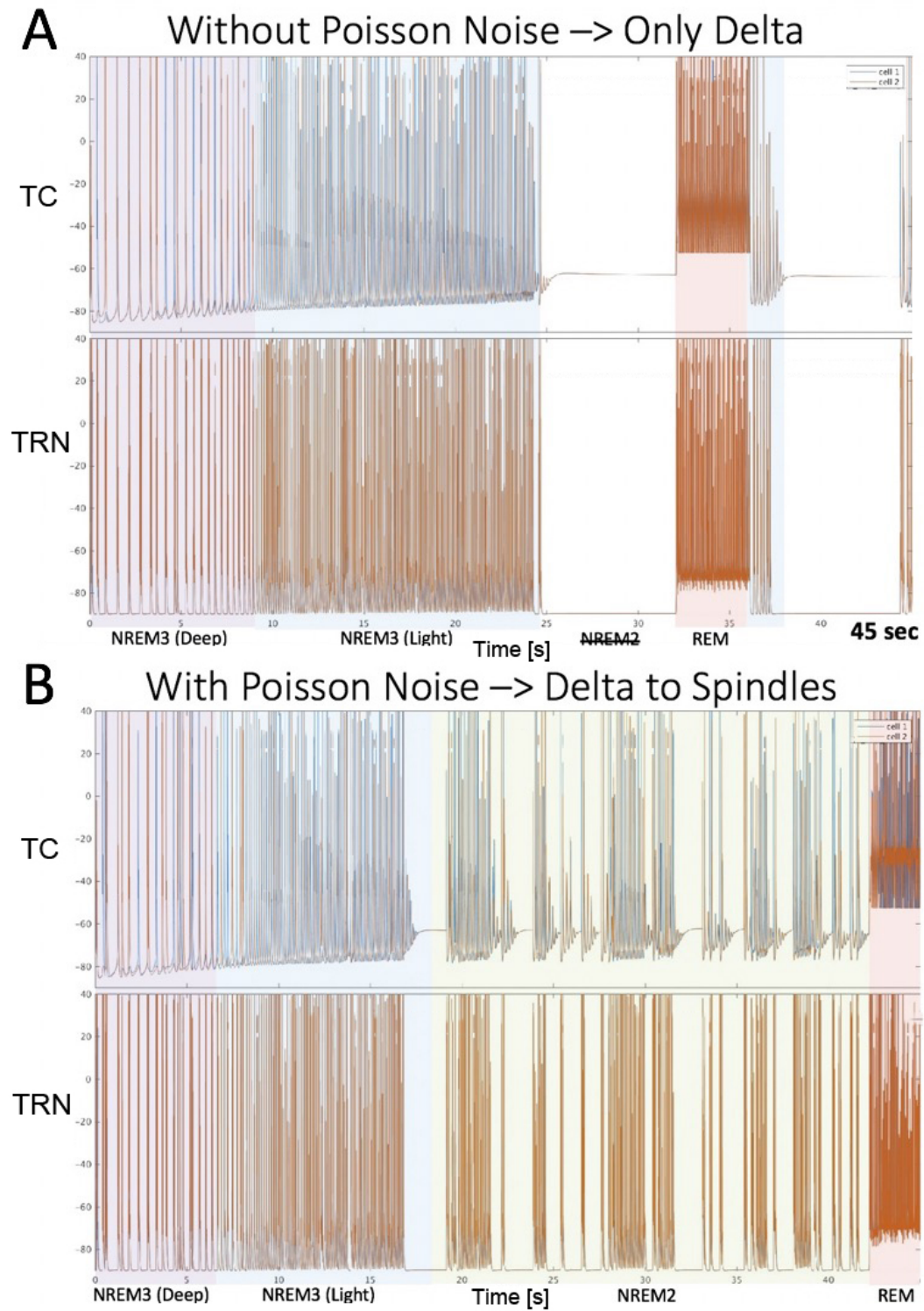
Figure 3·19: Poisson noise to TC cells triggers spindles. (A) Without poisson noise, there are no NREM2 spindles, just depolarized silence. (B) With noise, the NREM2 period has alpha spindles (green region).
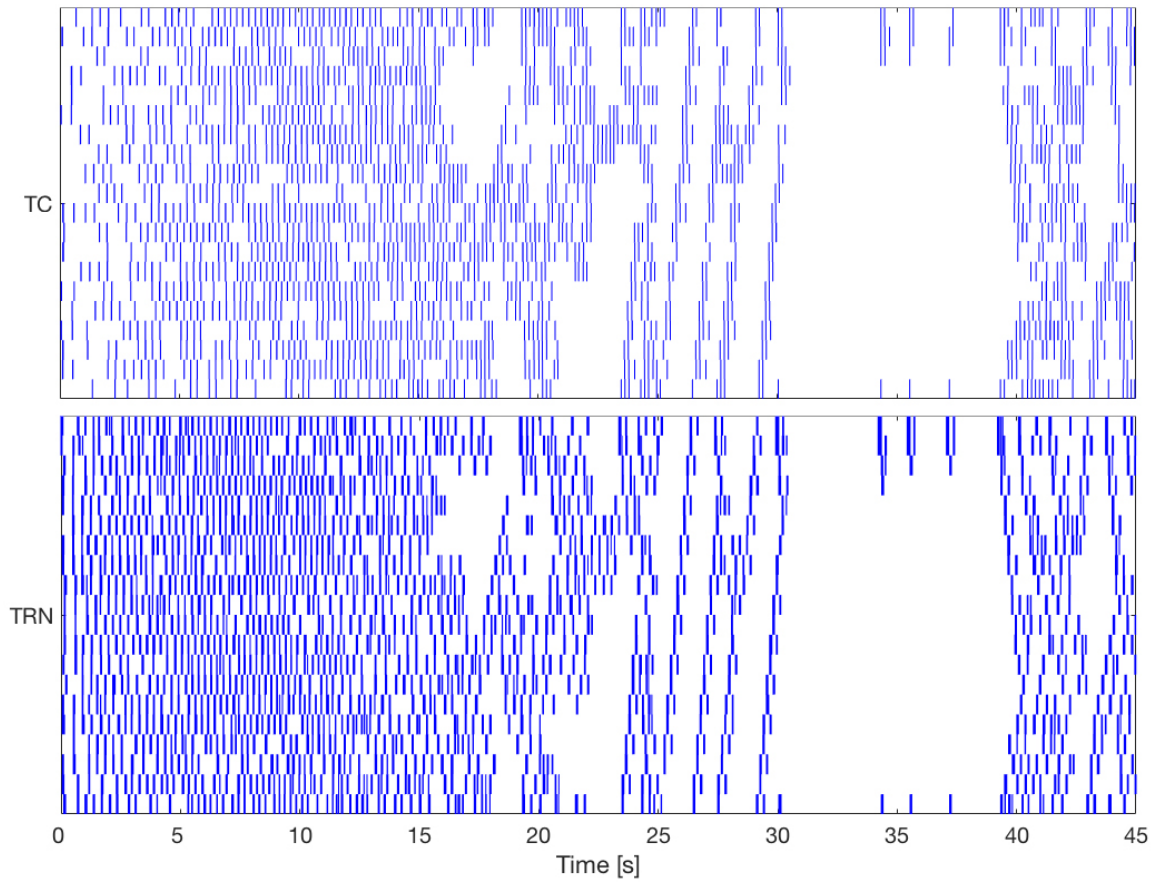
Figure 3·20: Mixed local and global NREM2 spindles in a sparsely connected 40 cell thalamic model. Global traveling spindles are found between 25 and 30 seconds. Three local spindles occurred around 35 seconds.

Corticothalamic Synaptic Strength Modulates Global Synchrony

Previous modeling studies have demonstrated a synchronizing role of cortex for spindle groups in different thalamic cells (Destexhe et al., 1998). To explore thalamic interactions with cortex in a sparse setting, a 40 cell cortical model with the same sparseness was added to the 40 cell thalamic model of the previous section to yield an 80 cell sparse 20% nearest-neighbor-connected corticothalamic model.

I hypothesized that the addition of cortex would synchronize individual bursts across cells. Indeed, the strength of the synapse from cortex E cells to thalamic cells controlled the degree of synchrony across all populations, as depicted in Figure 3·21. Lower E→TC gAMPA led to sparse anti-synchronous firing within each population at NREM3 (i.e., the lower VIP/gH levels) found at the start of the simulations. Higher E→TC gAMPA recruited and synchronized all the thalamic cells, and most of the cortical cells. E→TRN gAMPA had similar effects. This synchrony with higher synaptic values was present for both NREM3 and NREM2 spindles.

Since there are no TC↔TC synapses in thalamus, these excitatory neurons are predisposed to anti-synchrony. The synchrony from including cortex is due to the cortical E↔E connections, which effectively adds an excitatory connection between TC cells.

Synchronous spindle bursts are characteristic of interlaminar thalamic nuclei (Destexhe and Sejnowski, 2001). Thus, the higher E→TC gAMPA values are desirable for modeling the arousal-related thalamic regions of interest here.

Finally, while traveling spindle waves occurred for most E→TC gAMPA values tested, extremely large values led to synchrony of all cells, even during spindles (not shown).
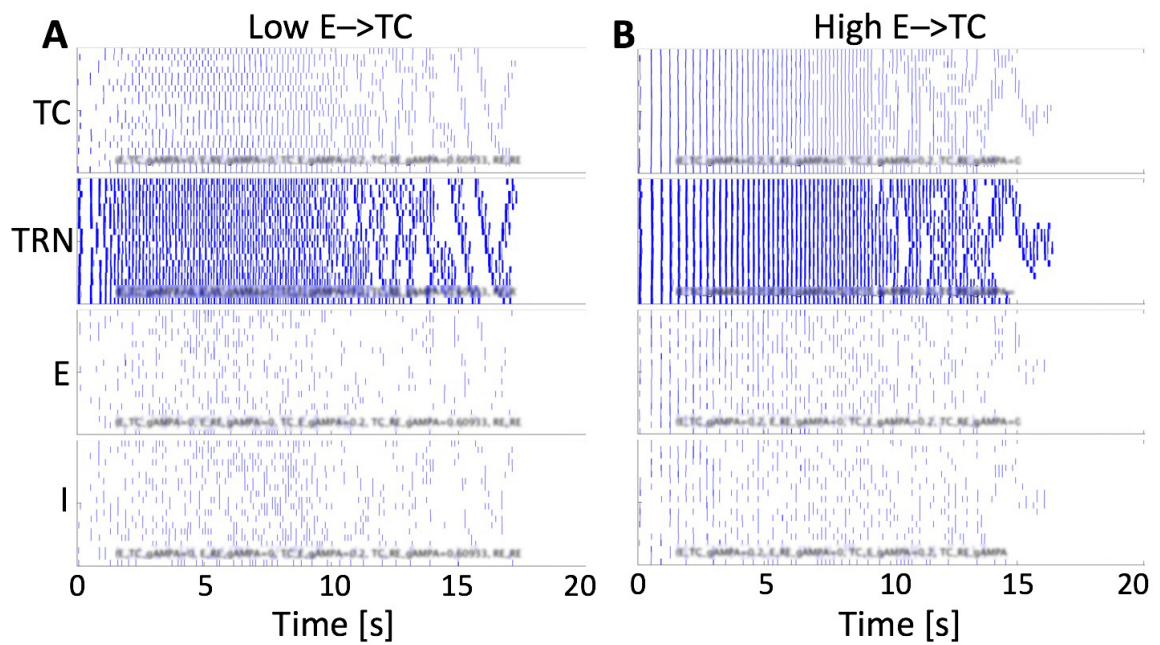
Figure 3·21: Corticothalamic synaptic strength modulates global synchrony in a sparsely connected 80 cell corticothalamic model. Each cell with synapses connected to it's 5 nearest neighbors (20% connectivity per cell). (A) Low E→TC gAMPA = 0.002. TC cells remain anti-synchronous during NREM3 continuous bursting before switching to synchronous NREM2 traveling spindle waves. (B) Higher E→TC gAMPA = 0.02 recruited and synchronized all the thalamic cells, and most of the cortical cells, even during NREM3 at the beginning of the simulation.

3.3.3   Synchrony Changes During H-Current Modulation

Surprisingly, many parameter combinations yielded changes in synchrony within TC and TRN populations during H-current augmentation from medium-timescale VIP effects. Since these synchrony changes have not been explored extensively in the literature, the mechanisms of synchrony change were analyzed using phase response curve theory and simulations over multiple parameters.

Examining Synchrony using Phase Response Curves

The switch from synchrony to anti-synchrony in the isolated thalamic model was investigated further using phase response curves (PRCs). The PRC is a useful tool to assess synchrony mechanisms, and consists of determining the change in the interspike or interburst interval after inputs are delivered at various phases within the interval (Borgers, 2017).

Instantaneous impulse input PRCs for TC cells lacking noise were calculated for different levels of gH, representing the increasing VIP effect over time. At higher gH levels corresponding to relay mode, TC cells have a type 1 PRC (all positive or negative valued) for both positive and negative inputs, which indicates a predisposition toward synchrony (Figure 3·22)(Borgers, 2017).

Unlike relay mode, TC cells at lower gH levels corresponding to burst mode have a type 2 (positive and negative valued) PRC (Borgers, 2017), which was similar across bursting gH levels (only the magnitude of peaks changed slightly). For excitatory impulses, the positive slope when crossing the 0 phase shift (y-axis) at middle phases (x-axis) suggests stable synchrony (Figure 3·23B), whereas the negative slope when crossing 0 phase shift for inhibitory impulses suggests stable anti-synchrony (Figure 3·23A)(Borgers, 2017). Based on these results, one would expect short time constant AMPA synapses from cortex to act to synchronize TC cells, while rapid GABA-A
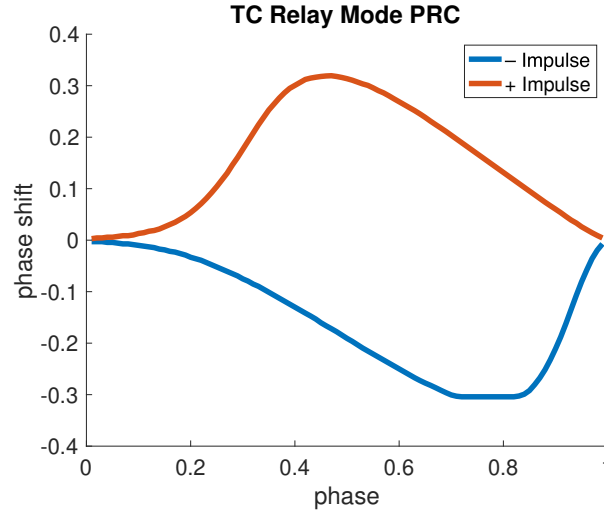
Figure 3·22: TC cells in relay mode have a type 1 (all positive or negative valued) phase response curve (PRC) for instantaneous inputs suggesting stable synchrony. Positive inputs are in red while negative impulses are in blue.

synapses from TRN are expected to encourage anti-synchrony. The slope magnitude can also affect stability interpretations but was not further examined here.

PRCs for TC cells in burst mode at different gH levels were also calculated for non-instantaneous inhibitory inputs with decay times ranging from 5 ms (GABA-A) to 500 ms (GABA-B). These PRCs reveal a switch from type 2 stable anti-synchrony for GABA-A to type 1 stable synchrony for GABA-B (Figure 3·24). Curves were similar across the tested gH ranges.

Exploring Synchrony via Simulation of a Parameter Volume

Synchrony was also examined through simulations of the 4 cell thalamic model without VIP. When initial TC cell voltages lay within ≈8 mV of one another, they tended to synchronize; when TC cells started >≈8 mV from one another, they moved into an anti-synchronous rhythm (Figure 3·25). Thus, empirically there is a small window of stable synchrony, likely due to the interaction between synchronizing GABA-B and anti-synchronizing GABA-A.

Indeed, simulations of the same 4 cell thalamic model with different levels of noise,
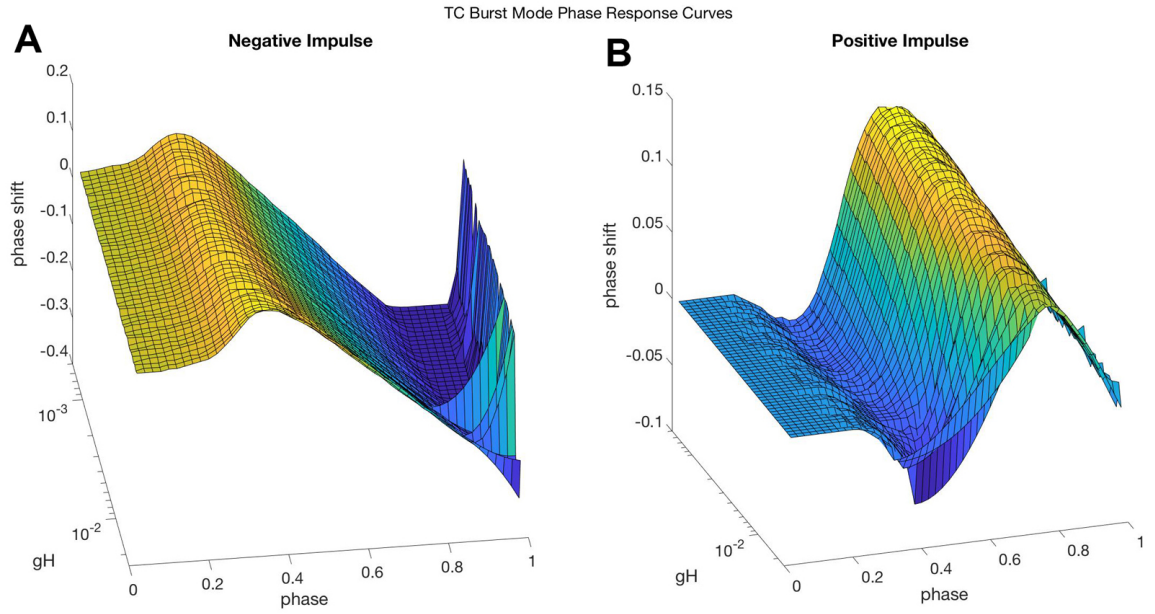
Figure 3·23: TC burst mode phase response curve (PRC) for instantaneous inputs at different H-Current conductances. (A) Type 2 PRC (positive and negative valued) for inhibition indicating stable anti-synchrony. (B) Type 2 PRC for excitation suggesting stable synchrony.
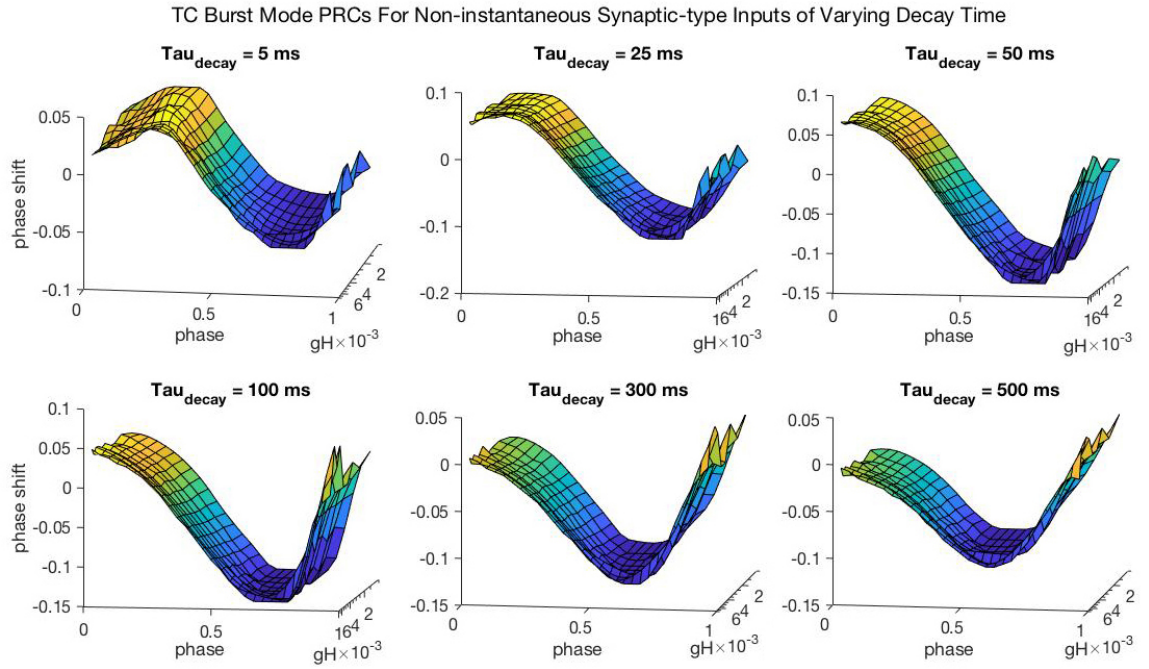
Figure 3·24: TC burst mode phase response curves for synaptic inhibition with decay time constants ranging from 5 ms (GABA-A) to 500 ms (GABA-B) reveal switch from type 2 to type 1.
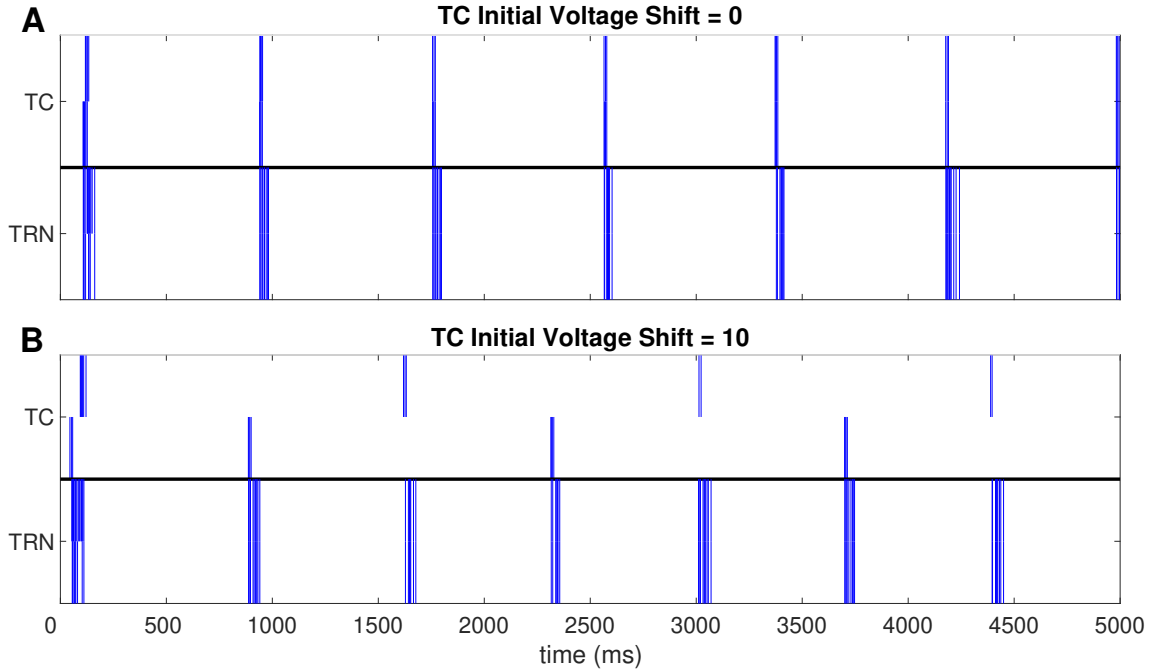
Figure 3·25: Rastergram reveals that TC cell synchrony in 4 cell model depends initial TC voltage spread. (A) TC cells synchronize when initial voltages are equivalent; (B) TC cells become anti-synchronous when initial voltages differ by 10 mV.

synaptic conductance, and starting voltage shifts reveal that both synchrony and anti-synchrony can be stable. Increasing TC→TRN gAMPA, TRN→TRN gGABA-A, and gH tended to promote anti-synchrony (Figure 3·26). Higher TRN→TRN gGABA-A led to fewer spikes per burst, and hence less cooperative GABA-B release, shifting the balance toward anti-synchronous GABA-A. Increasing TRN→TC GABA-A could cause a tendency toward either synchrony or anti-synchrony, depending on the values of the other parameters.

To summarize, TC cells in burst mode have a tendency toward anti-synchrony from TRN GABA-A, and synchrony from TRN GABA-B and cortical AMPA. The relative strength of each of these controls the type of synchrony. Including VIP effects in the isolated thalamic model starting from anti-synchrony reveals a continuous increase in frequency from δ to α, as expected. While it did not appear to affect the results, it has been demonstrated that noise can lead to bifurcations that change the synchrony
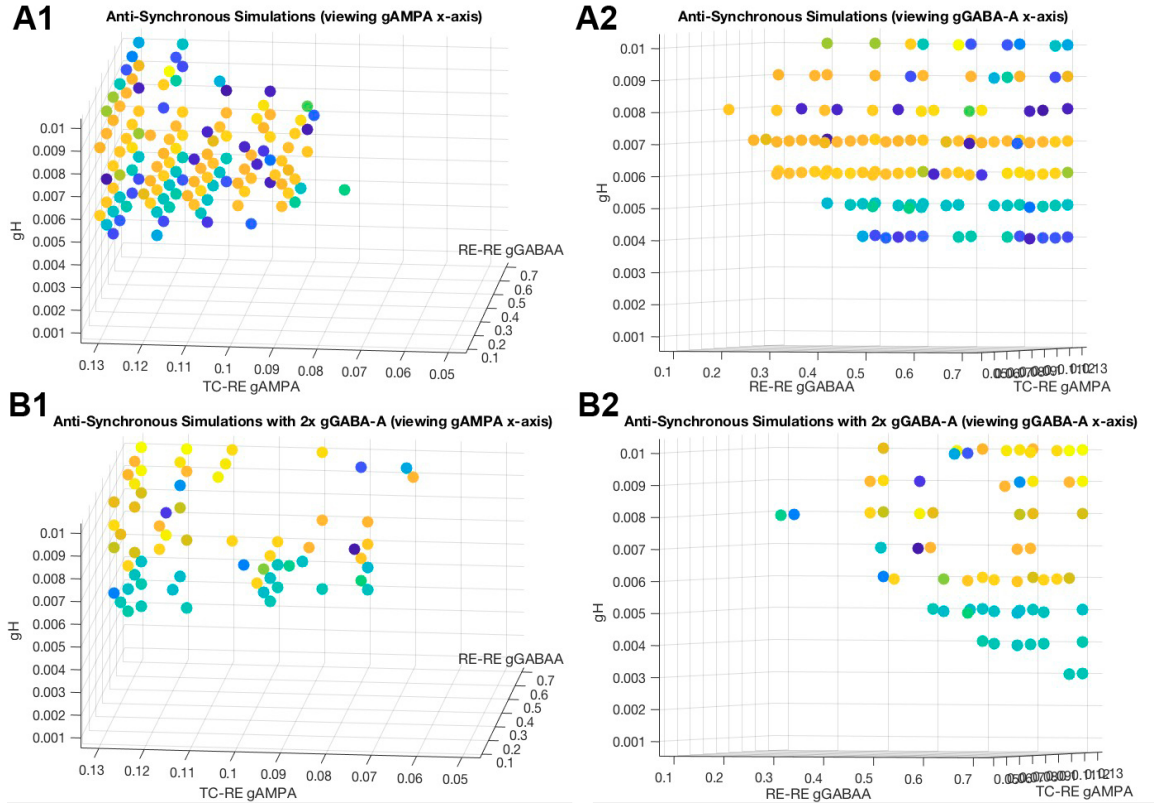
Figure 3·26: Anti-synchronous solutions for 4 cell thalamic model in gH and 3 synaptic conductance parameter space. (A) is baseline TRN→TC gGABA-A while (B) is 2x gGABA-A. (1) is a view with TC→TRN gAMPA in the x-axis position, while (2) is an alternative view with gGABA-A in the x-axis position. Anti-synchronous solutions cluster at higher values for all 3 axes. Note the general reduction in anti-synchronous points for 2x gGABA-A (i.e., B panels).

conclusions that are based on the PRC (Ermentrout and Saunders, 2006).

These results suggest that the switch from synchrony to anti-synchrony discussed in the *NREM3* section above results in part from an increase in the effective GABA-A strength as the TC cells depolarize away from the GABA-A reversal potential with increasing VIP effect. In addition, given a fixed time lag for TRN firing after TC firing and the shortening of the interburst interval with increasing depolarization, the GABA-A inhibitory post-synaptic potentials (IPSPs) will arrive at later phases closer to the maxima for phase advancement, which is maximally destabilizing of the synchrony condition.

3.3.4 Long Timescale VIP Shapes Sleep Stage Architecture

To determine the effect of long timescale ($\approx$8 hour) VIP effects on sleep stages using the uncompressed biological hours timescale in model time (versus a compressed seconds model timescale; see section 3.6.1), a simplified non-spiking thalamic model based on the spiking thalamic model was implemented first (described in section 3.6.7). As can be seen in Figure 3·27, the TC cells in successive NREM phases become progressively more depolarized. From the spiking model findings in section 3.3.2, this corresponds to a shift toward higher NREM3 bursting frequencies and greater time spent in NREM2 spindling (Figure 3·18). The trend of decreasing NREM3 : NREM2 was the desired feature that matches human hypnogram data (Scammell et al., 2017).

Next, all 3 timescales of VIP effects were added to the compressed-timescale spiking thalamocortical model to examine VIP's effects on sleep stage architecture during a simulated full night's sleep (described in section 3.6.3). The full night's sleep was comprised of five $\approx$20 second-long NREM-REM sleep cycles, corresponding to five biological 90 minute sleep cycles (i.e., 7.5 hours sleep). The newly added third timescale is the hours biological timescale corresponding to a 1 minute time constant in the model.
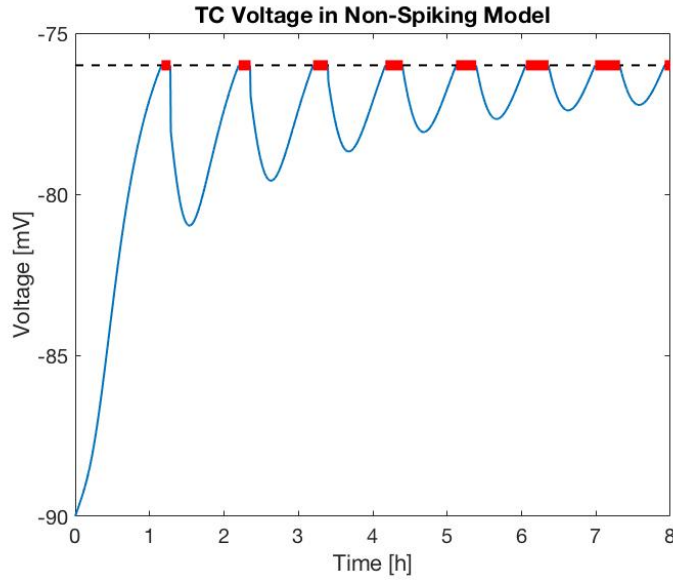
Figure 3·27: Human sleep architecture in a simplified non-spiking thalamic model with long timescale VIP effects leads to decreasing NREM sleep depth between REM cycles. This model demonstrates the timescales in the uncompressed true timescale, unlike the compressed timespan spiking model. Red horizontal bars indicate REM periods.

Figure 3·28 depicts the sleep data for TC cells in the 8 cell thalamocortical model, and reveals how each of the three cAMP timescales contributes to a feature in the voltage trace (Figure 3·28A). The seconds cAMP biological timescale shown in Figure 3·28B leads to the NREM2 spindles. Figure 3·28C reports how cAMP acting on the minutes biological timescale leads to NREM3→NREM2 transitions. Finally, Figure 3·28D demonstrates how the steady rise of the slowest cAMP state variable (hours biological timescale) creates the trend of decreasing ratio of NREM3 : NREM2 throughout the night, as found also in the simplified model (Figure 3·27). Within TC cells, this trend results from steadily increasing the minimum membrane potential, predisposing TC cells to depolarized NREM2 spindling over the hyperpolarized NREM3 bursting.

Statistics from 100 replications of the 80 cell full night's sleep thalamocortical model are shown in Figure 3·29. What differed between replications were the stochastic elements of the model, specifically the current noise and Poisson TC synaptic
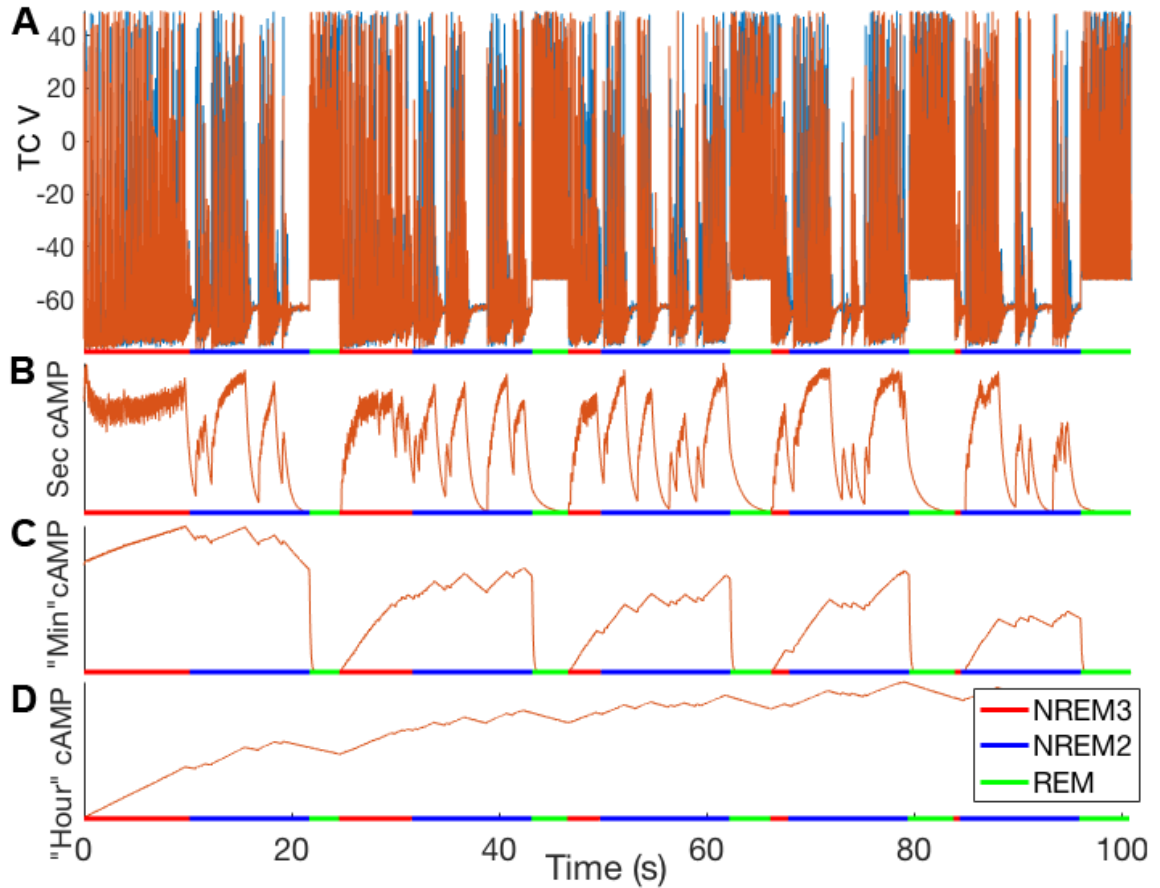
Figure 3·28: Progressive shift to greater NREM2 : NREM3 over course of full night of sleep in spiking model. (A) Voltage trace for 2 TC cells. The bottom portion of the panel reveals the sleep stages, including NREM3 (red), NREM2 (blue), and REM (green). (B) Seconds timescale cAMP. (C) Minutes biological timescale = 10 seconds model timescale cAMP. (D) Hours biological timescale = 1 min model timescale cAMP.

input that triggered spindles and affected REM3 lengths. Figure 3·29A shows the proportion of time spent in each sleep stage compared to rough empirical values—the proportion of model time spent in each sleep stage of 19%, 59%, and 22% approximates empirical values (Scammell et al., 2017) of 25%, 50%, and 25% of time spent in NREM3, NREM2, and REM, respectively.

Figure 3·29B-D shows the model TC population spectral power for each sleep stage averaged over the 100 replicates. The spectrum of figure 3·29B shows the 6 Hz δ frequency peak for NREM3. Figure 3·29C demonstrates how NREM2 lacks a δ power peak below 5 Hz, and has power at both δ and α bands. The NREM2 δ power is due to these simulations often being synchronized during spindles, leading to a lower frequency, as discussed in 3.3.3 section. The REM β peak at 15 Hz in Figure 3·29D results from the cortex having a beta frequency preference when driven strongly, as in REM conditions.

3.3.5 Propofol Counteracts VIP's Mechanisms

Since propofol anesthesia is believed to harness the innate sleep pathway in addition to directly inhibiting the H-current responsible for VIP's effects, the interaction between propofol and the VIP mechanisms above was examined using the isolated thalamic model.

Propofol's three dominant actions on thalamus, pictured in Figure 3·30A, were examined separately: (1) augmented TRN GABA-A conductance and decay time constant (2x baseline) in Figure 3·30B; (2) decreased H-current conductance (20% baseline) in Figure 3·30D; (3) indirectly increased potassium leak conductance (1.5x baseline) via the brainstem neuromodulators histamine and acetylcholine in Figure 3·30C. The three cAMP timescales were all sped up to ensure that cAMP equilibrated faster, permitting 30 second simulations (versus keeping the timescales slower and having to simulate longer with the same end result).
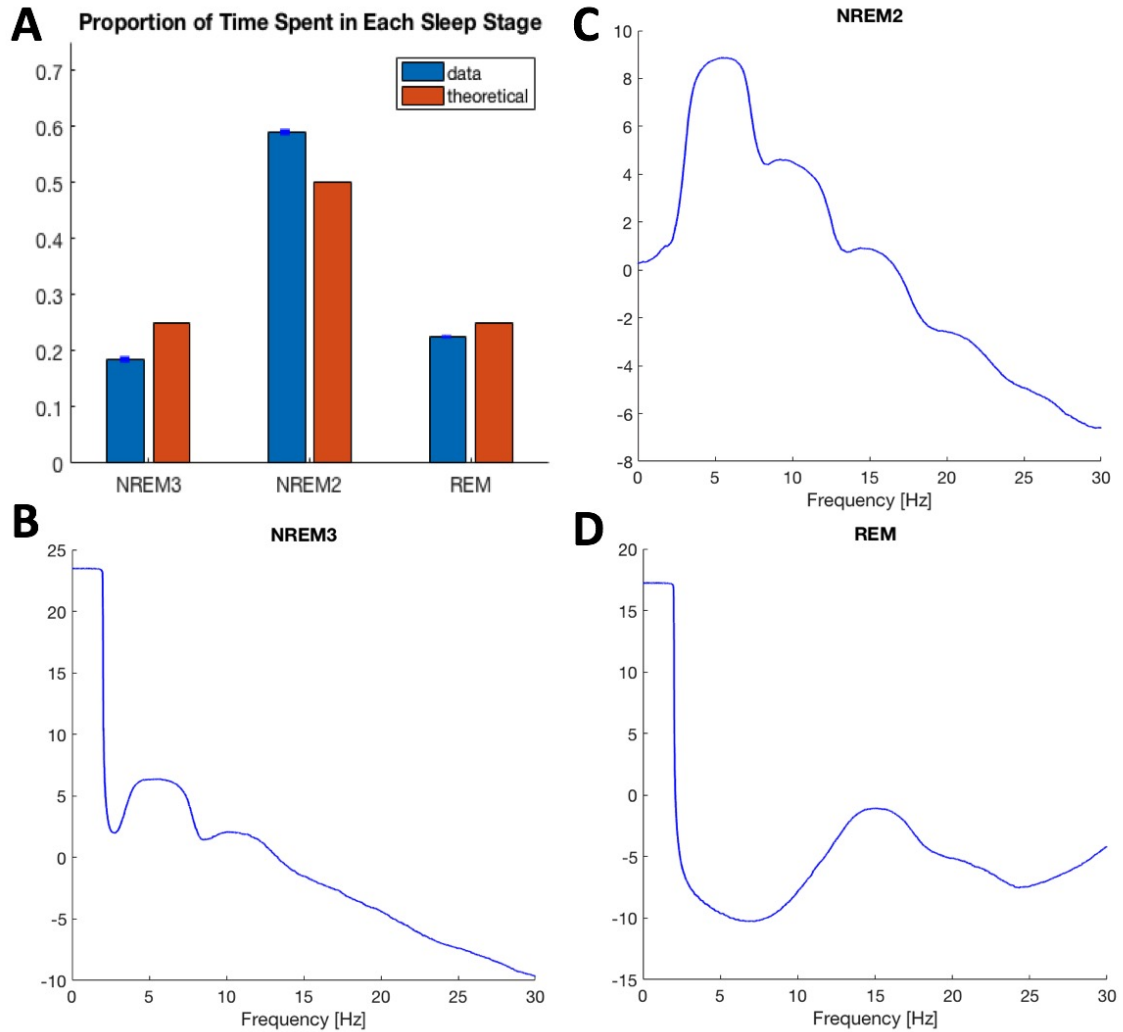
Figure 3·29: Statistics of thalamocortical model sleep stage architecture are similar to empirical human values. A full night's sleep of 5 NREM-REM cycles is simulated 100 times in the 80 cell thalamocortical model with different instantiations of current and TC synaptic noise. (A) Proportion of time spent in each sleep stage of 19%, 59%, and 22% compared to empirical values of 25%, 50%, and 25% for NREM3, NREM2, and REM, respectively. Error bars show 2 standard errors of the mean. (B) Mean average spectrum of TC cells for NREM3, NREM2, and REM, respectively. Shaded error region represents 2 standard errors of the mean.

All three propofol effects decreased excitation within thalamus sufficiently to prevent VIP's effects from switching thalamus from NREM3 continuous bursting to NREM2 spindling, keeping the TC cells bursting in a slow/delta bursting regime. Simulations also revealed that increasing any of the three propofol effects led to decreasing burst frequency, which is expected from the greater inhibition and hyperpolarization.
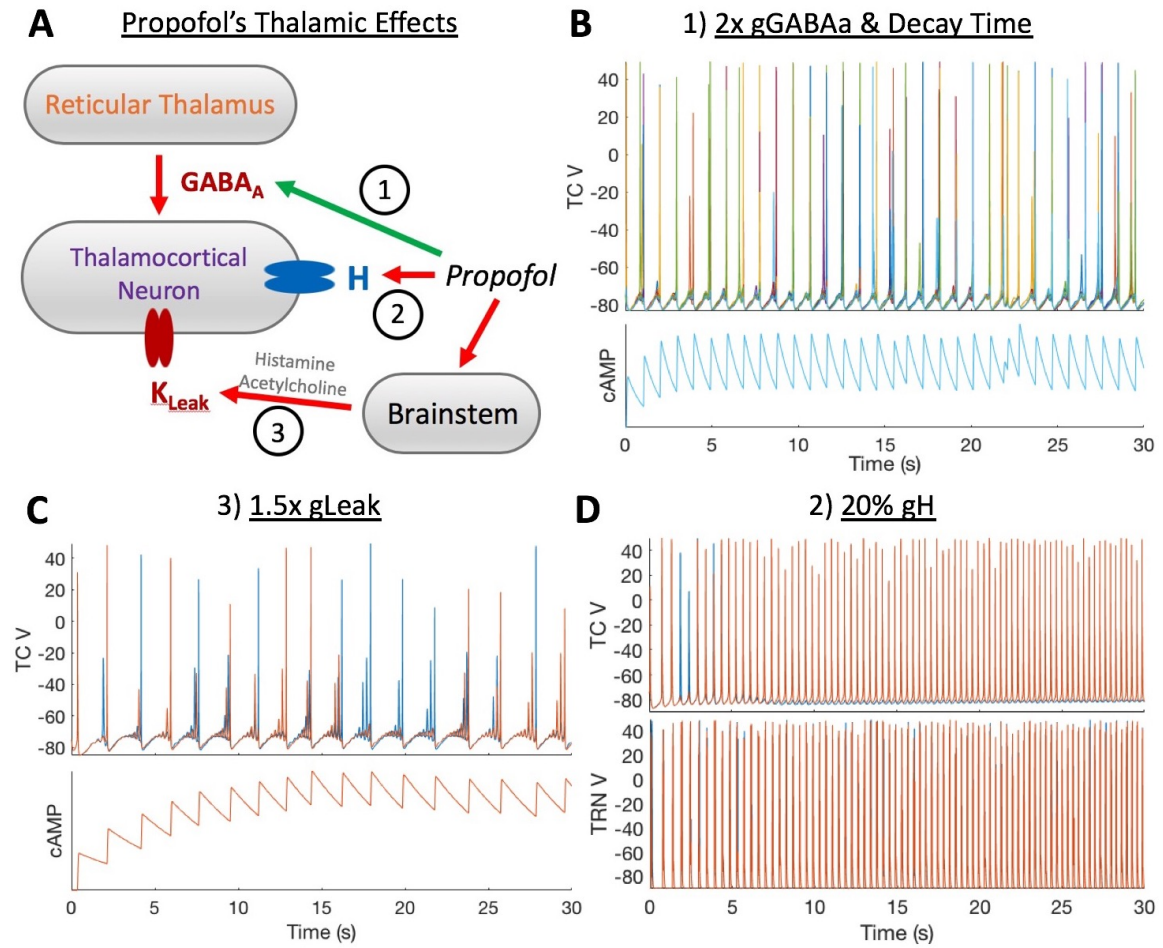
Figure 3·30: Propofol counteracts VIP mechanisms in 30 second simulations of the thalamic model. (A) Propofol has 3 effects on thalamus: (1) augmentation of GABA-A conductance and its decay time constant (2x baseline); (2) increased gH (20% baseline); (3) indirect increase of potassium leak (1.5x baseline) via brainstem neuromodulators histamine and acetylcholine. (B-D) modeling each of the three propofol effects on thalamus maintained continuous bursting at delta frequencies and prevented transition to relay mode or spindle patterns. Importantly, these effects persisted once VIP-mediated cAMP second messenger activity reached equilibrium (bottom panels of B-C).

3.4 Discussion

The present work investigated the significance of intrathalamic vasoactive intestinal peptide (VIP) neuromodulation in a computational model. This model was extended from previous models (Destexhe et al., 1996; Destexhe et al., 1998) to include VIP neuromodulation at multiple timescales, each of which yielded different results. Shorter timescales led to more robust spindles compared to past models. Longer timescales shaped NREM3 to NREM2 transitions and the trend of decreasing ratio of NREM3 : NREM2 through a night's sleep. The simulated effects of propofol counteracted these VIP mechanisms, keeping thalamus in a slowly bursting state characteristic of anesthesia. Thus, the main results are that (1) intrathalamic VIP controls sleep stage architecture, and (2) neutralization of intrathalamic VIP's excitatory effects contributes to the inhibition by propofol anesthesia.

3.4.1 Spindles from Short Timescale VIP Effects

As shown in Figure 3·14, simulations of short timescale VIP in the isolated thalamic model revealed a novel mechanism for spindle production. These spindles were more robust than those from previous models, meaning they could be elicited over a larger region of the relevant parameter space, i.e. maximal gH and gLeak. Interestingly, the range of spindles increased even more when the VIP mechanism was isolated by removing the calcium one. Furthermore, modifying the calcium modulation from the starting value only decreased the robustness of spindles. In contrast to the current view, these results suggest that fast-timescale neuromodulation from TRN may be the primary mechanism of spindle termination in TC cells. If true, inhibiting VIP's actions should reduce or fully prevent spindles.

The H-current augmentation mechanism responsible for spindles is similar for VIP- and calcium-mediated spindles (Figures 3·10, 3·14B). However, calcium entry

is related to T-current activation during TC bursting while VIP-activity results from TRN bursting. Incidentally, TRN bursts tend to have tens of spikes while TC bursts have only a few spikes. A TRN source of spindle bursting is more consistent with the literature result that spindle length correlates more strongly with TRN than TC activity (Bartho et al., 2014).

Minimal Biophysical Spindle Mechanism

Biophysically, any source that depolarizes the cell during a period of bursting can terminate the bursts, since the essential T-current would be inactivated by depolarization. T-current inactivation removes its depolarized plateau on which bursts occur. If the depolarization mechanism were to terminate bursts only after a few seconds of bursting and then last at least a few seconds after termination, that could shape spindle formation. This is in contrast to short depolarizations less than a second that would cause brief segments of burst skipping, very unlike spindles.

Spindle Mechanisms In The Literature

Both experimental and computational studies have examined the mechanisms of spindles for decades. The consensus is that TRN is fundamental to spindle generation. Early studies demonstrated that the isolated TRN can produce recurring segments of α oscillations (Steriade et al., 1987), and that spindles are abolished once TC cells are disconnected from TRN (Steriade et al., 1985).

From the mathematical literature (Kopell and Ermentrout, 1986; Izhikevich, 2007; Ermentrout and Terman, 2010), the switch from continuous bursting to spindles requires a mechanism to terminate the bursts and force a temporary period of silence before bursting reinitiates. Once the thalamus is sufficiently hyperpolarized, the H/T-current pacemaker serves as the initiator of bursting (section 3.2.6). That spindle termination results from H-current augmentation was verified by reducing H-current

and demonstrating conversion of spindles to continuous bursting (Luthi et al., 1998), as predicted by computational models (Destexhe et al., 1996). However, these models made the simplification of modulating H-current by calcium, as discussed in section 3.2.7. The ultimate mediator of H-current augmentation was not determined.

More recently, optogenetic stimulation of mouse TRN was shown to generate cortical spindles (Halassa et al., 2011). Cortex can also initiate spindles, but this is likely though cortical stimulation of TRN (Bonjean et al., 2011). A rat study recording TC and TRN cells during spontaneous spindles concluded that spindle length was more correlated with TRN than TC activity; although in a separate experiment, the magnitude of TRN optogenetic activation did not correlate with spindle length, suggesting a more complicated relationship between spindles and each thalamic cell type (Bartho et al., 2014).

This work is the first to identify TRN-mediated intrathalamic neuromodulation by VIP as a source of bursting termination, which is consistent with the many studies highlighting the important role of TRN in shaping spindle activity.

3.4.2 NREM3 $\rightarrow$ NREM2 Sleep Cycle Transitions from Medium Timescale VIP Effects

VIP effects on the order of a biological hour-timescale led to transitions from NREM3 to NREM2. Potential biological mechanisms to account for this slow effect are receptor trafficking to the membrane and translation of new HCN channels during minutes of repeated VIP synaptic activity. A prediction from this result is that blocking VIP effects should prevent or delay transition to NREM2.

Spindles are Triggered by Synaptic Noise

The initiation for NREM2 spindles in the main sleep model differed from both the initial spindle model discussed above in section 3.4.1 as well as previous models (Des-

texhe et al., 1996) on which it was based. Specifically, the first spindle model had spindles initiate spontaneously—H-current modulation decayed, permitting T-current de-inactivation, which was followed by H-current depolarization which activated T-current. In the main sleep model, instead of waiting for spontaneous emergence of spindles, spindles were triggered by random Poisson synaptic noise.

Differing Synchrony is Responsible Delta versus Alpha Activity in NREM2

Furthermore, while Poisson synaptic noise to TC cells led to an anti-synchronous α spindles, synaptic noise to TRN cells led to brief bouts of synchronized δ bursts (section 3.3.2). Consequently, the ratio of the noise to TC versus TRN cells determines the prevalence of α spindles versus δ bursts, respectively. This follows from the *Synchrony* section results in section 3.3.2. Specifically, Poisson noise to a subset of TC cells initiates their firing, which leads to TRN bursting back onto the TC cells. The first TC subgroup were aligned by the input while the remainder are aligned in silence when the TRN cells fire, encouraging anti-synchrony between the two groups. In contrast, when the TRN cells are first activated by noise, all the TC cells are at a similar state of silence awaiting input, encouraging synchrony as the LTS burst together.

This NREM2 model fits experimental data more closely since human NREM2 is characterized by spindles co-existing with a few short delta bursts (Nir et al., 2011). Moreover, the model realistically yielded different spindle lengths and interspindle intervals (Contreras et al., 1997).

3.4.3   TC Cell Synchrony

PRCs for TC cells were calculated to better understand their synchronization. From the PRCs, GABA-A and GABA-B inputs to TC cells from TRN are expected to promote synchrony and anti-synchrony, respectively. Subsequent simulations supported

this prediction for GABA-B. However, GABA-A could promote either synchrony or anti-synchrony, depending on the other parameters. PRC theory has typically been used in simpler circuits than (Borgers, 2017). This explains why the results from the PRCs did not always match up with the simulation results. The wide range of synchrony behaviors seen here motivates the need for more theoretical research in systems of coupled rebound oscillators.

Increasing TRN–TRN gGABA-A consistently led to anti-synchrony. This is consistent with previous theoretical investigations which showed that rebound oscillations in mutually-coupled inhibitory neurons could lead to anti-synchrony (Wang and Rinzel, 1992; Skinner et al., 1994).

One question is why increasing gH can switch from synchrony to anti-synchrony, as in Figure 3·26. As gH increases, the bursting frequency increases. Since the phase response curves stayed about the same with respect to phase for different gH values, this corresponds to a shorter time to reach the global maxima for phase advancement. Thus, if the time lag to TRN GABA-A IPSPs was about constant, one would expect faster burst frequencies corresponding to higher gH to be more prone to anti-synchrony, as seen in Figure 3·26.

3.4.4 Post-REM Sleep Stage

In humans, REM is followed by a NREM2→NREM3→NREM2 cycle. This initial post-REM NREM2 stage was replicated in the simple non-spiking model (Figure 3·27) by adding post-REM decaying excitation that could result from brainstem acetylcholine (methods section 3.6.7). This is plausible since REM is associated with high acetylcholine (Scammell et al., 2017), whose excitatory effects (especially within TC cells) could take time to decay, causing the slow transition to deeper NREM3 after REM.

However, the full spiking model lacks this post-REM excitation since I hypothesize

that it is external to the thalamocortical circuit under investigation here and does not affect this work's main results. Furthermore, the minutes biological cAMP state variable is reset to 0 after REM periods, representing its decline during REM when TRN is not bursting and hence not releasing much VIP. The reset was necessary due to an artifact of the 8 cell model: since the model only had 2 cells of each type, the effective population synchrony remained relatively high during REM (i.e., even in full anti-synchrony, 1 cell firing is equivalent to 50% population synchrony), which led to continued VIP accumulation. In a larger model, REM would be associated with far less synchrony, so VIP would decline during REM and the reset would be unnecessary. Thus, Figure 3·28C reveals sharp declines in the minutes cAMP timescale state variable after each REM period. In a larger model, this decline would start at the beginning of REM.

Because the spiking model lacks the post-REM excitation, NREM3 follows REM without an intermediate NREM2 period, as seen in Figure 3·28. Future extensions to this model should incorporate a source of post-REM excitation to more realistically model the REM→NREM2→NREM3→NREM2→REM cycle.

3.4.5 Sleep Stage Architecture Modulation by Long Timescale VIP Effects

Intrathalamic VIP slow-timescale effects via cAMP can explain the trend of decreasing depth of NREM sleep between REM cycles during natural sleep, i.e. decreasing ratio of NREM3 : NREM2 sleep. This requires biological timescales on the order of hours, which is entirely feasible considering that cAMP-modifying neuromodulators in other systems maintain this timescale (Blum et al., 2014). Moreover, VIP-mediated effects in other nuclei last up to a week, suggesting involvement of nuclear effects such as increased HCN mRNA transcription and protein translation (Bourgin et al., 1997).

The model predicts that NREM3 thalamic bursting frequencies would progres-

sively increase after each NREM-REM cycle. Seemingly contradicting this prediction, a human EEG sleep study reporting spectrum data found that frequencies below 2 Hz decreased in power and shifted to lower frequencies over 4 successive NREM periods (Achermann and Borbély, 1997). However, since cortex has a slow wave mechanism separate from thalamus (Neske, 2015), the progressive increase in thalamic NREM3 bursting frequency with each NREM-REM cycle may be masked in common EEG analyses by cortex's internally driven slow pacemaker. Supporting the model predictions was the finding that the EEG spectrum peaks at $\approx$7 and $\approx$14 Hz (the latter may be a harmonic) increased slightly (up to 2 Hz) between NREM-REM cycles. This is consistent with the model if the thalamic bursting frequency started at 7 Hz.

In Vivo Studies

There are several relevant *in vivo* studies that involved sleep architecture modulation, specifically that thalamus plays a role in transitions between NREM and REM sleep. One used optogenetics to stimulate mouse TRN with a spindle-like α frequency; NREM-REM transitions increased, although average durations of those states did not change from baseline (Kim et al., 2012). Similarly, injecting PACAP (a VIP-analog) intracerebrally in rats led to increased NREM-REM transitions without changing the durations of these states compared to baseline (Fang et al., 1995). That TRN stimulation and VIP-analog infusion yielded the same result is consistent with the theory introduced here that TRN-VIP can control sleep architecture.

Although the NREM-REM transition was not modeled here as a direct VIP effect, VIP's actions in the model replicates the experimental observation that the transition from NREM to REM sleep (and wakefulness) correlates with continuously rising depolarization of TC and TRN neurons (Hirsch et al., 1983). Thus, VIP causes an effect in the model that correlates with NREM-REM transitions, consistent with the intriguing hypothesis (not explored here) that intrathalamic VIP can trigger a NREM-

REM transition. Notably, this novel idea is not mutually exclusive of the dominant theory that NREM-REM transitions are controlled by ascending neuromodulatory centers, like the brainstem and forebrain (Weber and Dan, 2016), since these structures strongly influence thalamus. It is also possible that there is dual-control of sleep stage transitions.

Considering the case that NREM-REM transitions are controlled exclusively by sources extrinsic to thalamus, how would intrathalamic VIP increase NREM-REM transitions? One explanation follows indirectly from VIP's pressure to keep thalamus depolarized closer to NREM2, since less external excitation would be required to transition thalamus to a depolarized state like REM. This hypothesis assumes that a depolarizing state transition in thalamus is required for REM, which is consistent with the evidence supporting thalamus' key role in arousal (discussed in section 3.2.11). If intrathalamic VIP's actions were blocked, the model predicts that it would be more difficult to achieve sufficient excitation to bring thalamus into REM, which would lead to longer NREM periods and altered REM electrophysiology.

A limitation of the *in vivo* experimental studies discussed in this section is that rodent sleep architecture is very different from humans, e.g. it is far more fragmented throughout a day (Genzel et al., 2014). Furthermore, rodent studies do not typically differentiate between NREM2 and 3.

Adenosine

Another candidate molecule for the continuously rising depolarization is adenosine (A1). Adenosine has the opposite effect on thalamic H-current from VIP (i.e, inhibitory), and is thought to act by decreasing cAMP levels (McCormick, 1992). Indeed, taking the adenosine receptor antagonist caffeine at bedtime increases human spindle power and decreases slow-wave power (Landolt et al., 1995), which is expected from H-current disinhibition; incidentally, this is consistent with the general idea that

H-current augmentation biases sleep toward NREM2. In addition, adenosine levels decline throughout a night's sleep (Porkka-Heiskanen et al., 2000), suggesting that adenosine's inhibition of thalamus would decline, leading to net TC depolarization during sleep. An alternative mechanism for indirect control of thalamus derives from the finding that adenosine reduced thalamocortical synaptic excitation of cortical neurons presynaptically, suggesting a role in reducing cortical excitation directly and thalamus indirectly (Fontanez and Porter, 2006).

There is also evidence against a direct role for adenosine in progressive thalamic depolarization. A study that increased adenosine levels in cat thalamus via infusion of the adenosine transport inhibitor NBTI found no changes in NREM sleep relative to wakefulness, as well as no change in the δ spectral power; however, augmenting the cholinergic basal forebrain adenosine did lead to increased NREM sleep (Porkka-Heiskanen et al., 1997). Furthermore, sleep deprivation led to increased adenosine levels in basal forebrain and cortex but not thalamus (Porkka-Heiskanen et al., 2000); sleep deprivation is known to cause longer sleep periods, especially NREM3 (Huber et al., 2000).

Together, these results support an indirect role for adenosine in changing thalamic H-current, probably through basal forebrain cholinergic modulation of thalamus. Its direct role in thalamus is possibly an auto-regulatory one—high neural activity builds up adenosine from ATP use (since adenosine is a degradation product of used ATP), leading to negative feedback on activity.

3.4.6   Other Studies of Sleep Architecture Control

A variety of different methods have revealed the presence of numerous centers that can affect the initiation, maintenance, and termination of awake, NREM, and REM arousal states (Weber and Dan, 2016). While the period of ultradian sleep oscillations generally correlates with brain size (Weber and Dan, 2016), the mechanisms

determining these durations remain unknown. A recent review suggested that the mutual inhibition between NREM- and REM-active neurons may create an oscillator responsible for the ultradian period (Weber and Dan, 2016). While coupled inhibitory oscillators are capable of producing synchronized and robust rhythms (Whittington et al., 2000), it is not obvious how these antagonistic neural circuits create such long timescales.

It is possible that brainstem centers and intrathalamic neuromodulation interact to sculpt sleep architecture. For example, intrathalamic neuromodulation may serve the role of depolarizing thalamus into a relay mode that is more receptive of brainstem control for switching from NREM to REM or wakefulness.

3.4.7 Anesthetics

Finally, propofol anesthesia both directly and indirectly counteracts VIP modulation, maintaining thalamus in a sustained burst mode unsupportive of consciousness (Alkire et al., 2000).

Propofol Alpha Oscillation

A previous computational model (Ching et al., 2010) suggested that the anesthetic α frequency depends on a thalamic resonance to the α band induced by the propofol-mediated prolongation of the GABA-A decay time-constant; meanwhile, strong spectral power is due to enhanced TRN-mediated rebound excitation in TC cells because of augmented GABA-A conductance, causing TC synchronization. Importantly, the paper noted that the model under high-dose propofol is actually in the spindling regime, whose typical waxing-and-waning pattern is masked due to cortical excitation. One key difference between the spindle α in the Ching model and the current model (as well as previous models on which the Ching model was based (Destexhe et al., 1996)) is that the Ching model TC cells are synchronized when engaged in the

propofol α, discussed below.

Here, an alternative propofol α mechanism is proposed. α frequencies in this model require reduced cortical drive to the thalamus, which occurs under propofol due to augmented GABA-A conductance, as well as reduced brainstem inputs *in vivo*. The loss of cortical excitation prevents synchronization of thalamus, permitting it to enter anti-phase bursting at multi-unit α, single-unit δ.

Synchronous Propofol Alpha in Previous Models

Section 3.3.3 explained how synchrony is associated with the continuous δ bursts while anti-synchrony characterizes the α spindles in this work's thalamic model. An early computational study reported that TC cells with 10 Hz α GABA-A synaptic inputs could entrain to half the frequency at 5 Hz δ with lower GABA-A conductances (Destexhe et al., 1996); however, entrainment at α was possible by increasing the GABA-A conductance. Since propofol increases the TRN→TC GABA-A conductance, it makes sense that previous thalamic models of the propofol anesthetic state describe a continuous synchronized α oscillation in TC cells (Ching et al., 2010; Soplata et al., 2017).

In those studies, propofol was modeled as an increase in the GABA-A conductance and decay time constant. The latter effect should not cause stabilization according to the PRC results in Figure 3·24 showing that a slightly longer decay time constant should still favor anti-synchrony; although the change in decay time was reported as being important for the cortical α (Ching et al., 2010). Likewise, the larger GABA-A conductance would be expected to also favor anti-synchrony as revealed by simulations of varying degrees of noise and gGABAa. However, a strong excitatory cortical drive would synchronize the TC cells, as revealed by the type 1 PRC for excitation in Figure 3·23. In addition, Soplata et. al's isolated thalamus only presented continuous propofol α with a slight increase in tonic applied current—it is possible that this

changed the PRC from type 2 to type 1, permitting a stable synchrony.

Dexmedetomidine

Dexmedetomidine is an α2-adrenergic receptor agonist that produces a neural state similar to a constant NREM2 with few bursts and ample spindles, but not REM transitions (Huupponen et al., 2008). Dexmedetomidine is a weaker agent not typically used alone in the surgical or critical care settings since patients tend to be too arousable. The α2-adrenergic inhibition is thought to harness the natural sleep pathways in brainstem (Brown et al., 2010), which helps explain its weaker effect. Assuming that dexmedetomidine's predominant effect is in brainstem, it would withdraw neuromodulator activity from thalamus, which would bring thalamus into burst mode. Its weaker efficacy would enable VIP to cause transition from the NREM3 to NREM2 excitation level. Presumably, direct inhibition of brainstem centers responsible for REM would then prevent the NREM2 to REM transition, keeping the thalamocortical circuit in a spindling regime. However, a sufficiently strong stimulus would be able to overcome this brainstem inhibition, leading to positive feedback of excitatory activity that would awaken a person.

3.4.8 Homeostasis From Intrathalamic Neuromodulation

A concept that unifies each of the results is that VIP provides a mechanism for depolarizing thalamocortical (TC) neurons toward and across the burst-relay mode border, when starting from burst mode. This depolarizing drive at different timescales leads to the major results.

Taking a broader view, this unilateral VIP-mediated depolarization forms a homeostatic mechanism keeping thalamus near the burst/relay border (Figure 3·31). If the thalamus starts deep in burst mode, intrinsic VIP slowly depolarizes thalamus, increasing its burst rate. This forms a positive feedback since the faster bursting leads

to more average VIP release. This continues until thalamus reaches the burst/relay border. Thus, while weak cortical inputs might not be relayed initially, they would be after thalamus depolarizes sufficiently. Conversely, if the thalamus starts in a depolarized relay mode and excitation is withdrawn, it would hyperpolarize toward the burst border. After crossing the border, VIP would act to depolarize cells back across the border. The simulations here suggest that in the absence of high levels of excitation, TC cells will attract toward the burst/relay border and subsequently stably oscillate around the border.
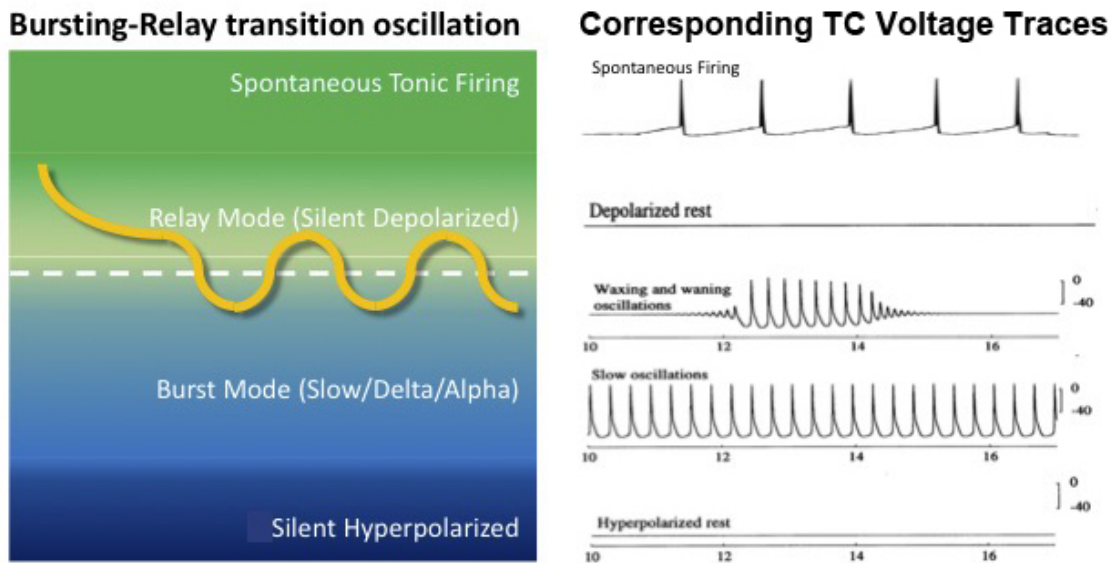
Figure 3·31: VIP homeostatically keeps thalamus on the firing mode transition boundary. With the withdrawal of excitatory input, thalamus will move from the relay mode (green) to the burst mode (blue). VIP acts to keep thalamus near the boundary between the two firing modes. Oscillations around the border occur since the silent depolarized state has no VIP activity, and tonic firing has much less VIP activity than the burst mode. Hence, there is a tendency to drop back into burst mode, and then rise again into relay mode. Right panel adapted from (Destexhe et al., 1993a).

3.4.9 Intrathalamic Neuromodulation in Recovery From Disorders of Consciousness

One hypothesis about the role of thalamic homeostasis in a pathologic state is that it may contribute to recovery from disorders of consciousness (DOC) after severe brain

injury. Reduced levels of consciousness after brain injury is often associated with a reduction in thalamocortical connectivity (Giacino et al., 2014), which would hyperpolarize thalamus into the burst mode unsupportive of normal consciousness (Weyand et al., 2001). VIP release during burst mode would eventually bring thalamus into relay mode, permitting greater thalamocortical connectivity and conscious cognition. Indeed, functional magnetic resonance imaging (fMRI) studies reveal greater thalamocortical connectivity after recovery of consciousness post-brain injury (Laureys et al., 2000). While this mechanism would improve functional connectivity, the most severe injuries may require additional structural changes that can take even longer periods, i.e. > weeks (Thengone et al., 2016).

It should be noted that the results of a recent study appear on the surface to conflict with this hypothesis (Magrassi et al., 2018). Thalamic spiking was recorded extracellularly from patients with disorders of consciousness under sevoflurane general anesthesia. The majority of recorded single units fired single spikes instead of bursts of multiple spikes. Hence, the authors concluded that the majority of thalamus was not in burst mode. One issue with this analysis is that low-threshold spike (LTS) bursts can have 1 or more spikes. Thus, if these thalamic neurons fired only single spikes during the bursts, they would be misclassified. Intracellular recordings would be required for confirmation. Even if the single-spiking neurons were in relay mode, there is still a complicating factor. The sevoflurane level used, although low for a healthy patient with normal connectivity, may have hyperpolarized many of the bursting cells into silence (Destexhe et al., 1993a), spuriously elevating the ratio of cells in relay vs. burst mode.

3.4.10 Future Modeling Directions

There are several next steps to this line of research. They involve increasing complexity within thalamus and adding more brain regions.

Brainstem

One intriguing direction would be to explicitly model brainstem interactions with the thalamocortical circuit during sleep and anesthesia. There are several existing phenomenological models of sleep that could be combined with the thalamocortical model described here (Booth and Diniz Behn, 2014). It would be especially interesting to add thalamocortical feedback to these models and test hypotheses about brainstem versus thalamic control of sleep architecture. The combined model could also be used to study anesthesia by changing the relevant parameters for brainstem. The brainstem is not typically modeled along with the thalamocortical circuit, so there would be great value in examining this combination more closely.

Zona Incerta

Another brain region with strong influence to consider is zona incerta. This extrathalamic nucleus sends inhibitory connections predominantly to the intralaminar thalamus of interest here (Bartho et al., 2002). It would be modeled like TC cells but without bursting currents, VIP, and TC feedback.

Conduction Delays

An additional feature to investigate is the impact of conduction delays since the thalamocortical model spans large neural distances. Theoretical investigations have demonstrated that conduction delays can affect synchronization and wave formation (Crook et al., 1997; Ermentrout and Kopell, 1998). This is especially relevant for studying slow wave propagation and spindle synchronization in a larger model (Bazhenov et al., 2002).

Thalamic Interneurons

Thalamic interneurons have been most studied in the lateral geniculate nucleus of thalamus related to visual processing, but are also found in other thalamic nuclei (Jones, 2012). Since VIP has been found not just in TRN cell bodies, but also within neurons of relay nuclei (Burgunder et al., 1999), it is most likely that there are VIP-containing interneurons. It would be interesting to model neuromodulation from these interneurons versus TRN and the consequent affects on oscillations.

Cortical Slow Waves

There is an extensive experimental and theoretical literature on the origins of sleep slow waves, as well as the relative contributions of cortex and thalamus (Amzica and Steriade, 1998; Crunelli and Hughes, 2009; David et al., 2013; Lemieux et al., 2014; David and Schmiedt, 2014; Neske, 2015; Crunelli et al., 2015; Gent et al., 2018). Notably, a recent human magnetoencephalographic (MEG) study found that spindles occur at preferential phases of the cortical slow wave (Klinzing et al., 2016). It seems that cortex is likely the main source of slow waves, but they can also be initiated and modulated by thalamus (David et al., 2013; David and Schmiedt, 2014; Neske, 2015; Crunelli et al., 2015; Lewis et al., 2015; Gent et al., 2018). Thus, it would be interesting to investigate the impact of thalamically-triggered cortical slow waves on the VIP spindle mechanism and model the phase relationship between the cortical slow waves and thalamic spindles. Furthermore, slow timescales of VIP modulation could contribute to a thalamic pacemaker for the cortical slow oscillations.

Other cAMP Modulators

The explicit modeling of cAMP in this relay thalamus model enables the study of other neuromodulators besides VIP since many converge on the cAMP pathway; e.g., adenosine, nitric oxide, serotonin, and norepinephrine (McCormick, 1992). Thus, this

model provides a useful tool for future studies of thalamic neuromodulation (Figure 3·32).
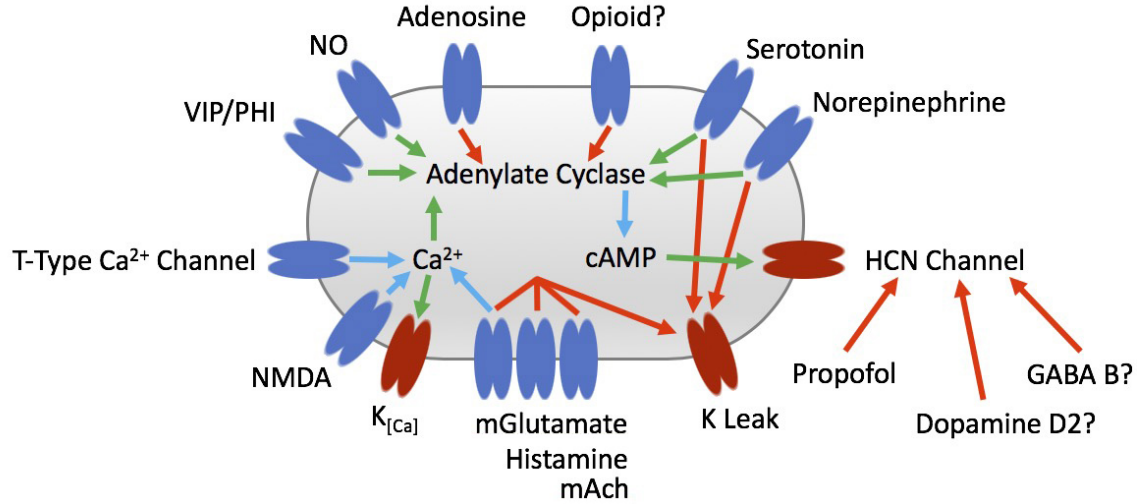
Figure 3·32: A framework for future studies of thalamic neuromodulation using explicitly modeled cAMP. Many neuromodulators converge on the calcium and cAMP pathways, and also affect potassium leak channels.

It may also be useful to explicitly model adenylate cyclase and phosphodiesterase in some cases. For example, adenylate cyclase isoforms are differentially modulated by calcium, which is relevant for thalamic cells since they possess T-type calcium channels. This approach was initially considered for the present work, but the additional complexity was not warranted for this preliminary study. Additional data may be necessary though to constrain the additional kinetic terms needed.

3.4.11 Experimental Validation

There are several predictions of this model that may be tested experimentally to validate the model's main results:

- Seconds VIP: Antagonizing VPAC2 receptors in centromedial nucleus during NREM2 spindles will reduce or prevent spindles (motivated by section 3.4.1).

- Strong VPAC2 receptor agonism in centromedial nucleus during NREM3 should lead to NREM2 spindling (motivated by section 3.4.2).

- 90 Minute VIP: Antagonizing VPAC2 receptors in centromedial nucleus during NREM3 will prevent or delay transition to NREM2 (motivated by section 3.4.2).

- Hours VIP: Antagonizing VPAC2 receptors in centromedial nucleus will lead to longer NREM periods and aberrant REM electrophysiology, or alternatively prevent REM entirely (motivated by 3.4.5).

- Hours VIP: NREM3 delta oscillations in human thalamus will increase in frequency with each successive NREM-REM cycle during sleep

- TRN optogenetic stimulation mimicking δ bursting will lead to short-term inhibition followed by prolonged excitation. One can voltage clamp TC cells within the H-current activation but below the T-current activation window to check for a growing inward current.

3.5   Conclusions

Here, I use computational models to introduce the concept of intrathalamic neuromodulation control of NREM sleep architecture and demonstrate that its homeostatic mechanism is counteracted by general anesthesia. This new hypothesis motivates new experimental studies that could help improve understanding of sleep architecture control, relevant to many human sleep disorders.

These results also demonstrate the utility of computational models for testing *in vivo* hypotheses based on *in vitro* data. Furthermore, the models permit interrogation of various time-varying biophysical parameters that would impossible or difficult to measure empirically.

3.6   Methods

3.6.1   Thalamocortical Model Simulation

To explore the role intrathalamic VIP in a thalamocortical circuit, a computational model of single compartment conductance-based Hodgkin-Huxley-type point neurons was simulated using the DynaSim toolbox for MATLAB (Sherfey et al., 2018). These models are conductance-based because neurons are modeled as electrical RC circuits: the membrane acts as a capacitor, storing charge; each ion channel is represented by a resistor and voltage source, with resistance equal to the inverse of the ion channel's conductance and voltage equal to the ionic reversal potential. These models possess greater biophysical realism than other commonly used models such as integrate-and-fire and mean-field models, since each parameter represents a biophysical correlate that can be measured experimentally. These models are scalable in size and complexity while remaining computationally tractable to simulate.

The actual substrate of the model is a system of ordinary differential equations that must be solved numerically. Numerical integration is performed using a 2nd-order Runge-Kutta method with a fixed time step of 0.005 ms. Some results derive from simulations of the isolated thalamic submodule, as indicated in the results section.

The model is comprised of 2 or 20 neurons of each neuronal population as indicated in the text. The model with 2 cell populations represents two highly synchronized subpopulations of each neural type and is useful for demonstrating synchrony vs. anti-synchrony. The larger models permit more phase differences between cells and captures the behavior of a more realistic network with greater heterogeneity and noise.

Compression of Simulation Timescale

The physical timescales modeled here range 8 orders of magnitude, from spiking at 10^{-4} seconds to sleep at 10^4 seconds. Furthermore, there is a bimodal distribution of

timescales with most being very fast, and a couple VIP ones being far slower. This large separation of timescales means that one can speed up the slow VIP timescales by several orders of magnitude and still have similar qualitative results, which has great advantages for reducing computation time. Thus, an 8-hour night's sleep is represented by approximately 2 minutes of model time. This time compression follows that of other sleep models using spiking neurons (Krishnan et al., 2016).

3.6.2 Conductance-Based Model Specification

Single compartment conductance-based Hodgkin-Huxley-type point neuron models were used a typical equation structure as follows.

Voltage changes over time were calculated using the following standard cable equation:

$$C_m \frac{dV}{dt} = - \sum (I_{int} + I_{syn}) + I_{app}$$

Membrane and synaptic currents used a Hodgkin-Huxley-type conductance:

$$I = \bar{g} m^n h^k (V - E_{rev})$$

For the full model specification including equations and parameter values, see appendix A on page 145. For a more thorough exposition on this type of modeling method in the thalamocortical circuit, consult the monograph *Thalamocortical Assemblies* by Alain Destexhe and Terry Sejnowski (Destexhe and Sejnowski, 2001).

3.6.3 Thalamocortical Relay Nucleus Model

The thalamic model was based on the canonical Destexhe thalamic model, which is constrained by ferret thalamic slice experimental data (McCormick and Huguenard, 1992; Destexhe et al., 1993a; Destexhe et al., 1996). As is commonly practiced, the thalamic model incorporates a non-specific relay nucleus and the thalamic reticular nucleus (TRN). The relay nucleus is not typically specified in modeling papers since the measured intrinsic properties of the thalamocortical (TC) neurons have surpris-

ingly little diversity across many thalamic nuclei (Destexhe and Sejnowski, 2001). In the current context, the relay nucleus is considered a higher-older thalamic region relevant to arousal, specifically the centromedial nucleus of the intralaminar thalamus (Van der Werf et al., 2002; Baker et al., 2014).

The TC neurons of the relay thalamus contain the standard sodium and potassium spiking currents of the Hodgkin-Huxley formalism along with potassium leakage currents. The unique currents are the H- and T-currents. The H-current is hyperpolarization-activated non-selective cation channel. The T-type calcium current is activated around the reversal potential for the H-current. If a TC neuron is hyperpolarized, the T-current is de-inactivated, while the H-current serves as a pacemaker current that raises the membrane potential to the T-current activation threshold, which then initiates a barrage of low-threshold spikes (LTS), initiating the thalamic burst mode. Like previous models, this model contains dynamics for calcium representing a thin shell inside the membrane, driven by the inward T-type calcium current. These transients local to the membrane are hypothesized to be most relevant for modulating the membrane HCN channels. Hence, general cytoplasmic calcium and endoplasmic reticulum calcium stores are not considered.

Two Types of H-Current Modulation

As diagramed in Figure 3·13, two sources of H-current modulation are considered here: VIP and calcium. As discussed in section 3.2.7, direct calcium modulation is a simplification of its indirect actions on HCN channels. In reality, both pathways ultimately modify cAMP, as described in section 3.2.2 and outlined in Figure 3·1.

H-Current Modulation By Calcium

The original Destexhe model featured closed, open, and calcium-bound open states for the H-current. The calcium-bound state featured a modifier that doubled the increase

in H-current conductance (gH). This calcium-bound state is what terminated spindles after a period of time. However, the slow receptor kinetics made spindles occur only every ≈ 30 sec. The calcium-modulated H-current mechanism corresponding to Figure 3·13B was only used for results in section 3.3.1.

To reduce simulation time and reproduce more realistic interspindle intervals, the kinetics were sped up. This modification also permitted a larger interspindle interval range with spindles recurring every few seconds to a minute, depending on the maximal H conductance. This kinetic change did not impact the relevant results in section 3.3.1.

H-Current Modulation By VIP

In addition to the calcium mechanism, VIP augmentation of H-current was explored here (Figure 3·13A). As detailed in appendix A, gH modulation by VIP is via an additive term. This is a simpler formalism than including a separate second-messenger-bound HCN state as with calcium in the original Destexhe model, described above. The separate state formalism would require an additional kinetic time constant that lacks adequate constraint. Since both VIP modulation forms yielded similar qualitative results for spindle production as in section 3.3.1, the more parsimonious form was chosen for the results presented here.

3.6.4 Thalamic Reticular Nucleus Model

The reticular thalamus model is very similar to the TC model. A key difference is that it lacks the HCN pacemaker current. Secondly, its T-current differs from that in TC neurons, as revealed by experimental data (Huguenard and McCormick, 1992). This T current inactivates more slowly and does so in a mostly voltage-independent manner. Hence, it is referred to as T_s.

The different T channel kinetics lead to different intrinsic low threshold spiking

properties between TC and TRN cells. Experimentally, TC cells burst with 2-10 spikes over a period of 8 ms, while TRN cells fire bursts of many action potentials over an early 50-100 ms period with spike frequency modulation followed by tonic firing for up to hundreds of ms (Domich et al., 1986).

3.6.5 Cortical Model

The cortical model contains two neuronal populations, based on the excitatory (E) regular spiking (RS) pyramidal neurons and inhibitory (I) parvalbumin-positive fast-spiking (FS) interneurons from (McCarthy et al., 2008). Both RS and FS cells contain the sodium and potassium spiking currents as well as potassium leak currents. In addition, the RS neuron model has a slow depolarization-activated potassium M-current, responsible for spike-frequency adaptation. It is named "M" because in physical neurons the activity of the muscarinic acetylcholine receptor inhibits it—this effect is not modeled here.

3.6.6 Synaptic Connectivity

The thalamocortical model synaptic connectivity is diagramed in Figure 3·33 and based on two prior models (Destexhe et al., 1996; Destexhe et al., 1998). Connectivity is all-to-all for each type of connection unless otherwise stated.

Thalamic Connectivity

The relay thalamus is the sole source of outgoing signals from the thalamus, whereas the reticular thalamus makes only intrinsic thalamic synapses. Connectivity within the thalamus between the TC and TRN cells is the same as the canonical model (Destexhe et al., 1996), with the addition of the VIP neuromodulator. TC cells form excitatory α-amino-3-hydroxy-5-methyl-4-isoxazolepropionic acid (AMPA) connections onto TRN cells and cortical RS cells.

Figure 3·33: Model Synaptic Connections. (A) Connections with the thalamus. (B) Connections within the full thalamocortical model network graph. Cortical E cells make AMPA connections. Cortical I cells make GABA-A connections.
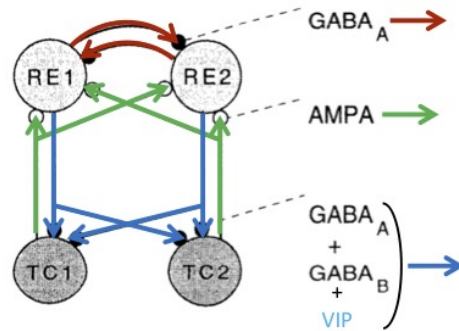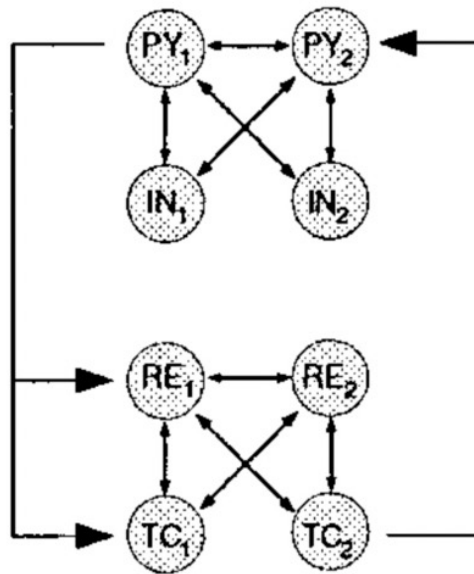
The model TRN forms γ-aminobutyric acid (GABA) synapses both with itself (including autapses) and TC cells. The autapses are present since each model neuron symbolizes the activity of a small synchronized local population of neurons. Self-connections have GABA-A receptors, while synapses with TC cells have both GABA-A and longer acting GABA-B receptors. GABA-A receptors have a similar timescale to AMPA receptors, ≈ 10 ms. GABA-B receptors are modeled with cooperativity, so they are mostly active during bursting, and provide a delta frequency (≈ 4 Hz) timescale.

Connectivity within reticular thalamus has a rich literature of different and sometimes contradictory findings across species. The reticular thalamus is known to have dendro-dendritic synapses and self-collaterals within the nucleus (Landisman et al., 2002; Deschenes et al., 1985; Yen et al., 1985; Pinault et al., 1997). Asymmetric excitatory chemical synapses have been described from electron microscopy investigations (Pinault et al., 1997). Intra-TRN GABA-A connections have also been identified (Deschenes et al., 1985; Yen et al., 1985), as well as weak GABA-B—the GABA-B is ignored here due to its weakness (Ulrich and Huguenard, 1996), although it has been studied in computational models previously (Golomb et al., 1994). Furthermore, electrical synapses have been found between pairs of TRN neurons (Landisman et al., 2002). As has been done in previous computational models to incorporate the complexity of intra-TRN connectivity in a parsimonious fashion (Destexhe et al., 1996), this work uses solely intra-TRN GABA-A synapses that tend to be excitatory, which has been empirically observed (Bazhenov et al., 1999). As noted by Destexhe and Sejnoswki, this makes the model more stable by inhibiting activity if it is too high; i.e., average membrane potential increases above GABA-A reversal potential (Destexhe and Sejnowski, 2001). Since these neurons are capable of bursting when hyperpolarized by either excitatory or inhibitory PSPs, the excitatory GABA-A does

not affect the results here.

Cortical Connectivity

Cortical RS cells have AMPA synapses to other RS cells and FS interneurons, as well as thalamic TC and TRN cells. FS cells only have GABA connections to RS cells (containing GABA-A receptors). Synaptic connectivity between thalamus and cortex is similar to (Destexhe et al., 1998), except there are no TC to FS AMPA connections.

3.6.7   Simplified Non-Spiking Sleep Model

A simplified non-spiking model was used to demonstrate the utility of the two slower VIP timescales for shaping sleep architecture using the hours-long biological timescale as the model timescale. This model is based on the thalamic module of the full spiking model, but with slower time constants to match the correct timescales for an $\approx$8 hour human night's sleep.

Another key difference from the spiking model is the addition of post-REM excitation from brainstem acetylcholine. This excitation more realistically replicates the post-rem transition from NREM2 to NREM3 before transition back to NREM2. In the spiking model, NREM3 immediately follows REM without a NREM2 intermediary since there is no post-REM source of excitation added to the model. This is discussed more fully in discussion section 3.4.4.

Chapter 4

GIMBL-Vis: a Graphical Interactive Multi-dimensional extensiBLe Visualization Toolbox for Matlab

4.1 Abstract

Computational models of neural circuits exhibit diverse behaviors, including many that are unexpected or difficult to predict. Numerical simulations are useful for characterizing the dynamics of these high-dimensional systems. An increasingly vexing issue is the difficulty in visualizing and analyzing how properties of these models change as multiple independent parameters are varied in simulations. Here, I introduce GIMBL-Vis, a Matlab toolbox for visualization of such multi-dimensional datasets. This toolbox simplifies the process of exploring multi-dimensional data in Matlab by providing a graphical interface for visualization and analysis. The interface features sliders for each data dimension, controlling dynamic slicing through 2D and 3D slices of a dataset to reveal the effects of varying specific parameters. The toolbox is a useful complement for neural simulators, including our group's recently developed Dynamic Neural Simulator (DynaSim). Furthermore, since it supports datasets in table form, it may be used for diverse sources of data.

4.2   Introduction

4.2.1   Big Data

Since technological advances have made it possible to collect data on a scale previously unimaginable, the twenty-first century has been deemed the era of "big data". Neuroscience is no exception. For example, multi-electrode arrays and calcium imaging make it possible to record from hundreds to thousands of neurons simultaneously. In addition to experimental datasets, modern computing clusters have enabled the generation of comparably enormous *in silico* datasets. The data size will continue to increase as groups continue to push toward simulating entire brains at the individual neuron level. Computational methods are essential for deriving insights from this deluge of data overwhelming scientists.

4.2.2   Neural Circuit Simulation

While theoretical computational methods are important, the engineering of tools both physical and virtual is also crucial. For the field of computational neural circuit modeling (see section 1.3.1), many choose to use a neural simulator software package. There are several common neural simulation environments (Brette et al., 2007), including NEURON (Hines and Carnevale, 1997), NEST (Diesmann and Rechnen, 2001), GENESIS (Wilson and Bhalla, 1989), and Brian 2 (Stimberg et al., 2013). Since none were available for Matlab, our research group created the Dynamic Neural Simulator (DynaSim), a Matlab modeling and simulation toolbox for solving systems of differentials equations, especially those of Hodgkin-Huxley style conductance-based point neurons (Sherfey et al., 2018).

Computational Modeling Datasets

Neural circuit models exhibit diverse behaviors, including many that are unexpected or difficult to predict. Hence, during the process of developing circuit models, it is important to test a range of values for different parameters, both to explore different regimes of dynamics and to check the robustness of findings. Even "tiny" models with only a few cells can possess hundreds of parameters and generate terabytes of data when simulating over combinations of varying parameters. For example, simulating the Cartesian product (i.e., every combination in a lattice grid) of 5 parameters with 10 values each yields a 5D dataset of $10^5 = 10,000$ simulations.

Modeling Case Studies: Stomatogastric Ganglion Neurons and Networks

Several notable modeling studies that highlight the importance of checking multiple parameters are from Eve Marder's group.

One study looked at 600 thousand parameterizations over 17 dimensions of a stomatogastric ganglion lateral pyloric (LP) neuron (Taylor et al., 2009). 1300 of these models fit the experimentally measured electrophysiological properties well. A key questions was whether the parameters were correlated with one another. One technique the paper uses to describe the dataset was 2D histograms of pairwise correlations between parameters.

Another paper examined 20 millions parameterizations over 10 dimensions of a simplified 3-cell network model of the stomatogastric ganglion (Prinz et al., 2004). About 2% of the models generated output resembling empirical findings according to 15 features. These plausible models varied tremendously, including different synaptic connectivities. The data was summarized with histograms for each feature.

DynaSim

A key strength of DynaSim is that it simplifies the process of exploring a large parameter space with massively parallel simulation, such that a batch of 10,000 simulations run in parallel on a computing cluster is not atypical. This presents a data visualization problem, as each simulation has several parameter dimensions of interest. For example, viewing the voltage over time or ion channel conductance over time is often desired. Furthermore, different views or functions of these variables are also informative, including spike rastergrams and power spectrums. These goals motivate the need for visualization tools.

4.2.3 Existing Visualization Solutions

There are many options for data visualization, and the toolset differs for each of the commonly used data science languages, i.e. R and Python. Each tool offers varying degrees of integration into common workflows, as well as different levels of automation.

Simple solutions involve manually creating plots. A popular option is ggplot2 for R (Wickham, 2016), an implementation of Wilkinson's grammar of graphics (Wilkinson, 2011), which also has ports for Python. Interactive plots can be made easily with tools like Shiny from RStudio (Racine, 2011), or the Jupyter Notebook for Python (Ragan-Kelley et al., 2014).

A recent trend is the creation of tools that automate the creation of plots. Typically these use either a series of heuristic rules or an artificial neural network in the background to generate visualization recommendations. Examples include Vega Voyager (Wongsuphasawat et al., 2017) and data2Vis (Dibia, 2018) for Python.

Matlab Standard Library Options

While there are numerous solutions for visualizing rich datasets in the open-source languages R and Python favored by the data science industry, there is a paucity of visualization tools for Matlab, commonly used in many research settings. In particular, Matlab provides neither a rapid nor simple solution for visualizing >3D datasets, including the multi-dimensional neural datasets mentioned previously. The closest option is the *slice* function of the Matlab standard library (Figure 4·1). The slice tool creates a static view and is labor-intensive, requiring manual specification of the data as a numeric matrix (listing 4.1). It is highly cumbersome to use with a >3D dataset, if one wishes to change the slice positions, or with non-numeric data.

Listing 4.1: *Slice* function example code from Matlab documentation for Figure 4·1

```
[X,Y,Z] = meshgrid(-2:.2:2);
V = X.*exp(-X.^2-Y.^2-Z.^2);
xslice = [-1.2,0.8,2];
yslice = [];
zslice = 0;
slice(X,Y,Z,V,xslice,yslice,zslice)
```

MatImage Toolbox

As for user-created visualization tools for multi-dimensional data, only one was easily found: the MatImage toolbox (https://github.com/mattools/matImage). Intended for use with medical and scientific imaging data, it provides a library of image processing functions as well as three interactive tools. Each tool appears in a different figure window (Figure 4·2). The *Slicer* tool contains the main graphical user interface (GUI) with various functions accessible by dropdown menus from the toolbar. The main *Slicer* interface provides a slider for slicing through a 3D image with a single 2D plane. The *orthoSlices* window expands on the built-in *slice* function, permitting dynamic slicing by clicking and dragging the planes. Finally, the *OrthoSlicer3d* win-
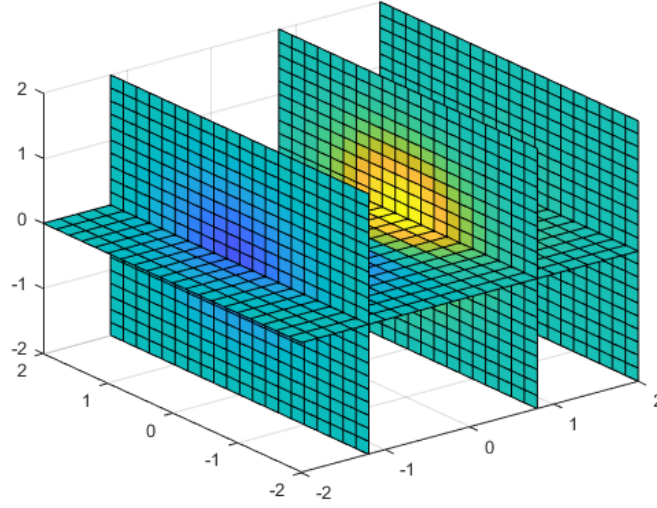
Figure 4·1: Matlab *slice* function view output

dow shows three 2D slice planes. Crosshairs on any of the planes may be dragged to change the views in the other planes. A bonus feature is the capability to render the 3D image into an isosurface. Like the Matlab *slice* function, the toolbox is limited to a single 3D numerical dataset.

Visualizing Simulation Results

To visualize simulation results, a typical solution in our group is to view a linear list of pre-generated figures. This is tediously inefficient and slow for hundreds or thousands of simulations, different figure types, or lattice sweeps over multiple parameters. The latter is especially problematic since multi-dimensional data often has structure across dimensions which leads to repeating patterns during a linear viewing that can be hard to interpret correctly. In summary. an increasingly vexing issue is the difficulty in visualizing and analyzing how properties of computational models change as multiple independent parameters are varied in simulations. There is an urgent need for visualization software that simplifies the process of viewing multi-dimensional data rapidly.
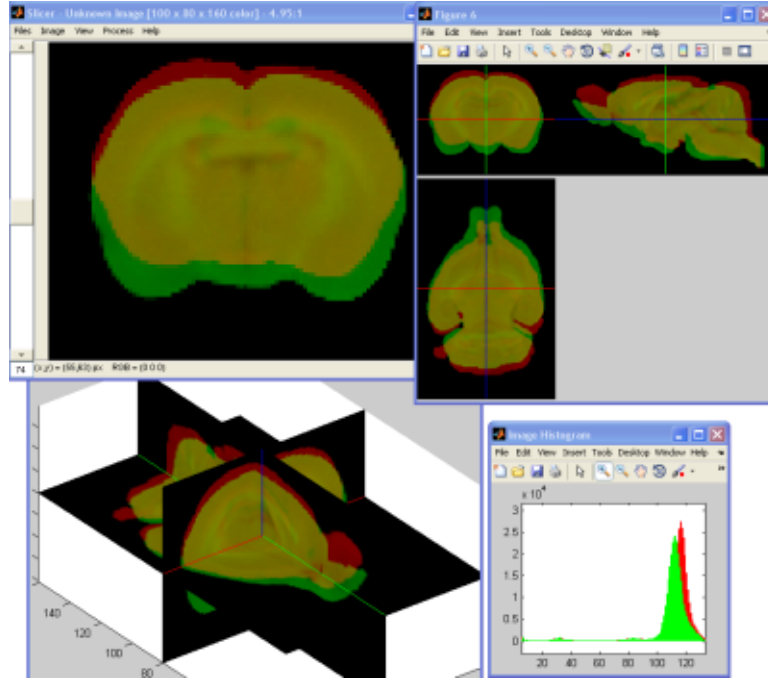
Figure 4·2: MatImage toolbox for Matlab

The MatImage toolbox is useful for basic imaging applications, but is ill-suited for the multi-dimensional datasets generated by simulations or electrophysiological recordings, which often require multiple different views of not just the raw data but also functions of the data. In general, it is difficult to overcome the reality that humans tend to think and see in 3D. One common solution is to employ techniques of multidimensionality reduction, mapping a high-dimensional dataset into a lower dimensional space (Cunningham and Yu, 2014). However, this is not possible for many dataset (e.g., non-numeric data) and is not always desired. An example of the former is when one desires preservation of the original axes, as in the case when the dimensions have a physical meaning that would be obfuscated by combining dimensions.

4.2.4 The GIMBL-Vis Solution

When I began my modeling work, there did not yet exist an efficient Matlab workflow for visualizing the results of model simulations when varying over multiple parameters (section 4.2.3). To solve this problem, I created **GIMBL-Vis** (GV): a **G**raphical **I**nteractive **M**ulti-dimensional extensi**BL**e **Vis**ualization toolbox for Matlab (Roberts, 2017). This toolbox simplifies the process of exploring multi-dimensional data in Matlab by providing a graphical interface for visualization and analysis. Notably, it is built with an extensible plugin system at its core, enabling customization for specific projects and the addition of new features over time from the user base. The current plugins, described in section 4.3 below, provide an indispensable toolkit for working with multi-dimensional data.

4.3 Design

4.3.1 Design Philosophy

A disadvantage with proprietary black-box scientific software is the inability to adapt it to one's particular usage case as well as the inability to fix bugs oneself when they arise. In contrast, GIMBL-Vis is free and open-source software (FOSS) with a liberal license, meaning that users are welcome to adapt it to their needs. Hosted on GitHub, users can submit new features and bug fixes, providing a software experience mirroring the culture of academia more broadly.

Free, open-source scientific software is a beautiful concept that when implemented well is appreciated by academics everywhere (Prlić and Procter, 2012). Unfortunately, practical considerations such as lack of funding or software experience of the "developers" conspire to render many field-specific packages lackluster at best, unusably plagued by bugs at worst. An approach that mitigates some of these issues is to build on a stable software foundation that has an experienced, committed developer base,

such as Python or Matlab. This approach was adopted for DynaSim and GIMBL-Vis.

4.3.2 GV Class

GIMBL-Vis is implemented in a series of different classes to permit the use of an object-oriented programming paradigm, an advanced feature of Matlab seldom used. The application is accessed through the *gv* class. Simply calling **gv** will call the constructor and will return an object of the *gv* class. To open the GUI window and use the interactive graphical mode, it requires calling the **run** object method on an existing object, or the **Run** class method (listing 4.2). The **gv** constructor can also take arguments as a shortcut to load data from the workspace, a file, or a directory containing a single data file.

Listing 4.2: Opening the GV application

```
%--Open GV GUI without an explicit data source--
% 3 ways:

% 1) Using constructor followed by method call
gvObj = gv;
gvObj.run();

% 2) Using class method
gv.Run; % or `gvObj = gv.Run;`
gvr; % or `gvObj = gvr;`

% 3) using constructor with simultaneous method call
gv().run; % or `gvObj = gv().run;`
```

4.3.3 Data

Data Sources

GIMBL-Vis is not limited to use with neural simulators like DynaSim or neuroscientific electrophysiological datasets. Since GV can import any dataset that can be

represented in table form (e.g., a CSV or Microsoft Excel file), it may be used with diverse sources of data.

Data Model

GV's data model is depicted in Figure 4·3. At the lowest level, GV data is ultimately stored in an array—a multi-dimensional array for numeric data, or a cell array for mixed and non-numeric data. Non-lattice data is supported with NaN (not-a-number) entries for numeric arrays, or empty cells for cell arrays. One level up, the data array is contained inside a *gvArray* object. The class inherits from the Multidimensional Dictionary (MDD) data structure, created by our group to store multi-dimensional data along with axis information and metadata to facilitate multi-dimensional visualization. MDD objects contain many useful low-level data wrangling methods, including those for slicing data subsets and merging data. The subclass inheritance permits extension of the MDD class with GV-specific methods and variables. Finally, the gvArray value object is wrapped in a gvArrayRef handle object. This enables flexibility in passing the data object around and modifying without copying it. Finally, this data object is abstracted from the user's point of view as a *hypercube* multi-dimensional data object.

DynaSim Integration

GV works seamlessly with DynaSim. Since the raw DS datasets can be terabytes in size, the preferred workflow for visualization involves two branches of compressing the data into a useful form.

The first involves pre-computing a scalar numeric or categorical value for each simulation from DS analysis functions. Thus, the data from each single simulation with potentially hundreds of dimensions is compressed into a set of scalars. GV automatically imports the analysis result values into a GV hypercube, storing the relevant
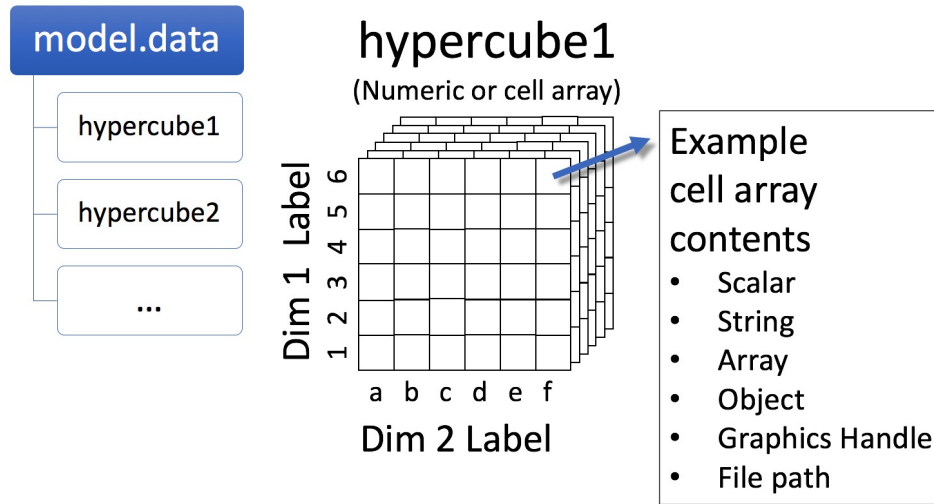
Figure 4·3: Data model

metadata. The analysis functions themselves along with the simulation number become values on a prepended datatype dimension called "analysisFn" by default (dimension 1 in Figure 4·9). There are then viewed in the *Plot Window Plugin* window, as detailed in section 4.3.4.

A second way to compress the data is to pre-compute plots of different types indexed to simulation number. These are viewed in the *Image Window Plugin* window, and are dynamically changed by highlighting points in the *Plot Window Plugin* window corresponding to each simulation (described in section 4.3.4).

A third option is to load the raw simulation data and call plotting functions from within GV. This makes use of the *dsPlot Window Plugin* discussed in section 4.3.4.

Importing Data

There are several ways to import data into GV using the Matlab command window (listing 4.3).

Listing 4.3: Importing data into GV using the Matlab command window

```
% src can be a dataVariable in workspace or the path to
    a data file
```

```
src = dataVariable;
% or
src = fullfile('path','to','file');

% Import data using class call
gv(src);
gv.Load(src);

% Import data into existing object
gvObj = gv();
gvObj.load(src);
```

There are also a several ways using the GV toolbar menus found in the main window. From the *File* menu, there are automatic import options and manual ones. The automatic ones search for a mat data file in the current working directory and either load the *gvArray* object or import the Matlab array. The manual ones open a loading window for selection of a file to import. From the *Model* menu, there is an option to import data from the workspace, which brings up a selection box from which one can choose one or more workspace variables to import into GV.

For DynaSim users, a quick way to automatically import DS data is to run GV (using an option from listing 4.2, e.g. `gv`) starting from inside of a DS study directory (containing the studyinfo.mat file)—the data is automatically imported and a GV-specific data file is saved for faster reloading in future calls.

4.3.4 Plugins

Main Window Plugin

The main window plugin provides the core GIMBL-Vis interface. As shown in Figure 4·4, the window features a top toolbar with dropdown menus to access different methods. Below this are tabs for each of the actively loaded plugins. Next is a data panel for changing the active hypercube if multiple ones have been imported. Lastly

is a scrollable panel of all plugins found in the "plugins" directory.
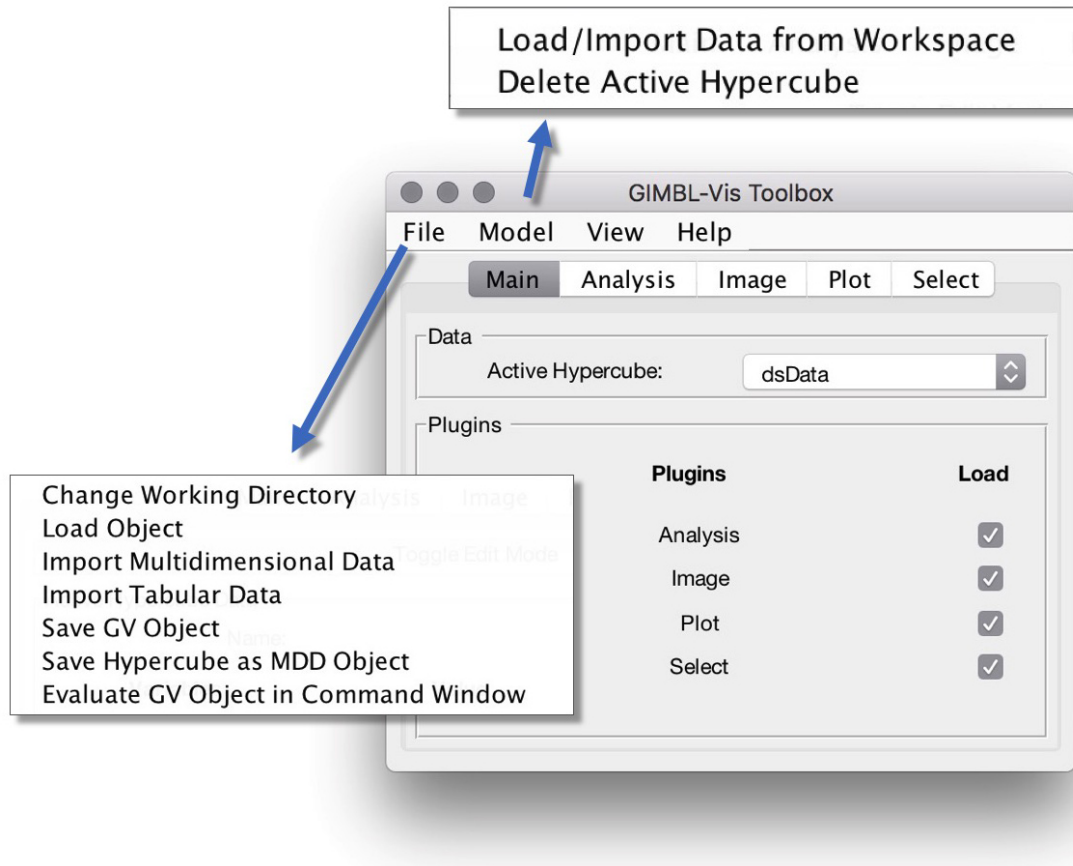
Figure 4·4: Main Window

Plot Window Plugin

The current set of plugins implement three methods of visualization. The first is the *Plot Window Plugin*, a meta plot of scalar functionals for every simulation (Figure 4·5). A typical functional is the average firing rate or the peak spectral power. The number of visible dimensions can be set from 1-8, with >3D selections showing 2D and 3D projections of the hypercube as subplots in the figure window. Using the select plugin (Figure 4·9), one may use the mouse wheel to scroll through the 2D and 3D slices of the dataset to reveal the effects of varying specific parameters.

There are multiple view types for 1D, 2D, and 3D panels. These options can be
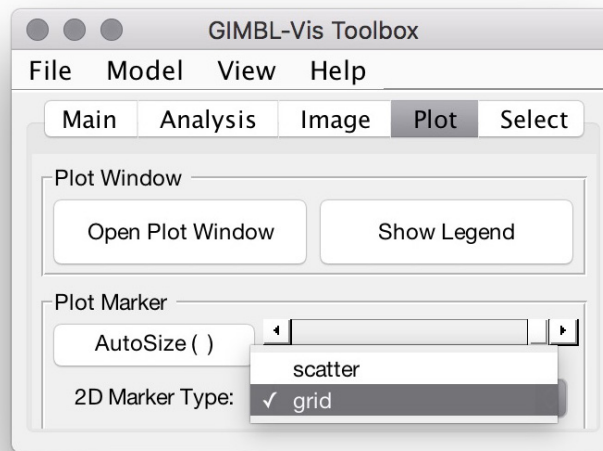
Figure 4·5: Plot Panel

changed in the plot panel of the main window, or with the shortcut keys 1, 2, and 3, respectively. For a 1D slice, options include a line plot with the y-axis representing the value of the scalar, and a linear point plot with the value encoded in the point color. For 2D slices, a point plot or color grid plot (like *imagesc* or *pcolor*) is available. For 3D, there is a point plot (i.e., *plot3* function) or a view with three orthogonal slices (i.e., *slice* function).

Image Window Plugin

The second visualization is found in the *Image Window Plugin* (Figure 4·6). This permits visualization of pre-created images from the simulations, by using the mouse to highlight points in the plot window. For example, one may make images of the voltage trace and spectral power during each simulation. Using image files is faster than loading the data and consumes far less storage space. Thus, 1 terabyte of simulation data could be compressed into a few 100 megabytes of metadata and images for rapid visualization.
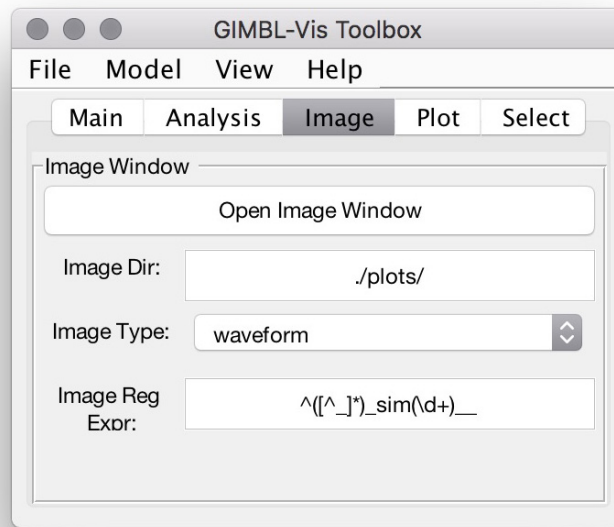
Figure 4·6: Image Panel

dsPlot Window Plugin

The third visualization requires access to the original simulation data. In this *dsPlot Window Plugin* 4·7, one may click on the points in the plot window to load the data and apply any plotting function to the data. This is slower than using the image window but allows for post hoc visualization and the use of Matlab figure tools.

Analysis Plugin

The *Analysis Plugin* is the first mentioned that is not associated with a separate window, although it does have its own panel in the main window (Figure 4·8). It enables one to apply a function to the data of a given hypercube. The output can be merged back into the source hypercube, stored as a new hypercube, stored as as workspace variable, or saved to a new mat file. Since GIMBL-Vis has been used mainly for visualization so far, the analysis plugin is the first of its kind, and demonstrates what is possible with the flexibly extensible GV core.
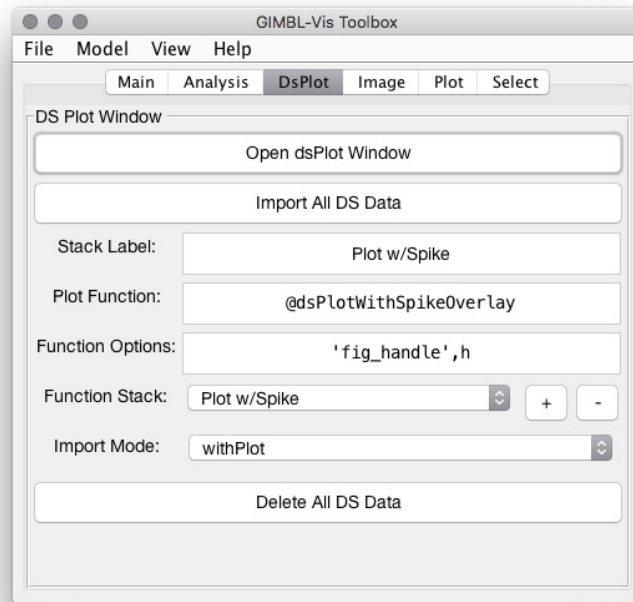
Figure 4·7: dsPlot Panel

4.3.5 Advantages and Disadvantages

Advantages

- Free, open-source toolbox with an extensible plugin architecture for development by the community

- Visualize >3D data while maintaining the original dimensions

- Works with mixed types of data, including numeric and categorical

- Different view types for 1D, 2D, and 3D slices

- Configuration file for customizing the user experience

Disadvantages

- Runs within Matlab only
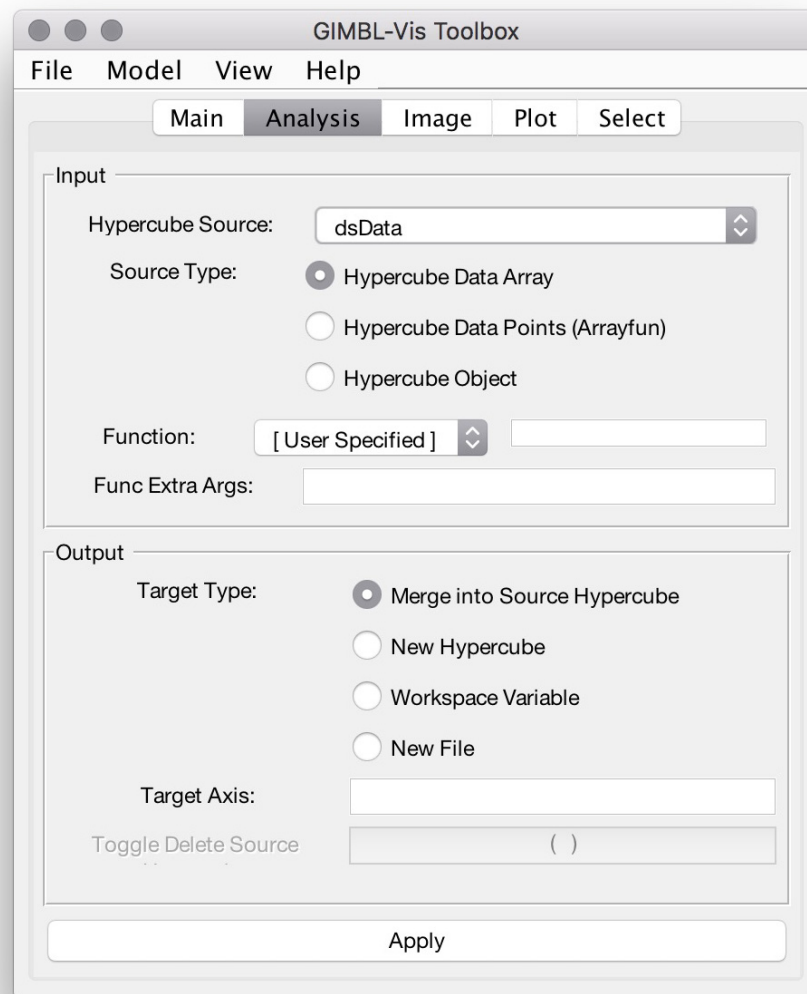
Figure 4·8: Analysis Panel

- *Plot Window Plugin* optimized for use with compressions of time series data, i.e. images and scalar functions of the original data

- No plugin yet for microscopy or medical data

4.4 Usage Example

4.4.1 Simulating a Simple Model with DynaSim and Running GIMBL-Vis

To demonstrate the power of the DynaSim + GIMBL-Vis workflow, what follows is the code and relevant snapshots from the workflow to simulate a single Izhikevich spiking neuron model. As Izhikevich writes, the model "reproduces spiking and bursting behavior of known types of cortical neurons...[and] combines the biologically plausibility of Hodgkin-Huxley-type dynamics and the computational efficiency of integrate-and-fire neurons" (Izhikevich, 2003). The code to simulate the model in DS, start GV, and import the data follows in listing listing 4.4.

Listing 4.4: Simulating and visualizing 5D data from 1125 simulations of an Izhikevich neuron

```
%--Simulate using DynaSim--
% simulation time limits
options.time_limits = [0 2e3]; % ms, [beg end]

% simulate on supercomputer
options.cluster_flag = 1;

% choose directory to save simulation results
options.study_dir = 'Izh_sims';

% instantiate model structure
s = struct();

% add applied current and noise
s.populations.mechanism_list = {'stim', 'noise'};
```

```
% add parameter ranges to vary over
P='pop1'; % default name of population
options.vary={
    {P, 'I', linspace( -65,   80, 5)};
    {P, 'a', linspace(-.026, .03, 5)};
    {P, 'b', linspace(   -1, 1.5, 5)};
    {P, 'c', linspace(  -65, -45, 3)};
    {P, 'd', linspace(    0,   8, 3)};
  };

% Known Parameters for Behaviors:
%   tonic bursting
%     {'a', .02; 'b', .2; 'c',-50; 'd',2;  'I', 15}
%   spike frequency adaptation
%     {'a', .01; 'b', .2; 'c',-65; 'd',8;  'I', 30}
%   spike latency
%     {'a', .02; 'b', .2; 'c',-65; 'd',6;  'I',  7}
%   rebound burst
%     {'a', .03; 'b',.25; 'c',-52; 'd',0;  'I',  0}
%   bistability
%     {'a',   1; 'b',1.5; 'c',-60; 'd',0;  'I',-65}
%   accomodation
%     {'a', .02; 'b',  1; 'c',-55; 'd',4;  'I',  1}
%   inhibition-induced spiking
%     {'a', -.02;'b',- 1; 'c',-60; 'd',8;  'I', 80}
%   inhibition-induced bursting
%     {'a',-.026;'b', -1; 'c',-45; 'd',0;  'I', 70}

% define plot and analysis functions
options.plot_functions = {@dsPlot}; % voltage plot
options.analysis_functions = {dsResult_muaFR}; %
   calculate average firing rate for entire simulate

% use predefined Izhikevich neuron model
```

```
%    (part of DS model library)
s.populations.equations = 'Izh';
s.populations.parameters = {'stim_amp', 200,
                            'noise_amp',2e4};

dsPlot(dsSimulate(s, options);

%--Visualize using GIMBL-Vis--
% change working directory to simulation study directory
cd( options.study_dir );

% run GV application
gvr(src);
```

4.4.2   Using GIMBL-Vis to View the Simulation Data

After running that code, the main GV window appears. The corresponding select panel is shown in Figure 4·9. The first dimension shows that the firing rate analysis function results will be viewed. Clicking the view checkboxes chooses which dimensions will be represented in the plot window (top of Figure 4·10). By checking all 5 viewable dimensions to plot, the plot window creates subplots for each 2D and 3D slice of the data. The slice view can be changed dynamically by moving the sliders or entering a value in the value box.

Moving the mouse over the plot points for different simulations triggers the corresponding simulation's voltage trace image to appear in the image window (bottom half of Figure 4·10).

4.5   Conclusion

While Eve Marder's work with high-dimensional parameter sweeps of models (introduced in section 4.2.2) has highlighted the need to explore different model parame-
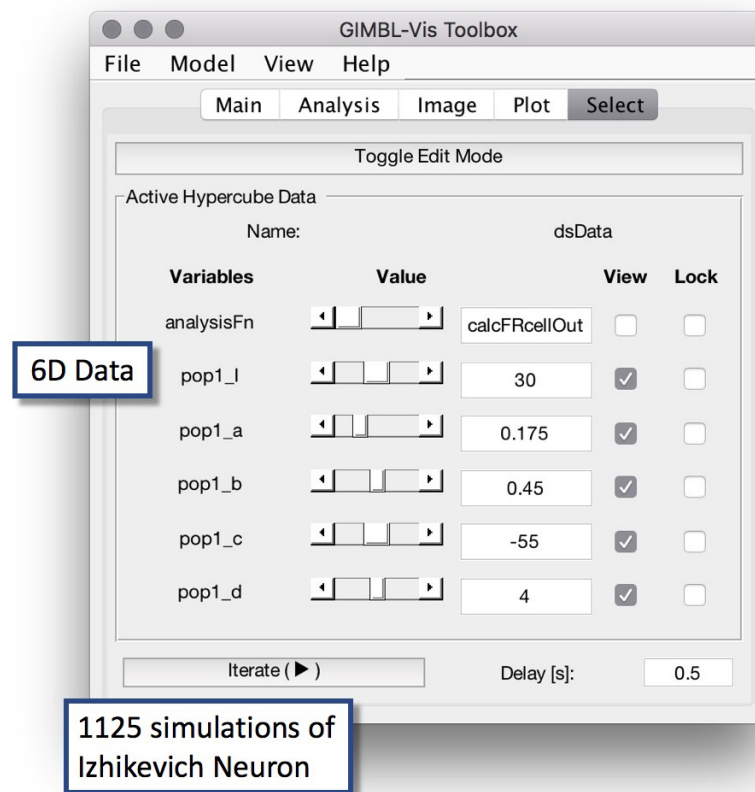
Figure 4·9: Select Panel
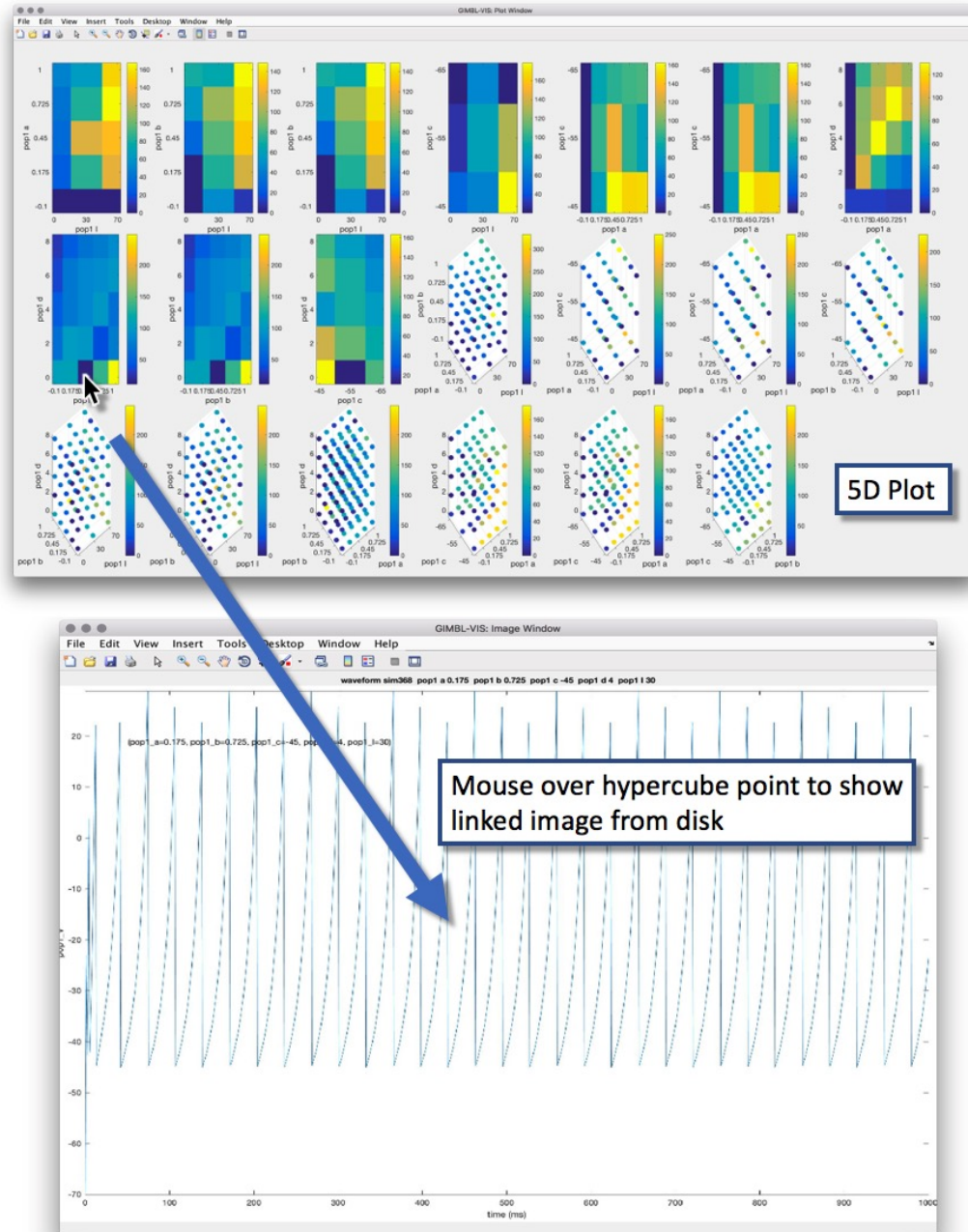
Figure 4·10: Example dataset in GV. The top *dsPlot window* plots the average firing rate of each simulation in 2D and 3D slices of 5D parameter space for 1125 different parameterizations of an Izhikevich neuron. The bottom *image window* shows pre-created voltage trace images for each simulation, by mousing over the corresponding point in the *dsPlot window*.

terizations, until now there did exist an efficacious tool for interpreting the results of such explorations, especially in Matlab.

GIMBL-Vis provides a unique Matlab solution to the problem of visualizing and analyzing multi-dimensional data. Importantly, it provides an extensible open platform for distributed development by the community, in order to adapt to future needs.

4.5.1 Future Directions

There are nearly endless potential extensions for GIMBL-Vis. It features a flexible core structure for building GUI apps. The best direction for future development is whatever the current needs of the users are.

For visualization, the next feature to create is a multi-panel image window plugin. This would be similar to the current *Image Window Plugin*, but would enable the tiling of multiple pre-generated images to be viewed simultaneously while surfing through the simulations in the plot window. For example, the voltage trace, an ion channel time-series, spike rastergram, and power spectrogram could be viewed simultaneously.

From the analysis perspective, an important next step is to create an explicit dimensionality reduction plugin that facilitates using the built-in Matlab functions. It would also be interesting to connect GV with the DataHigh toolbox (Cowley et al., 2013), that embeds neural population activity into lower-dimensional spaces.

Chapter 5

Conclusions

Here, the concept of local neuromodulation exerting a powerful influence on global cortical rhythms is explored through two projects, one experimental and one computational. While empiricism is the cornerstone of modern science, experimental investigations often yield surprising or unexpected results with unclear mechanisms. Biophysical computational model can provide desirable explanatory power for these elusive mechanisms. Thus, an effective way to study scientific problems is to use an collaborative dual process of empirical studies and computational models informing one another with their complementary strengths. Both investigations described here followed this process. However, as the problems investigated by these methods continue to increase in complexity and technology enables larger datasets, the problem of visualization and analysis of data to make conclusions becomes ever more difficult. Hence, the final work discussed is the creation of a Matlab tool for visualizing and analyzing such multi-dimensional datasets.

Appendix A

Model Specification

A.1 Spiking Model

Single compartment conductance-based Hodgkin-Huxley-type point neuron models were used with a typical equation structure as follows.

Voltage changes over time were calculated using the following standard cable equation:

$C_m \frac{dV}{dt} = -\sum(I_{int} + I_{syn}) + \mathcal{N}(I_{app}, I_{std}^2)$, in which C_m is the membrane capacitance, I_{int} are the intrinsic ionic currents, I_{syn} are the synaptic currents, I_{app} is the mean applied current, and I_{std} is the standard deviation of the gaussian current noise.

Most membrane and synaptic currents used a Hodgkin-Huxley-type conductance: $I = \bar{g}m^n h^k(V - E_{rev})$, in which $\bar{g}$ is the maximal conductance, m and h are different gates (fraction of channels open), and E_{rev} is the reversal potential.

Each of the gates evolved in time according to one of three forms: $\frac{dm}{dt} = \frac{1-m}{\tau_r} - \frac{m}{\tau_d} = \frac{m_\infty(V)-m}{\tau_m} = \alpha_m(V)(1 - m) - \beta_m(V)m$

In the full thalamocortical model, E→TC and E→TRN synapses during NREM2 were silenced to reduce synchronization, permitting anti-synchronous alpha frequencies. This merely impacts frequency, not timing.

A.1.1 Spiking Model Equations

Cells	Scope	Equation
[TC & TRN]	Na	$iNa = gNa * mNa^3 * hNa * (V - ENa)$
"	"	$\alpha_m = .32 * (13 - (V + Vshift))/(exp((13 - (V + Vshift))/4) - 1)$
"	"	$\beta_m = .28 * ((V + Vshift) - 40)/(exp(((V + Vshift) - 40)/5) - 1)$
"	"	$\alpha_h = .128 * exp((17 - (V + Vshift))/18)$
"	"	$\beta_h = 4/(1 + exp((40 - (V + Vshift))/5))$
"	K	$iK = gK * nK^4 * (V - EK)$
"	"	$\alpha_n(V) = 0.032 * (15 - (V + Vshift))/(exp((15 - (V + Vshift))/5) - 1)$
"	"	$\beta_n(V) = 0.5 * exp((10 - (V + Vshift))/40)$
"	CaBuffer	$CaBuffer' = max(((-10 * iT(t))/(2 * 96485.3)), 0) - (CaBuffer - 0.00024)/5$
"	Leak	$iLeak = -gLeak * (V - ELeak)$
"	Pois	$iPois = -gPois * s * (V - Epois)$
"	"	$s(t + 1) := s(t) * Pois(\lambda) * exp(-dt/tauPois)$
TC	T	$iT = gT * Minf(V)^2 * hT * (V - ET(V))$
"	"	$hT' = (Hinf(V) - hT)/tauH(V)$
"	"	$ET(V) = 1000 * (8.31441 * 309.15)/(2 * 96485.3) * log(2/CaBuffer(t))$
"	"	$Minf(V) = 1/(1 + exp((-(V + 57 + Vshift))/6.2))$
"	"	$Hinf(V) = 1/(1 + exp((V + 81 + Vshift)/4))$
"	"	$tauH(V) = (30.8 + (211.4 + exp((V + 113.2 + Vshift)/5))/(1 + exp((V + 84 + Vshift)/3.2))))/3.737$
"	H	$iH = gH * (OPENone + caCoop * OpenCaLocked + campMult1 * campModNorm1(V) + campMult2 * campModNorm2(V) + campMult3 * campModNorm3(V)) * (V - EH)$
"	"	$OPENone' = k4 * OpenCaLocked - k3 * (Pca/Pc) * OPENone - \beta_h(V) * OPENone + \alpha_h(V) * Cone$
"	"	$OpenCaLocked = 1 - Cone - OPENone$
"	"	$Cone' = \beta_h(V) * OPENone - \alpha_h(V) * Cone$
"	"	$Pzero' = k2 * Pca - k1 * ((CaBuffer(t)/cac)^nCa) * Pzero$
"	"	$Pca = 1 - Pzero$

Cells	Scope	Equation
''	''	$\alpha_h(V) = Hinf(V)/tauH(V)$
''	''	$\beta_h(V) = (1 - Hinf(V))/tauH(V)$
''	''	$tauH(V) = tauMin + 1000/(exp((V+71.5)/14.2) + exp((-(V+89))/11.6))$
''	''	$Hinf(V) = 1/(1 + exp((V+75)/5.5))$
''	''	$campModNorm1(t) = campGate1(t)/campScale$
''	''	$campModNorm2(t) = campGate2(t)/campScale$
''	''	$campModNorm3(t) = campGate3(t)/campScale$
''	cAMP	$camp1' = remBool(t) * sVIP * (1 - camp1)/tauCAMP1 - camp1/(tauCAMP1 * (1 - (sVIP < 1e - 4) * tauCAMP1PropReduce))$
''	''	$camp2' = remBool(t) * sVIP * (1 - camp2)/(tauCAMP2 - remBool(t) * tauCAMP2RemPropReduce * tauCAMP2) - camp2/(tauCAMP2 - remBool(t) * tauCAMP2RemPropReduce * tauCAMP2)$
''	''	$camp3' = remBool(t) * sVIP * (1 - camp3)/tauCAMP3 - camp3/tauCAMP3$
''	''	$campGate1 = (2 * camp1 * netcon)/scalingFactor$
''	''	$campGate2 = (2 * camp2 * netcon)/scalingFactor$
''	''	$campGate3 = (2 * camp3 * netcon)/scalingFactor$
TRN	T_{slow}	$iTslow = gT * mT^2 * hT * (V - ET(V))$
''	''	$mT' = (Minf(V) - mT)/tauM(V)$
''	''	$hT' = (Hinf(V) - hT)/tauH(V)$
''	''	$Minf(V) = 1/(1 + exp(-(V + 50 + Vshift)/7.4))$
''	''	$tauM(V) = (0.999 + (0.333/(exp((V + 25 + Vshift)/10) + exp(-(V + 100 + Vshift)/15))))$
''	''	$Hinf(V) = 1/(1 + exp((V + 78 + Vshift)/5))$
''	''	$tauH(V) = (28.307 + (0.333/(exp((V + 46 + Vshift)/4) + exp(-(V + 405 + Vshift)/50))))$
''	''	$ET(V) = 1000 * (8.31441 * 309.15)/(2 * 96485.3) * log(2/CaBuffer(t))$
E&I	Na	$iNa = -gNa * m^3 * h * (X - ENa)$
''	''	$m' = 0.32 * (V + 54)/(1 - exp(-(V + 54)/4)) * (1 - m) - 0.28 * (V + 27)/(exp((V + 27)/5) - 1) * m$

Cells	Scope	Equation
"	"	$h' = 0.128 * exp(-(V + 50)/18) * (1 - h) - 4/(1 + exp(-(V + 27)/5)) * h$
"	K	$iK = -gK * n^4 * (V - EK)$
"	"	$n' = 0.032 * (V + 52)/(1 - exp(-(V + 52)/5)) * (1 - n) - 0.5 * exp(-(V + 57)/40) * n$
"	Leak	$ILeak = -gLeak * (V - ELeak)$
E	M	$w' = (Q10 * 0.0001 * (V - Vhalf)/(1 - exp(-(V - Vhalf)/9))) * (1 - w) + Q10 * 0.0001 * (V - Vhalf)/(1 - exp((V - Vhalf)/9)) * w$
Syn	Any	$scalingFactor = max(sum(netcon, 1), 1)$
"	"	$netcon = rand(Npre, Npost) <= prob_c xn$
"	AMPA	$iAMPA = gAMPA/scalingFactor * (s * netcon) * (Vpost - EAMPA)$
"	"	$s' = (1 + tanh(Vpre/4)) * (1 - s)/2/tauRAMPA - s/tauDAMPA$
"	GABAa	$iGABA_A = spm * gGABAA/scalingFactor * (s * netcon) * (V - EGABAA)$
"	"	$s' = (1 + tanh(Vpre/4))/2 * (1 - s)/tauRGABAA - s/(tauDGABAA * spm)$
"	GABAb	$iGABA_B = gGABAB/scalingFactor * ((gg^4/(gg^4 + Kd)) * netcon) * (V - EGABAB)$
"	"	$r' = (1 + tanh(V_p re/4))/2 * (1 - r)/rTauRGABAB - r/rTauDGABAB$
"	"	$gg' = r/gTauRGABAB - gg/gTauDGABAB$
"	VIP	$sVIP' = (1 + tanh(Vpre/4)) * (1 - sVIP)/2/tauRvip - sVIP/tauDvip$
Misc	[spindle Timer]	$spindleTimer' = remBool(t) * (-spindleTimer) * timerKineticMult + spindleAccumBool * (1 - spindleTimer)/tauTimerD$
"	[rem Timer]	$remTimer' = remBool(t) * (-remTimer/tauRemD) + remBool(t) * (1 - remTimer) * remKineticMult$
"	[spindle InitBool]	spindleInitBool := remBool(t) && (t - tLastRemStart) > 5e3 && (allTcVoltagesLast500ms > modeThresh) && noTcSpikesInLast500ms && (remTimer(t) > .9)

Cells	Scope	Equation
"	[spindle Accum Bool]	spindleAccumulateBool := (spindleInitiateBool || spindleAccumulateBool) && !remBool(t)
"	remBool	$remBool := spindleTimer(t) > 0.9$

Table A.1: Spiking Model Equations

A.1.2 Spiking Model Parameters

Cells	Scope	Param	Value	Unit
TC	Cell	I_app	0	$\mu A/cm^2$
"	"	I_app_REM	5	$\mu A/cm^2$
"	"	I_std	1.5	$\mu A/cm^2$
"	"	V_0	-75	mV
"	"	V_0_std	0	mV
"	"	C_m	1	$\mu F/cm^2$
"	Na	gNa	90	mS/cm^2
"	"	ENa	50	mV
"	"	Vshift	25	mV
"	K	gK	10	mS/cm^2
"	"	EK	-100	mV
"	"	Vshift	25	mV
"	T	gT	2	mS/cm^2
"	"	Vshift	2	mV
"	H	gH	0.05	mS/cm^2
"	"	EH	-40	mV
"	"	nCa	4	none
"	"	caCoop	2	none
"	"	cac	0.002	mM
"	"	k1	0.002	ms^{-1}
"	"	k2	0.002	ms^{-1}
"	"	k3	0.003	$ms^{-1} * mM^{-1}$
"	"	k4	0.003	ms^{-1}
"	"	Pc	0.01	none
"	"	tauMin	20	ms
"	"	campMult1	0.5	none
"	"	campMult2	0.64444	none
"	"	campMult3	3.5556	none
"	"	campScale	0.25	none
"	cAMP	tauCAMP1	1000	ms

Cells	Scope	Param	Value	Unit
”	”	tauCAMP2	10000	ms
”	”	tauCAMP3	60000	ms
”	”	tauCAMP1PropRed	0.50	none
”	”	tauCAMP2RemPropRed	0.99	none
”	Leak	gLeak	0.02	mS/cm^2
”	”	Eleak	-85	mV
”	CaBuffer	CaBuffer_0	0.00024	mM
TRN	Cell	I_app	0	$\mu A/cm^2$
”	”	I_app_REM	5	$\mu A/cm^2$
”	”	I_std	2	$\mu A/cm^2$
”	”	V_0	-90	mV
”	”	V_0_std	0	mV
”	Na	gNa	200	mS/cm^2
”	”	ENa	50	mV
”	”	Vshift	55	mV
”	K	gK	20	mS/cm^2
”	”	EK	-100	mV
”	”	Vshift	55	mV
”	Tslow	gT	3	mS/cm^2
”	”	Vshift	2	mV
”	Leak	gLeak	0.05	mS/cm^2
”	”	Eleak	-90	mV
”	Ca_buffer	CaBuffer_0	0.00024	mM
E	Cell	I_app	0	$\mu A/cm^2$
”	”	I_std	4	$\mu A/cm^2$
”	”	V_0	-71	mV
”	”	V_0_std	2	mV
”	Na	gNa	100	mS/cm^2
”	”	ENa	50	mV
”	K	gK	80	mS/cm^2
”	”	EK	-100	mV
”	M	gM	1.3	mS/cm^2
”	”	EK	-100	mV
”	”	Q10	3.209	none
”	”	V_half	-30	mV
”	”	w_0	0.025	none
”	Leak	gLeak	0.1	mS/cm^2
”	”	Eleak	-67	mV
I	Cell	I_app	0	$\mu A/cm^2$
”	”	I_std	2	$\mu A/cm^2$
”	”	V_0	-67	mV

Cells	Scope	Param	Value	Unit
"	"	V_0_std	2	mV
"	Na	gNa	100	mS/cm^2
"	"	ENa	50	mV
"	K	gK	80	mS/cm^2
"	"	EK	-100	mV
"	Leak	gLeak	0.1	mS/cm^2
"	"	Eleak	-67	mV
TC & TRN	Pois	gPois	0.7	mS/cm^2
"	"	λ	0.8	none
"	"	Epois	0	mV
"	"	tauPois	2	ms
Any	AMPA	EAMPA	1	mV
"	"	tauRAMPA	0.1	ms
"	"	tauDAMPA	2	ms
"	GABAa	EGABAA	1	mV
"	"	tauRGABAA	0.25	ms
"	"	tauDGABAA	5	ms
"	GABAb	EGABAB	-95	mV
"	"	Kd	100	μm^4
"	"	rTauRGABAB	2	ms
"	"	rTauDGABAB	833	ms
"	"	gTauRGABAB	5.5556	ms
"	"	gTauDGABAB	29.4118	ms
TC→TRN	AMPA	gAMPA	1.4022	mS/cm^2
TRN→TC	GABAa	gGABAA	0.0691	mS/cm^2
"	GABAb	gGABAB	0.012	mS/cm^2
"	VIP	tauRvip	1	ms
"	"	tauDvip	5	ms
TRN→TRN	GABAa	gGABAA	1.4022	mS/cm^2
TC→E	AMPA	gAMPA	0.2	mS/cm^2
E→TC	AMPA	gAMPA	0.2	mS/cm^2
E→TRN	AMPA	gAMPA	0.2	mS/cm^2
E→I	AMPA	gAMPA	0.1	mS/cm^2
I→E	GABAa	gGABAA	0.1	mS/cm^2
E→E	AMPA	gAMPA	0.1	mS/cm^2
Misc	spindleTimer	tauTimerD	5000	ms
"	"	timerKineticMult	5	none
"	remTimer	tauRemD	1000	ms
"	"	tauRemMult	3	none
"	"	modeThresh	-76	mV

Cells	Scope	Param	Value	Unit
"	"	remKineticMult	5	none

Table A.2: Spiking Model Parameters

A.2 Simplified Non-Spiking Model

A simplified non-spiking model was used to demonstrate the utility of the two slower VIP timescales for shaping sleep architecture using the hours-long biological timescale as the model timescale. This model is based on the thalamic module of the full spiking model, but with slower time constants to match the correct timescales for an $\approx$8 hour human night's sleep.

A.2.1 Non-Spiking Model Equations

Scope	Equation
V	$V' = (iLeak(V) + iH(V)) * 3.6e5$
Leak	$iLeak = -gLeak * (V - ELeak)$
H	$iH = -gH * gHmod * Hinf * (V - EH)$
"	$gHmod = min(campSlowMult * campSlowGate + campMult * campGate + achGate * achMult, .8)$
"	$Hinf = 1./(1 + exp((V + 75)./5.5))$
"	$campGate = (camp/maxCAMP)^nCamp$
"	$campSlowGate = (campSlow/maxCAMP)$
cAMP	$camp' = remBool * burstVipAvgS. * (1 - camp)./tauCamp - camp./tauCamp$
	$campSlow' = remBool * burstVipAvgS. * (1 - campSlow)./tauCampSlow - campSlow./tauCampSlow$
	$maxCAMP = burstVipAvgS/(1 + burstVipAvgS)$
ACh	$ach' = (remBool). * (1 - aCh)./tauACh - aCh./tauACh$
"	$achGate = adenoMult * aCh/maxAch$
Adenosine	$adenoMult = (adeno + .65)/1.65$
"	$adeno = (tFinal - t)/tFinal$
REM	$remTimer' = remBool * (-remTimer/tauRemD) + remBool * (1 - remTimer) * 5$

Scope	Equation
"	$tauRemD = tauRemDRange(1) + sign(diff(tauRemDRange)) * (1 - adeno) * range(tauRemDRange)$
"	remBool = (t - tLastRemStart) > 30/60 && burstModeBool && remTimer > .9
"	$burstModeBool = (V <= modeThresh)$

Table A.3: Non-Spiking Model Equations

A.2.2 Non-Spiking Model Parameters

Scope	Parameter	Value	Unit
Leak	gLeak	0.01	mS/cm^2
"	Eleak	-90	mV
H	gH	0.01	mS/cm^2
"	EH	-40	mV
cAMP	tauCamp	40/60	hours
"	campMult	1	none
"	burstVipAvgS	0.15	none
"	nCamp	4	none
"	campSlowMult	1	none
"	tauCampSlow	8	hours
ACh	achMult	0.5	none
"	maxAch	0.5	none
"	tauACh	10/60	hours
Adenosine	tFinal	8	hours
REM	tauRemDRange	[10 50]/60	hours
"	modeThresh	-76	mV

Table A.4: Non-Spiking Model Parameters

References

Achermann, P. and Borbély, A. A. (1997). Low-frequency (<1 Hz) oscillations in the human sleep electroencephalogram. *Neuroscience*, 81(1):213–222. [Cited on page 101]

Akeju, O. and Brown, E. N. (2017). Neural oscillations demonstrate that general anesthesia and sedative states are neurophysiologically distinct from sleep. *Current opinion in neurobiology*, 44:178–185. [Cited on page 64]

Alkire, M. T., Asher, C. D., Franciscus, A. M., and Hahn, E. L. (2009). Thalamic microinfusion of antibody to a voltage-gated potassium channel restores consciousness during anesthesia. *Anesthesiology*, 110(4):766–773. [Cited on page 65]

Alkire, M. T., Haier, R. J., and Fallon, J. H. (2000). Toward a Unified Theory of Narcosis: Brain Imaging Evidence for a Thalamocortical Switch as the Neurophysiologic Basis of Anesthetic-Induced Unconsciousness. *Consciousness and Cognition*, 9(3):370–386. [Cited on page 104]

Alkire, M. T., McReynolds, J. R., Hahn, E. L., and Trivedi, A. N. (2007). Thalamic microinjection of nicotine reverses sevoflurane-induced loss of righting reflex in the rat. *Anesthesiology*, 107(2):264–272. [Cited on page 65]

Amzica, F. and Steriade, M. (1998). Electrophysiological correlates of sleep delta waves. *Electroencephalography and clinical neurophysiology*, 107(2):69–83. [Cited on page 110]

Arinsburg, S. S., Cohen, I. S., and Yu, H.-G. (2006). Constitutively active Src tyrosine kinase changes gating of HCN4 channels through direct binding to the channel proteins. *Journal of Cardiovascular Pharmacology*, 47(4):578–586. [Cited on page 51]

Baker, R., Gent, T. C., Yang, Q., Parker, S., Vyssotski, A. L., Wisden, W., Brickley, S. G., and Franks, N. P. (2014). Altered Activity in the Central Medial Thalamus Precedes Changes in the Neocortex during Transitions into Both Sleep and Propofol Anesthesia. *The Journal of neuroscience*, 34(40):13326–13335. [Cited on pages 64, 65, 67, and 115]

Bal, T., von Krosigk, M., and McCormick, D. A. (1995). Synaptic and membrane mechanisms underlying synchronized oscillations in the ferret lateral geniculate nucleus in vitro. *The Journal of physiology*, 483 (Pt 3):641–663. [Cited on page 78]

Bar-Gad, I., Elias, S., Vaadia, E., and Bergman, H. (2004). Complex locking rather than complete cessation of neuronal activity in the globus pallidus of a 1-methyl-4-phenyl-1,2,3,6-tetrahydropyridine-treated primate in response to pallidal microstimulation. *Journal of Neuroscience*, 24(33):7410–7419. [Cited on pages 38 and 39]

Bartho, P., Freund, T. F., and Acsady, L. (2002). Selective GABAergic innervation of thalamic nuclei from zona incerta. *European Journal of Neuroscience*, 16(6):999–1014. [Cited on page 109]

Bartho, P., Slézia, A., Matyas, F., Faradzs-Zade, L., Ulbert, I., Harris, K. D., and Acsady, L. (2014). Ongoing Network State Controls the Length of Sleep Spindles via Inhibitory Activity. *Neuron*, 82(6):1367–1379. [Cited on pages 59, 96, and 97]

Bartolo, R. and Merchant, H. (2015). β oscillations are linked to the initiation of sensory-cued movement sequences and the internal guidance of regular tapping in the monkey. *Journal of Neuroscience*, 35(11):4635–4640. [Cited on page 11]

Bazhenov, M., Timofeev, I., and Steriade, M. (1999). Self–sustained rhythmic activity in the thalamic reticular nucleus mediated by depolarizing GABAA receptor potentials. *Nature neuroscience*. [Cited on page 119]

Bazhenov, M., Timofeev, I., Steriade, M., and Sejnowski, T. J. (2002). Model of thalamocortical slow-wave sleep oscillations and transitions to activated States. *Journal of Neuroscience*, 22(19):8691–8704. [Cited on pages 56 and 109]

Berke, J. D. (2009). Fast oscillations in cortical-striatal networks switch frequency following rewarding events and stimulant drugs. *European Journal of Neuroscience*, 30(5):848–859. [Cited on page 40]

Berke, J. D., Okatan, M., Skurski, J., and Eichenbaum, H. B. (2004). Oscillatory entrainment of striatal neurons in freely moving rats. *Neuron*, 43(6):883–896. [Cited on page 11]

Blum, I. D., Zhu, L., Moquin, L., Kokoeva, M. V., Gratton, A., Giros, B., and Storch, K.-F. (2014). A highly tunable dopaminergic oscillator generates ultradian rhythms of behavioral arousal. *eLife*, 3:27. [Cited on page 100]

Bokil, H., Andrews, P., Kulkarni, J. E., Mehta, S., and Mitra, P. P. (2010). Chronux: a platform for analyzing neural signals. *Journal of Neuroscience Methods*, 192(1):146–151.

[Cited on page 15]

Bonjean, M., Baker, T., Lemieux, M., Timofeev, I., Sejnowski, T., and Bazhenov, M. (2011). Corticothalamic Feedback Controls Sleep Spindle Duration In Vivo. *The Journal of neuroscience*, 31(25):9124–9134. [Cited on page 97]

Booth, V. and Diniz Behn, C. G. (2014). Physiologically-based modeling of sleep-wake regulatory networks. *Mathematical Biosciences*, 250:54–68. [Cited on pages 61, 63, and 109]

Borbély, A. A. (1982). A two process model of sleep regulation. *Human neurobiology*, 1(3):195–204. [Cited on page 63]

Borgers, C. (2017). An introduction to modeling neuronal dynamics. Cham: Springer International Publishing. [Cited on pages 84 and 99]

Bourgin, P., Lebrand, C., Escourrou, P., Gaultier, C., Franc, B., Hamon, M., and Adrien, J. (1997). Vasoactive intestinal polypeptide microinjections into the oral pontine tegmentum enhance rapid eye movement sleep in the rat. *Neuroscience*, 77(2):351–360. [Cited on pages 45 and 100]

Boyden, E. S., Zhang, F., Bamberg, E., Nagel, G., and Deisseroth, K. (2005). Millisecond-timescale, genetically targeted optical control of neural activity. *Nature neuroscience*, 8(9):1263–1268.

[Cited on page 3]

Brette, R., Rudolph, M., Carnevale, T., Hines, M., Beeman, D., Bower, J. M., Diesmann, M., Morrison, A., Goodman, P. H., Harris, F. C., Zirpe, M., Natschlager, T., Pecevski, D., Ermentrout, B., Djurfeldt, M., Lansner, A., Rochel, O., Vieville, T., Muller, E., Davison, A. P., El Boustani, S., and Destexhe, A. (2007). Simulation of networks of spiking neurons: a review of tools and strategies. *Journal of computational neuroscience*, 23(3):349–398. [Cited on page 122]

Brown, E. N., Lydic, R., and Schiff, N. D. (2010). General anesthesia, sleep, and coma. *New England Journal of Medicine*, 363(27):2638–2650. [Cited on pages 44, 64, and 106]

Brown, P. (2007). Abnormal oscillatory synchronisation in the motor system leads to impaired movement. *Current opinion in neurobiology*, 17(6):656–664. [Cited on pages 2, 6, 8, and 11]

Brown, P., Oliviero, A., Mazzone, P., Insola, A., Tonali, P., and Di Lazzaro, V. (2001). Dopamine dependency of oscillations between subthalamic nucleus and pallidum in Parkinson's disease. *Journal of Neuroscience*, 21(3):1033–1038. [Cited on pages 12 and 40]

Brown, P. and Williams, D. (2005). Basal ganglia local field potential activity: character and functional significance in the human. *Clinical neurophysiology*, 116(11):2510–2519. [Cited on page 11]

Budde, T., Biella, G., Munsch, T., and Pape, H. C. (1997). Lack of regulation by intracellular Ca2+ of the hyperpolarization-activated cation current in rat thalamic neurones. *The Journal of physiology*, 503 (Pt 1):79–85. [Cited on pages 46 and 57]

Burgunder, J. M., Heyberger, B., and Lauterburg, T. (1999). Thalamic reticular nucleus parcellation delineated by VIP and TRH gene expression in the rat. *Journal of chemical neuroanatomy*, 17(3):147–152. [Cited on pages 53, 54, and 110]

Buzsaki, G. (2006). Rhythms of the Brain. New York, NY: Oxford University Press. [Cited on page 1]

Buzsaki, G., Anastassiou, C. A., and Koch, C. (2012). The origin of extracellular fields and currents — EEG, ECoG, LFP and spikes. *Nature Reviews Neuroscience*, 13(6):407–420. [Cited on page 1]

Calebiro, D. and Maiellaro, I. (2014). cAMP signaling microdomains and their observation by optical methods. *Frontiers in Cellular Neuroscience*, 8:350. [Cited on pages 47 and 49]

Chen, K.-S., Xu, M., Zhang, Z., Chang, W.-C., Gaj, T., Schaffer, D. V., and Dan, Y. (2018). A Hypothalamic Switch for REM and Non-REM Sleep. *Neuron*, 97(5):1168–1176.e4. [Cited on page 61]

Ching, S., Cimenser, A., Purdon, P. L., Brown, E. N., and Kopell, N. J. (2010). Thalamocortical model for a propofol-induced α-rhythm associated with loss of consciousness. *Proceedings of the National Academy of Sciences of the United States of America*, 107(52):22665–22670. [Cited on pages 56, 64, 104, and 105]

Ching, S., Purdon, P. L., Vijayan, S., Kopell, N. J., and Brown, E. N. (2012). A neurophysiological-metabolic model for burst suppression. *Proceedings of the National Academy of Sciences of the United States of America*, 109(8):3095–3100. [Cited on page 64]

Ching, S. N. and Brown, E. N. (2014). Modeling the dynamical effects of anesthesia on brain circuits. *Current opinion in neurobiology*, 25, 116-122. [Cited on page 64]

Contreras, D., Destexhe, A., Sejnowski, T. J., and Steriade, M. (1997). Spatiotemporal patterns of spindle oscillations in cortex and thalamus. *The Journal of neuroscience*, 17(3):1179–1196. [Cited on pages 59, 67, and 98]

Costa, R. M., Lin, S.-C., Sotnikova, T. D., Cyr, M., Gainetdinov, R. R., Caron, M. G., and Nicolelis, M. A. L. (2006). Rapid alterations in corticostriatal ensemble coordination during acute dopamine-dependent motor dysfunction. *Neuron*, 52(2):359–369. [Cited on page 12]

Courtemanche, R., Fujii, N., and Graybiel, A. M. (2003). Synchronous, focally modulated beta-band oscillations characterize local field potential activity in the striatum of awake behaving monkeys. *Journal of Neuroscience*, 23(37):11741–11752. [Cited on page 11]

Cowley, B. R., Kaufman, M. T., Butler, Z. S., Churchland, M. M., Ryu, S. I., Shenoy, K. V., and Yu, B. M. (2013). DataHigh: graphical user interface for visualizing and interacting with high-dimensional neural activity. *Journal of Neural Engineering*, 10(6):066012–19. [Cited on page 143]

Crook, S. M., Ermentrout, G. B., Vanier, M. C., and Bower, J. M. (1997). The role of axonal delay in the synchronization of networks of coupled cortical oscillators. *Journal of computational neuroscience*, 4(2):161–172. [Cited on page 109]

Crunelli, V., David, F., Lorincz, M. L., and Hughes, S. W. (2015). The thalamocortical network as a single slow wave-generating unit. *Current opinion in neurobiology*, 31:72–80. [Cited on page 110]

Crunelli, V. and Hughes, S. W. (2009). The slow (¡1 Hz) rhythm of non-REM sleep: a dialogue between three cardinal oscillators. *Nature neuroscience*, 13(1):9–17. [Cited on page 110]

Cunningham, J. P. and Yu, B. M. (2014). Dimensionality reduction for large-scale neural recordings. *Nature neuroscience*, 17(11):1500–1509. [Cited on page 127]

David, F. and Schmiedt, J. T. (2014). Thalamus and Cortex: Inseparable Partners in Shaping Sleep Slow Waves? *The Journal of neuroscience*, 34(35):11517–11518. [Cited on page 110]

David, F., Schmiedt, J. T., Taylor, H. L., Orban, G., Di Giovanni, G., Uebele, V. N., Renger, J. J., Lambert, R. C., Leresche, N., and Crunelli, V. (2013). Essential Thalamic Contribution to Slow Waves of Natural Sleep. *The Journal of neuroscience*, 33(50):19599–19610. [Cited on page 110]

DeBoer, P., Heeringa, M. J., and Abercrombie, E. D. (1996). Spontaneous release of acetylcholine in striatum is preferentially regulated by inhibitory dopamine D2 receptors. *European journal of pharmacology*, 317(2-3):257–262. [Cited on page 12]

Deschenes, M., Madariaga-Domich, A., and Steriade, M. (1985). Dendrodendritic synapses in the cat reticularis thalami nucleus: a structural basis for thalamic spindle synchronization. *Brain research*, 334(1):165–168. [Cited on page 119]

Destexhe, A., Babloyantz, A., and Sejnowski, T. J. (1993a). Ionic mechanisms for intrinsic slow oscillations in thalamic relay neurons. *Biophysical Journal*, 65(4):1538–1552. [Cited on pages 56, 59, 69, 107, 108, and 114]

Destexhe, A., Bal, T., McCormick, D. A., and Sejnowski, T. J. (1996). Ionic mechanisms underlying synchronized oscillations and propagating waves in a model of ferret thalamic slices. *Journal of Neurophysiology*, 76(3):2049–2070. [Cited on pages 56, 58, 59, 66, 67, 69, 71, 78, 95, 97, 98, 104, 105, 114, 117, and 119]

Destexhe, A., Contreras, D., Sejnowski, T. J., and Steriade, M. (1994). Modeling the control of reticular thalamic oscillations by neuromodulators. *Neuroreport*, 5(17):2217. [Cited on page 45]

Destexhe, A., Contreras, D., and Steriade, M. (1998). Mechanisms underlying the synchronizing action of corticothalamic feedback through inhibition of thalamic relay cells. *Journal of Neurophysiology*, 79(2):999–1016. [Cited on pages 59, 66, 76, 79, 82, 95, 117, and 120]

Destexhe, A., McCormick, D. A., and Sejnowski, T. J. (1993b). A model for 8-10 Hz spindling in interconnected thalamic relay and reticularis neurons. *Biophysical Journal*, 65(6):2473–2477. [Cited on pages 56 and 59]

Destexhe, A. and Sejnowski, T. J. (2001). *Thalamocortical Assemblies. How Ion Channels, Single Neurons, and Large-scale Networks Organize Sleep Oscillations.* Oxford University Press, USA. [Cited on pages 57, 82, 114, 115, and 119]

Deumens, R., Blokland, A., and Prickaerts, J. (2002). Modeling Parkinson's disease in rats: an evaluation of 6-OHDA lesions of the nigrostriatal pathway. *Experimental Neurology*, 175(2):303–317. [Cited on page 42]

Devergnas, A., Pittard, D., Bliwise, D., and Wichmann, T. (2014). Relationship between oscillatory activity in the cortico-basal ganglia network and parkinsonism in MPTP-treated monkeys. *Neurobiology of disease*, 68:156–166. [Cited on page 35]

Dibia, V. (2018). Data2Vis: Automatic Generation of Data Visualizations Using Sequence-to-Sequence Recurrent Neural Networks. *arxiv.org*. Retrieved from https://arxiv.org/abs/1804.03126 [Cited on page 124]

Diesmann, M. and Rechnen, M. G. (2001). NEST: An environment for neural systems simulations. *Forschung und wisschenschaftliches Rechnen, Beitrage zum Heinz-Billing-Preis*, 58, 43-70. [Cited on page 122]

Ding, J., Guzman, J. N., Tkatch, T., Chen, S., Goldberg, J. A., Ebert, P. J., Levitt, P., Wilson, C. J., Hamm, H. E., and Surmeier, D. J. (2006). RGS4-dependent attenuation of M4 autoreceptor function in striatal cholinergic interneurons following dopamine depletion. *Nature neuroscience*, 9(6):832–842. [Cited on page 12]

Diniz Behn, C. G. and Booth, V. (2010). Simulating Microinjection Experiments in a Novel Model of the Rat Sleep-Wake Regulatory Network. *Journal of Neurophysiology*, 103(4):1937–1953. [Cited on page 63]

DiPilato, L. M., Cheng, X., and Zhang, J. (2004). Fluorescent indicators of cAMP and Epac activation reveal differential dynamics of cAMP signaling within discrete subcellular compartments. *Proceedings of the National Academy of Sciences of the United States of America*, 101(47):16513–16518. [Cited on page 47]

Domich, L., Oakson, G., and Steriade, M. (1986). Thalamic burst patterns in the naturally sleeping cat: a comparison between cortically projecting and reticularis neurones. *The Journal of physiology*, 379(1), 429-449. [Cited on page 117]

Dyachok, O., Isakov, Y., Sagetorp, J., and Tengholm, A. (2006). Oscillations of cyclic AMP in hormone-stimulated insulin-secreting β-cells. *Nature*, 439(7074):349–352. [Cited on page 47]

English, D. F., Ibanez-Sandoval, O., Stark, E., Tecuapetla, F., Buzsaki, G., Deisseroth, K., Tepper, J. M., and Koos, T. (2011). GABAergic circuits mediate the reinforcement-related signals of striatal cholinergic interneurons. *Nature neuroscience*, 15(1):123–130. [Cited on page 41]

Ermentrout, B. and Saunders, D. (2006). Phase resetting and coupling of noisy neural oscillators. *Journal of computational neuroscience*, 20(2):179–190. [Cited on page 89]

Ermentrout, B. and Terman, D. H. (2010). Foundations of mathematical neuroscience. New York, NY: Springer Science+Business Media. [Cited on page 96]

Ermentrout, G. B. and Kopell, N. (1998). Fine structure of neural spiking and synchronization in the presence of conduction delays. *Proceedings of the National Academy of Sciences of the United States of America*, 95(3):1259–1264. [Cited on page 109]

Fang, J., Payne, L., and Krueger, J. M. (1995). Pituitary adenylate cyclase activating polypeptide enhances rapid eye movement sleep in rats. *Brain research*, 686(1):23–28. [Cited on page 101]

Feingold, J., Gibson, D. J., DePasquale, B., and Graybiel, A. M. (2015). Bursts of beta oscillation differentiate postperformance activity in the striatum and motor cortex of monkeys performing movement tasks. *Proceedings of the National Academy of Sciences of the United States of America*, 112(44), 13687-13692. [Cited on pages 2 and 11]

Fogel, S. M., Smith, C. T., and Cote, K. A. (2007). Dissociable learning-dependent changes in REM and non-REM sleep in declarative and procedural memory systems. *Behavioural Brain Research*, 180(1):48–61. [Cited on page 59]

Fontanez, D. E. and Porter, J. T. (2006). Adenosine A1 receptors decrease thalamic excitation of inhibitory and excitatory neurons in the barrel cortex. *Neuroscience*, 137(4):1177–1184. [Cited on page 103]

Fox, S. H. (2013). Non-dopaminergic treatments for motor control in Parkinson's disease. *Drugs*, 73(13):1405–1415. [Cited on page 38]

Franks, N. P. (2008). General anaesthesia: from molecular targets to neuronal pathways of sleep and arousal. *Nature Reviews Neuroscience*, 9(5):370–386. [Cited on pages 44 and 64]

Gent, T. C., Bandarabadi, M., Herrera, C. G., and Adamantidis, A. R. (2018). Thalamic dual control of sleep and wakefulness. *Nature neuroscience*, 21(7):974–984. [Cited on pages 64, 65, and 110]

Genzel, L., Kroes, M. C. W., Dresler, M., and Battaglia, F. P. (2014). Light sleep versus slow wave sleep in memory consolidation: a question of global versus local processes? *Trends in Neurosciences*, 37(1):10–19. [Cited on pages 60 and 102]

Gerfen, C. R. and Surmeier, D. J. (2011). Modulation of striatal projection systems by dopamine. *Annual Review of Neuroscience*, 34(1):441–466. [Cited on page 12]

Giacino, J. T., Fins, J. J., Laureys, S., and Schiff, N. D. (2014). Disorders of consciousness after acquired brain injury: the state of the science. *Nature Reviews Neurology*, 10(2), 99. [Cited on page 108]

Gittis, A. H., Leventhal, D. K., Fensterheim, B. A., Pettibone, J. R., Berke, J. D., and Kreitzer, A. C. (2011). Selective inhibition of striatal fast-spiking interneurons causes dyskinesias. *Journal of Neuroscience*, 31(44):15727–15731. [Cited on page 36]

Gleit, R. D., Diniz Behn, C. G., and Booth, V. (2013). Modeling Interindividual Differences in Spontaneous Internal Desynchrony Patterns. *Journal of Biological Rhythms*, 28(5):339–355. [Cited on page 63]

Golomb, D., Wang, X. J., and Rinzel, J. (1994). Synchronization properties of spindle oscillations in a thalamic reticular nucleus model. *Journal of Neurophysiology*, 72(3):1109–1126. [Cited on page 119]

Golomb, D., Wang, X. J., and Rinzel, J. (1996). Propagation of spindle waves in a thalamic slice model. *Journal of Neurophysiology*, 75(2):750–769. [Cited on page 71]

Graveland, G. A., Williams, R. S., and Difiglia, M. (1985). A Golgi study of the human neostriatum: Neurons and afferent fibers. *The Journal of comparative neurology*, 234(3):317–333. [Cited on page 40]

Hagiwara, N. and Irisawa, H. (1989). Modulation by intracellular Ca2+ of the hyperpolarization-activated inward current in rabbit single sino-atrial node cells. *The Journal of physiology*, 409:121–141. [Cited on page 58]

Halassa, M. M., Siegle, J. H., Ritt, J. T., Ting, J. T., Feng, G., and Moore, C. I. (2011). Selective optical drive of thalamic reticular nucleus generates thalamic bursts and cortical spindles. *Nature neuroscience*, 14(9):1118–1120. [Cited on pages 59 and 97]

Han, X., Qian, X., Bernstein, J. G., Zhou, H.-H., Franzesi, G. T., Stern, P., Bronson, R. T., Graybiel, A. M., Desimone, R., and Boyden, E. S. (2009). Millisecond-timescale optical control of neural dynamics in the nonhuman primate brain. *Neuron*, 62(2):191–198. [Cited on pages 17 and 22]

Hardel, N., Harmel, N., Zolles, G., Fakler, B., and Klocker, N. (2008). Recycling endosomes supply cardiac pacemaker channels for regulated surface expression. *Cardiovascular Research*, 79(1):52–60. [Cited on page 51]

Harmar, A. J., Fahrenkrug, J., Gozes, I., Laburthe, M., May, V., Pisegna, J. R., Vaudry, D., Vaudry, H., Waschek, J. A., and Said, S. I. (2012). Pharmacology and functions of receptors for vasoactive intestinal peptide and pituitary adenylate cyclase-activating polypeptide: IUPHAR Review 1. *British journal of pharmacology*, 166(1):4–17. [Cited on page 53]

He, C., Chen, F., Li, B., and Hu, Z. (2013). Neurophysiology of HCN channels: From cellular functions to multiple regulations. *Progress in neurobiology*, 112:1–23. [Cited on page 46]

Herrojo Ruiz, M., Brucke, C., Nikulin, V. V., Schneider, G.-H., and Kuhn, A. A. (2014). Beta-band amplitude oscillations in the human internal globus pallidus support the encoding of sequence boundaries during initial sensorimotor sequence learning. *NeuroImage*, 85 Pt 2:779–793. [Cited on page 11]

Higley, M. J., Gittis, A. H., Oldenburg, I. A., Balthasar, N., Seal, R. P., Edwards, R. H., Lowell, B. B., Kreitzer, A. C., and Sabatini, B. L. (2011). Cholinergic Interneurons Mediate Fast VGluT3-Dependent Glutamatergic Transmission in the Striatum. *PLoS ONE*, 6(4):e19155. [Cited on pages 36 and 40]

Higley, M. J., Soler-Llavina, G. J., and Sabatini, B. L. (2009). Cholinergic modulation of multivesicular release regulates striatal synaptic potency and integration. *Nature neuroscience*, 12(9):1121–1128. [Cited on page 41]

Hines, M. L. and Carnevale, N. T. (1997). The NEURON simulation environment. *Neural computation*, 9(6):1179–1209. [Cited on page 122]

Hirsch, J. C., Fourment, A., and Marc, M. E. (1983). Sleep-related variations of membrane potential in the lateral geniculate body relay neurons of the cat. *Brain research*, 259(2):308–312. [Cited on pages 59 and 101]

Hodgkin, A. L. and Huxley, A. F. (1952). A quantitative description of membrane current and its application to conduction and excitation in nerve. *The Journal of physiology*, 117(4):500–544. [Cited on page 5]

Holgado, A. J. N., Terry, J. R., and Bogacz, R. (2010). Conditions for the generation of beta oscillations in the subthalamic nucleus-globus pallidus network. *Journal of Neuroscience*, 30(37):12340–12352. [Cited on page 38]

Honjoh, S., Sasai, S., Schiereck, S. S., Nagai, H., Tononi, G., and Cirelli, C. (2018). Regulation of cortical activity and arousal by the matrix cells of the ventromedial thalamic nucleus. *Nature Communications*, 9(1), 2100. [Cited on page 65]

Huber, R., Deboer, T., and Tobler, I. (2000). Effects of sleep deprivation on sleep and sleep EEG in three mouse strains: empirical data and simulations. *Brain research*, 857(1-2):8–19. [Cited on page 103]

Huguenard, J. R. and McCormick, D. A. (1992). Simulation of the currents involved in rhythmic oscillations in thalamic relay neurons. *Journal of Neurophysiology*, 68(4):1373–1383. [Cited on page 116]

Huupponen, E., Maksimow, A., Lapinlampi, P., Sarkela, M., Saastamoinen, A., Snapir, A., Scheinin, H., Scheinin, M., Merilainen, P., Himanen, S.-L., and Jaaskelainen, S. (2008). Electroencephalogram spindle activity during dexmedetomidine sedation and physiological sleep. *Acta Anaesthesiologica Scandinavica*, 52(2):289–294. [Cited on page 106]

Ikarashi, Y., Takahashi, A., Ishimaru, H., Arai, T., and Maruyama, Y. (1997). Regulation of dopamine D1 and D2 receptors on striatal acetylcholine release in rats. *Brain research bulletin*, 43(1):107–115. [Cited on page 12]

Izhikevich, E. M. (2003). Simple model of spiking neurons. *IEEE Transactions on Neural Networks*, 14(6):1569–1572. [Cited on page 138]

Izhikevich, E. M. (2007). Dynamical systems in neuroscience. Cambridge, MA: MIT press. [Cited on page 96]

Jenkinson, N., Kuhn, A. A., and Brown, P. (2013). γ oscillations in the human basal ganglia. *Experimental Neurology*, 245:72–76. [Cited on page 40]

Jennett, B., Adams, J. H., Murray, L. S., and Graham, D. I. (2001). Neuropathology in vegetative and severely disabled patients after head injury. *Neurology*, 56(4):486–490. [Cited on page 65]

Jones, E. G. (2001). The thalamic matrix and thalamocortical synchrony. *Trends in Neurosciences*, 24(10):595–601. [Cited on page 65]

Jones, E. G. (2012). The thalamus. Cambridge: Cambridge University Press. [Cited on page 110]

Joo, K. M., Chung, Y. H., Kim, M. K., Nam, R. H., Lee, B. L., Lee, K. H., and Cha, C. I. (2004). Distribution of vasoactive intestinal peptide and pituitary adenylate cyclase-activating polypeptide receptors (VPAC1, VPAC2, and PAC1 receptor) in the rat brain. *The Journal of comparative neurology*, 476(4):388–413. [Cited on page 46]

Jung, S., Bullis, J. B., Lau, I. H., Jones, T. D., Warner, L. N., and Poolos, N. P. (2010). Downregulation of Dendritic HCN Channel Gating in Epilepsy Is Mediated by Altered Phosphorylation Signaling. *The Journal of neuroscience*, 30(19):6678–6688. [Cited on page 51]

Kaneko, T., Tashiro, K., Sugimoto, T., Konishi, A., and Mizuno, N. (1985). Identification of thalamic neurons with vasoactive intestinal polypeptide-like immunoreactivity in the rat. *Brain research*, 347(2):390–393. [Cited on pages 45 and 54]

Katzenschlager, R., Sampaio, C., Costa, J., and Lees, A. (2003). Anticholinergics for symptomatic management of Parkinson's disease. *The Cochrane database of systematic reviews*, 138(2):CD003735. [Cited on page 38]

Kempf, F., Brucke, C., Salih, F., Trottenberg, T., Kupsch, A., Schneider, G.-H., Doyle Gaynor, L. M. F., Hoffmann, K.-T., Vesper, J., Wohrle, J., Altenmuller, D.-M., Krauss, J. K., Mazzone, P., Di Lazzaro, V., Yelnik, J., Kuhn, A. A., and Brown, P. (2009). Gamma activity and reactivity in human thalamic local field potentials. *The European journal of neuroscience*, 29(5):943–953. [Cited on pages 12 and 40]

Kim, A., Latchoumane, C., and Lee, S. (2012). Optogenetically induced sleep spindle rhythms alter sleep architectures in mice. In *Proceedings of the National Academy of Sciences of the United States of America*. [Cited on page 101]

Kim, J., Jung, S.-C., Clemens, A. M., Petralia, R. S., and Hoffman, D. A. (2007). Regulation of Dendritic Excitability by Activity-Dependent Trafficking of the A-Type K+ Channel Subunit Kv4.2 in Hippocampal Neurons. *Neuron*, 54(6):933–947. [Cited on pages 51 and 52]

Kim, U., Bal, T., and McCormick, D. A. (1995). Spindle waves are propagating synchronized oscillations in the ferret LGNd in vitro. *Journal of Neurophysiology*, 74(3):1301–1323. [Cited on page 79]

Klinzing, J. G., Molle, M., Weber, F., Supp, G., Hipp, J. F., Engel, A. K., and Born, J. (2016). Spindle activity phase-locked to sleep slow oscillations. *NeuroImage*, 134(C):607–616. [Cited on page 110]

Kondabolu, K., Kowalski, M. M., Roberts, E. A., and Han, X. (2015). Optogenetics and Deep Brain Stimulation Neurotechnologies. In *Cognitive Enhancement* (pp. 441-450). Cham: Springer International Publishing. [Cited on page 3]

Kondabolu, K., Roberts, E. A., Bucklin, M., McCarthy, M. M., Kopell, N., and Han, X. (2016). Striatal cholinergic interneurons generate beta and gamma oscillations in the corticostriatal circuit and produce motor deficits. *Proceedings of the National Academy of Sciences of the United States of America*, 113(22):E3159–68. [Cited on pages 10 and 14]

Koos, T. and Tepper, J. M. (2002). Dual cholinergic control of fast-spiking interneurons in the neostriatum. *Journal of Neuroscience*, 22(2):529–535. [Cited on page 41]

Kopell, N. and Ermentrout, G. B. (1986). Subcellular Oscillations and Bursting. *Mathematical Biosciences*, 78(2):265–291. [Cited on page 96]

Koves, K., Arimura, A., Gorcs, T. G., and Somogyvari-Vigh, A. (1991). Comparative distribution of immunoreactive pituitary adenylate cyclase activating polypeptide and vasoactive intestinal polypeptide in rat forebrain. *Neuroendocrinology*, 54(2):159–169. [Cited on pages 53 and 54]

Kramer, M. A. and Eden, U. T. (2016). *Case Studies in Neural Data Analysis*. A Guide for the Practicing Neuroscientist. MIT Press. [Cited on page 1]

Kravitz, A. V., Freeze, B. S., Parker, P. R. L., Kay, K., Thwin, M. T., Deisseroth, K., and Kreitzer, A. C. (2010). Regulation of parkinsonian motor behaviours by optogenetic control of basal ganglia circuitry. *Nature*, 466(7306):622–626. [Cited on page 36]

Krishnan, G. P., Chauvette, S., Shamie, I., and Soltani, S. (2016). Cellular and neurochemical basis of sleep stages in the thalamocortical network. *eLife*. [Cited on pages 57 and 114]

Kuhn, A. A., Kempf, F., Brucke, C., Gaynor Doyle, L., Martinez-Torres, I., Pogosyan, A., Trottenberg, T., Kupsch, A., Schneider, G.-H., Hariz, M. I., Vandenberghe, W., Nuttin, B., and Brown, P. (2008). High-frequency stimulation of the subthalamic nucleus suppresses oscillatory beta activity in patients with Parkinson's disease in parallel with improvement in motor performance. *Journal of Neuroscience*, 28(24):6165–6173. [Cited on page 11]

Kuhn, A. A., Kupsch, A., Schneider, G.-H., and Brown, P. (2006). Reduction in subthalamic 8-35 Hz oscillatory activity correlates with clinical improvement in Parkinson's disease. *European Journal of Neuroscience*, 23(7):1956–1960. [Cited on pages 11 and 34]

Kuhn, A. A., Tsui, A., Aziz, T., Ray, N., Brucke, C., Kupsch, A., Schneider, G.-H., and Brown, P. (2009). Pathological synchronisation in the subthalamic nucleus of patients with Parkinson's disease relates to both bradykinesia and rigidity. *Experimental Neurology*, 215(2):380–387. [Cited on page 34]

Laburthe, M., Couvineau, A., and Marie, J. C. (2002). VPAC receptors for VIP and PACAP. *Receptors & channels*, 8(3-4):137–153. [Cited on page 46]

Lacey, M. G., Gooding-Williams, G., Prokic, E. J., Yamawaki, N., Hall, S. D., Stanford, I. M., and Woodhall, G. L. (2014). Spike firing and IPSPs in layer V pyramidal neurons during beta oscillations in rat primary motor cortex (M1) in vitro. *PLoS ONE*, 9(1):e85109. [Cited on page 38]

Landisman, C. E., Long, M. A., Beierlein, M., Deans, M. R., Paul, D. L., and Connors, B. W. (2002). Electrical synapses in the thalamic reticular nucleus. *Journal of Neuroscience*, 22(3):1002–1009. [Cited on page 119]

Landolt, H. P., Dijk, D. J., Gaus, S. E., and Borbély, A. A. (1995). Caffeine reduces low-frequency delta activity in the human sleep EEG. *Neuropsychopharmacology*, 12(3):229–238. [Cited on page 102]

Laureys, S., Faymonville, M. E., Luxen, A., Lamy, M., Franck, G., and Maquet, P. (2000). Restoration of thalamocortical connectivity after recovery from persistent vegetative state. *The Lancet*, 355(9217):1790–1791. [Cited on page 108]

Lee, S.-H. and Cox, C. L. (2003). Vasoactive intestinal peptide selectively depolarizes thalamic relay neurons and attenuates intrathalamic rhythmic activity. *Journal of Neurophysiology*, 90(2):1224–1234. [Cited on pages 44, 45, 51, 52, and 54]

Lee, S.-H. and Cox, C. L. (2006). Excitatory actions of vasoactive intestinal peptide on mouse thalamocortical neurons are mediated by VPAC2 receptors. *Journal of Neurophysiology*, 96(2):858–871. [Cited on pages 44, 51, and 52]

Lee, S.-H. and Cox, C. L. (2008). Excitatory actions of peptide histidine isoleucine on thalamic relay neurons. *Neuropharmacology*, 55(8):1329–1339. [Cited on pages 44, 51, 53, and 54]

Lefkimmiatis, K. and Zaccolo, M. (2014). cAMP signaling in subcellular compartments. *Pharmacology & Therapeutics*, 143(3):295–304. [Cited on page 47]

Lemieux, M., Chen, J.-Y., Lonjers, P., Bazhenov, M., and Timofeev, I. (2014). The impact of cortical deafferentation on the neocortical slow oscillation. *Journal of Neuroscience*, 34(16):5689–5703. [Cited on page 110]

Leventhal, D. K., Gage, G. J., Schmidt, R., Pettibone, J. R., Case, A. C., and Berke, J. D. (2012). Basal Ganglia Beta Oscillations Accompany Cue Utilization. *Neuron*, 73(3):523–536. [Cited on pages 2, 11, and 40]

Lewis, A. S., Schwartz, E., Savio Chan, C., Noam, Y., Shin, M., Wadman, W. J., James Surmeier, D., Baram, T. Z., Macdonald, R. L., and Chetkovich, D. M. (2009). Alternatively Spliced Isoforms of TRIP8b Differentially Control h Channel Trafficking and Function. *The Journal of neuroscience*, 29(19):6250–6265. [Cited on page 51]

Lewis, L. D., Voigts, J., Flores, F. J., Schmitt, L. I., Wilson, M. A., Halassa, M. M., and Brown, E. N. (2015). Thalamic reticular nucleus induces fast and local modulation of arousal state. *eLife*, 4:e08760. [Cited on pages 65 and 110]

Little, S., Pogosyan, A., Kuhn, A. A., and Brown, P. (2012). Beta band stability over time correlates with Parkinsonian rigidity and bradykinesia. *Experimental Neurology*, 236(2):383–388. [Cited on pages 2, 6, 8, and 11]

Liu, D. and Dan, Y. (2019). A Motor Theory of Sleep-Wake Control: Arousal-Action Circuit. *Annual Review of Neuroscience*, 42(1):annurev–neuro–080317–061813–20. [Cited on page 62]

Llinas, R. R. and Steriade, M. (2006). Bursting of thalamic neurons and states of vigilance. *Journal of Neurophysiology*, 95(6):3297–3308. [Cited on pages 2 and 54]

Lu, J., Greco, M. A., Shiromani, P., and Saper, C. B. (2000). Effect of lesions of the ventrolateral preoptic nucleus on NREM and REM sleep. *Journal of Neuroscience*, 20(10):3830–3842. [Cited on page 61]

Lu, J., Sherman, D., Devor, M., and Saper, C. B. (2006). A putative flip–flop switch for control of REM sleep. *Nature*, 441(7093):589–594. [Cited on page 62]

Luthi, A. (2014). Sleep Spindles: Where They Come From, What They Do. *The Neuroscientist*, 20(3):243–256. [Cited on page 59]

Luthi, A., Bal, T., and McCormick, D. A. (1998). Periodicity of thalamic spindle waves is abolished by ZD7288,a blocker of Ih. *Journal of Neurophysiology*, 79(6):3284–3289. [Cited on page 97]

Luthi, A. and McCormick, D. A. (1999). Modulation of a pacemaker current through Ca(2+)-induced stimulation of cAMP production. *Nature neuroscience*, 2(7):634–641. [Cited on pages 46 and 57]

Lyamin, O. I., Manger, P. R., Ridgway, S. H., Mukhametov, L. M., and Siegel, J. M. (2008). Cetacean sleep: an unusual form of mammalian sleep. *Neuroscience and Biobehavioral Reviews*, 32(8):1451–1484. [Cited on page 62]

Lytton, W. W., Contreras, D., Destexhe, A., and Steriade, M. (1997). Dynamic interactions determine partial thalamic quiescence in a computer network model of spike-and-wave seizures. *Journal of Neurophysiology*, 77(4):1679–1696. [Cited on page 56]

Magnin, M., Rey, M., Bastuji, H., Guillemant, P., Mauguière, F., and Garcia-Larrea, L. (2010). Thalamic deactivation at sleep onset precedes that of the cerebral cortex in humans. *Proceedings of the National Academy of Sciences of the United States of America*, 107(8):3829–3833. [Cited on page 64]

Magrassi, L., Zippo, A. G., Azzalin, A., Bastianello, S., Imberti, R., and Biella, G. E. M. (2018). Single unit activities recorded in the thalamus and the overlying parietal cortex of subjects affected by disorders of consciousness. *PLoS ONE*, 13(11):e0205967–17. [Cited on page 108]

Mallet, N., Pogosyan, A., Sharott, A., Csicsvari, J., Bolam, J. P., Brown, P., and Magill, P. J. (2008). Disrupted dopamine transmission and the emergence of exaggerated beta oscillations in subthalamic nucleus and cerebral cortex. *Journal of Neuroscience*, 28(18):4795–4806. [Cited on pages 12 and 35]

Manning, J. R., Jacobs, J., Fried, I., and Kahana, M. J. (2009). Broadband shifts in local field potential power spectra are correlated with single-neuron spiking in humans. *Journal of Neuroscience*, 29(43):13613–13620. [Cited on pages 24, 34, 39, and 40]

Maurice, N., Liberge, M., Jaouen, F., Ztaou, S., Hanini, M., Camon, J., Deisseroth, K., Amalric, M., Kerkerian-Le Goff, L., and Beurrier, C. (2015). Striatal Cholinergic Interneurons Control Motor Behavior and Basal Ganglia Function in Experimental Parkinsonism. *CellReports*, 13(4):657–666. [Cited on pages 35 and 36]

Maxwell, W. L., MacKinnon, M. A., Smith, D. H., McIntosh, T. K., and Graham, D. I. (2006). Thalamic nuclei after human blunt head injury. *Journal of Experimental Neurology*, 65(5):478–488. [Cited on page 65]

McCarley, R. W. and Hobson, J. A. (1975). Neuronal excitability modulation over the sleep cycle: a structural and mathematical model. *Science*, 189(4196):58–60. [Cited on page 63]

McCarthy, M. M., Brown, E. N., and Kopell, N. (2008). Potential Network Mechanisms Mediating Electroencephalographic Beta Rhythm Changes during Propofol-Induced Paradoxical Excitation. *Journal of Neuroscience*, 28(50):13488–13504. [Cited on pages 64, 66, and 117]

McCarthy, M. M. and Kopell, N. (2012). The Effect of Propofol Anesthesia on Rebound Spiking. *SIAM Journal on Applied Dynamical Systems*, 11(4):1674–1697. [Cited on page 64]

McCarthy, M. M., Moore-Kochlacs, C., Gu, X., Boyden, E. S., Han, X., and Kopell, N. (2011). Striatal origin of the pathologic beta oscillations in Parkinson's disease. *Proceedings of the National Academy of Sciences of the United States of America*, 108(28):11620–11625. [Cited on pages 6, 7, 12, 13, 16, 34, and 37]

McCormick, D. A. (1992). Neurotransmitter actions in the thalamus and cerebral cortex and their role in neuromodulation of thalamocortical activity. *Progress in neurobiology*, 39(4):337–388. [Cited on pages 44, 55, 102, and 110]

McCormick, D. A. and Huguenard, J. R. (1992). A model of the electrophysiological properties of thalamocortical relay neurons. *Journal of Neurophysiology*, 68(4):1384–1400. [Cited on pages 55, 56, and 114]

McCormick, D. A. and Pape, H. C. (1990). Properties of a hyperpolarization-activated cation current and its role in rhythmic oscillation in thalamic relay neurones. *The Journal of physiology*, 431:291–318. [Cited on pages 56 and 57]

Miller, J. W. and Ferrendelli, J. A. (1990). Characterization of GABAergic seizure regulation in the midline thalamus. *Neuropharmacology*, 29(7):649–655. [Cited on page 65]

Nelson, A. B., Hammack, N., Yang, C. F., Shah, N. M., Seal, R. P., and Kreitzer, A. C. (2014). Striatal cholinergic interneurons Drive GABA release from dopamine terminals. *Neuron*, 82(1):63–70. [Cited on page 41]

Nelson, L. E., Guo, T. Z., Lu, J., Saper, C. B., Franks, N. P., and Maze, M. (2002). The sedative component of anesthesia is mediated by GABAA receptors in an endogenous sleep pathway. *Nature neuroscience*, 5(10):979–984. [Cited on page 64]

Neske, G. T. (2015). The Slow Oscillation in Cortical and Thalamic Networks: Mechanisms and Functions. *Frontiers in neural circuits*, 9:88. [Cited on pages 101 and 110]

Ni, Q., Ganesan, A., Aye-Han, N.-N., Gao, X., Allen, M. D., Levchenko, A., and Zhang, J. (2010). Signaling diversity of PKA achieved via a Ca2+-cAMP-PKA oscillatory circuit. *Nature Chemical Biology*, 7(1):34–40. [Cited on page 47]

Nir, Y., Staba, R. J., Andrillon, T., Vyazovskiy, V. V., Cirelli, C., Fried, I., and Tononi, G. (2011). Regional slow waves and spindles in human sleep. *Neuron*, 70(1):153–169. [Cited on page 98]

Nobili, L., De Gennaro, L., Proserpio, P., Moroni, F., Sarasso, S., Pigorini, A., De Carli, F., and Ferrara, M. (2012). *Local aspects of sleep: Observations from intracerebral recordings in humans*, volume 199. Elsevier B.V., 1 edition. [Cited on page 62]

Oldenburg, I. A. and Sabatini, B. L. (2015). Antagonistic but Not Symmetric Regulation of Primary Motor Cortex by Basal Ganglia Direct and Indirect Pathways. *Neuron*, 86(5):1174–1181. [Cited on page 38]

Pigarev, I. N., Nothdurft, H. C., and Kastner, S. (1997). Evidence for asynchronous development of sleep in cortical areas. *Neuroreport*, 8(11):2557–2560. [Cited on page 62]

Pinault, D. (2004). The thalamic reticular nucleus: structure, function and concept. *Brain research. Brain research reviews*, 46(1):1–31. [Cited on page 45]

Pinault, D., Smith, Y., and Deschenes, M. (1997). Dendrodendritic and axoaxonic synapses in the thalamic reticular nucleus of the adult rat. *The Journal of neuroscience*, 17(9):3215–3233. [Cited on page 119]

Pisani, A., Bernardi, G., Ding, J., and Surmeier, D. J. (2007). Re-emergence of striatal cholinergic interneurons in movement disorders. *Trends in Neurosciences*, 30(10):545–553. [Cited on page 12]

Pittman-Polletta, B. R., Quach, A., Mohammed, A. I., Romano, M., Kondabolu, K., Kopell, N. J., Han, X., and McCarthy, M. M. (2018). Striatal cholinergic receptor activation causes a rapid, selective and state-dependent rise in cortico-striatal β activity. *European Journal of Neuroscience*, 48(8):2857–2868. [Cited on pages 6 and 7]

Pollok, B., Krause, V., Martsch, W., Wach, C., Schnitzler, A., and Sudmeyer, M. (2012). Motor-cortical oscillations in early stages of Parkinson's disease. *The Journal of physiology*, 590(13):3203–3212. [Cited on page 35]

Porkka-Heiskanen, T., Strecker, R. E., and McCarley, R. W. (2000). Brain site-specificity of extracellular adenosine concentration changes during sleep deprivation and spontaneous sleep: an in vivo microdialysis study. *Neuroscience*, 99(3):507–517. [Cited on page 103]

Porkka-Heiskanen, T., Strecker, R. E., Thakkar, M., Bjorkum, A. A., Greene, R. W., and McCarley, R. W. (1997). Adenosine: a mediator of the sleep-inducing effects of prolonged wakefulness. *Science*, 276(5316):1265–1268. [Cited on page 103]

Prinz, A. A., Bucher, D., and Marder, E. (2004). Similar network activity from disparate circuit parameters. *Nature neuroscience*, 7(12):1345–1352. [Cited on page 123]

Prlić, A. and Procter, J. B. (2012). Ten Simple Rules for the Open Development of Scientific Software. *PLoS Computational Biology*, 8(12):e1002802–3. [Cited on page 128]

Purdon, P. L., Sampson, A., Pavone, K. J., and Brown, E. N. (2015). Clinical Electroencephalography for Anesthesiologists: Part I: Background and Basic Signatures. *Anesthesiology*, 123(4):937–960. [Cited on page 64]

Racine, J. S. (2011). RStudio: A Platform-Independent IDE for R and Sweave. *Journal of Applied Econometrics*, 27(1):167–172. [Cited on page 124]

Ragan-Kelley, M., Perez, F., and Meeting, B. G. A. F. (2014). The Jupyter/IPython architecture: a unified view of computational research, from interactive exploration to communication and publication. *adsabs.harvard.edu*. [Cited on page 124]

Ramanathan, S., Hanley, J. J., Deniau, J.-M., and Bolam, J. P. (2002). Synaptic convergence of motor and somatosensory cortical afferents onto GABAergic interneurons in the rat striatum. *Journal of Neuroscience*, 22(18):8158–8169. [Cited on page 28]

Ramcharan, E. J., Gnadt, J. W., and Sherman, S. M. (2000). Burst and tonic firing in thalamic cells of unanesthetized, behaving monkeys. *Visual neuroscience*, 17(1):55–62. [Cited on page 55]

Rich, T. C., Fagan, K. A., Tse, T. E., Schaack, J., Cooper, D. M., and Karpen, J. W. (2001). A uniform extracellular stimulus triggers distinct cAMP signals in different compartments of a simple cell. *Proceedings of the National Academy of Sciences of the United States of America*, 98(23):13049–13054. [Cited on page 47]

Roberts, E. A. (2017). 26th Annual Computational Neuroscience Meeting (CNS*2017): Part 2. *BMC Neuroscience*, 18(S1):59.

[Cited on pages 8 and 128]

Roberts, E. A., Salisbury, K., and Chan, S. (2011). Tissue Modeling in a Patient-Specific Skull Base Surgical Simulator. *Otolaryngology — Head and Neck Surgery*, 145(2), P230-P230. [Cited on page 4]

Santoro, B. (2004). Regulation of HCN Channel Surface Expression by a Novel C-Terminal Protein-Protein Interaction. *The Journal of neuroscience*, 24(47):10750–10762. [Cited on page 51]

Saper, C. B., Chou, T. C., and Scammell, T. E. (2001). The sleep switch: hypothalamic control of sleep and wakefulness. *Trends in Neurosciences*, 24(12):726–731. [Cited on pages 61 and 66]

Scammell, T. E., Arrigoni, E., and Lipton, J. O. (2017). Neural Circuitry of Wakefulness and Sleep. *Neuron*, 93(4):747–765. [Cited on pages 60, 89, 92, and 99]

Schiff, N. D., Giacino, J. T., Kalmar, K., Victor, J. D., Baker, K., Gerber, M., Fritz, B., Eisenberg, B., O'Connor, J., Kobylarz, E. J., Farris, S., Machado, A., McCagg, C., Plum, F., Fins, J. J., and Rezai, A. R. (2007). Behavioural improvements with thalamic stimulation after severe traumatic brain injury. *Nature*, 448(7153):600–603. [Cited on page 65]

Schmidt, R., Leventhal, D. K., Mallet, N., Chen, F., and Berke, J. D. (2013). Canceling actions involves a race between basal ganglia pathways. *Nature neuroscience*, 16(8):1118–1124. [Cited on pages 2 and 11]

Shah, M. M., Hammond, R. S., and Hoffman, D. A. (2010). Dendritic ion channel trafficking and plasticity. *Trends in Neurosciences*, 33(7):307–316. [Cited on page 51]

Sharott, A., Magill, P. J., Harnack, D., Kupsch, A., Meissner, W., and Brown, P. (2005). Dopamine depletion increases the power and coherence of beta-oscillations in the cerebral cortex and subthalamic nucleus of the awake rat. *The European journal of neuroscience*, 21(5):1413–1422. [Cited on page 12]

Shen, W., Hamilton, S. E., Nathanson, N. M., and Surmeier, D. J. (2005). Cholinergic suppression of KCNQ channel currents enhances excitability of striatal medium spiny neurons. *Journal of Neuroscience*, 25(32):7449–7458. [Cited on page 41]

Shen, W., Tian, X., Day, M., Ulrich, S., Tkatch, T., Nathanson, N. M., and Surmeier, D. J. (2007). Cholinergic modulation of Kir2 channels selectively elevates dendritic excitability in striatopallidal neurons. *Nature neuroscience*, 10(11):1458–1466. [Cited on page 41]

Shepherd, G. M. G. (2013). Corticostriatal connectivity and its role in disease. *Nature Reviews Neuroscience*, 14(4):278–291. [Cited on page 36]

Sherfey, J. S., Soplata, A. E., Ardid, S., Roberts, E. A., Stanley, D. A., Pittman-Polletta, B. R., and Kopell, N. J. (2018). DynaSim: A MATLAB Toolbox for Neural Modeling and Simulation. *Frontiers in Neuroinformatics*, 12:146–15. [Cited on pages 113 and 122]

Sherman, S. M. (2001). Tonic and burst firing: dual modes of thalamocortical relay. *Trends in Neurosciences*, 24(2):122–126. [Cited on pages 2 and 55]

Siclari, F. and Tononi, G. (2017). Local aspects of sleep and wakefulness. *Current opinion in neurobiology*, 44:222–227. [Cited on page 62]

Sitaramayya, A. and Liebman, P. A. (1983). Phosphorylation of rhodopsin and quenching of cyclic GMP phosphodiesterase activation by ATP at weak bleaches. *Journal of Biological Chemistry*, 258(20):12106–12109. [Cited on page 51]

Skinner, F. K., Kopell, N., and Marder, E. (1994). Mechanisms for oscillation and frequency control in reciprocally inhibitory model neural networks. *Journal of computational neuroscience*, 1(1-2):69–87. [Cited on page 99]

Sochurkova, D. and Rektor, I. (2003). Event-related desynchronization/synchronization in the putamen. An SEEG case study. *Experimental brain research*, 149(3):401–404. [Cited on page 11]

Soplata, A. E., McCarthy, M. M., Sherfey, J., Lee, S., Purdon, P. L., Brown, E. N., and Kopell, N. (2017). Thalamocortical control of propofol phase-amplitude coupling. *PLoS Computational Biology*, 13(12):e1005879–24. [Cited on pages 56, 64, 69, and 105]

Stein, E. and Bar-Gad, I. (2013). β oscillations in the cortico-basal ganglia loop during parkinsonism. *Experimental Neurology*, 245:52–59. [Cited on page 35]

Steriade, M., Deschenes, M., Domich, L., and Mulle, C. (1985). Abolition of spindle oscillations in thalamic neurons disconnected from nucleus reticularis thalami. *Journal of Neurophysiology*, 54(6):1473–1497. [Cited on page 96]

Steriade, M., Domich, L., Oakson, G., and Deschenes, M. (1987). The deafferented reticular thalamic nucleus generates spindle rhythmicity. *Journal of Neurophysiology*, 57(1):260–273. [Cited on pages 59 and 96]

Stimberg, M., Goodman, D. F., Benichoux, V., and Brette, R. (2013). Brian 2 - the second coming: spiking neural network simulation in Python with code generation. *BMC Neuroscience*, 14(S1):192. [Cited on page 122]

Sun, Q.-Q., Prince, D. A., and Huguenard, J. R. (2003). Vasoactive intestinal polypeptide and pituitary adenylate cyclase-activating polypeptide activate hyperpolarization-activated cationic current and depolarize thalamocortical neurons in vitro. *Journal of Neuroscience*, 23(7):2751–2758.

[Cited on pages 44, 45, 46, 51, 52, 53, 54, 55, and 56]

Swadlow, H. A. and Gusev, A. G. (2001). The impact of 'bursting' thalamic impulses at a neocortical synapse. *Nature neuroscience*, 4(4):402–408. [Cited on page 55]

Tachibana, Y., Iwamuro, H., Kita, H., Takada, M., and Nambu, A. (2011). Subthalamo-pallidal interactions underlying parkinsonian neuronal oscillations in the primate basal ganglia. *The European journal of neuroscience*, 34(9):1470–1484.

[Cited on pages 38 and 39]

Taylor, A. L., Goaillard, J. M., and Marder, E. (2009). How Multiple Conductances Determine Electrophysiological Properties in a Multicompartment Model. *The Journal of neuroscience*, 29(17):5573–5586. [Cited on page 123]

Terman, D., Bose, A., and Kopell, N. (1996). Functional reorganization in thalamocortical networks: transition between spindling and delta sleep rhythms. *Proceedings of the National Academy of Sciences of the United States of America*, 93(26):15417–15422. [Cited on page 56]

Thengone, D. J., Voss, H. U., Fridman, E. A., and Schiff, N. D. (2016). Local changes in network structure contribute to late communication recovery after severe brain injury. *Science translational medicine*, 8(368):368re5–368re5. [Cited on page 108]

Toledo, J. B., Lopez-Azcarate, J., Garcia-Garcia, D., Guridi, J., Valencia, M., Artieda, J., Obeso, J., Alegre, M., and Rodriguez-Oroz, M. (2014). High beta activity in the subthalamic nucleus and freezing of gait in Parkinson's disease. *Neurobiology of disease*, 64:60–65. [Cited on page 37]

Traub, R. D. and Whittington, M. A. (2010). *Cortical Oscillations in Health and Disease.* Oxford University Press, USA. [Cited on page 1]

Ulrich, D. and Huguenard, J. R. (1996). Gamma-aminobutyric acid type B receptor-dependent burst-firing in thalamic neurons: a dynamic clamp study. *Proceedings of the National Academy of Sciences of the United States of America*, 93(23):13245–13249. [Cited on page 119]

Vaaga, C. E., Borisovska, M., and Westbrook, G. L. (2014). Dual-transmitter neurons: functional implications of co-release and co-transmission. *Current opinion in neurobiology*, 29:25–32. [Cited on page 45]

van der Meer, M. A. A. (2009). Low and high gamma oscillations in rat ventral striatum have distinct relationships to behavior, reward, and spiking activity on a learned spatial decision task. *Frontiers in Integrative Neuroscience*, 3. [Cited on page 40]

Van der Werf, Y. D., Witter, M. P., and Groenewegen, H. J. (2002). The intralaminar and midline nuclei of the thalamus. Anatomical and functional evidence for participation in processes of arousal and awareness. *Brain research. Brain research reviews*, 39(2-3):107–140. [Cited on pages 67 and 115]

Van Dort, C. J., Zachs, D. P., Kenny, J. D., Zheng, S., Goldblum, R. R., Gelwan, N. A., Ramos, D. M., Nolan, M. A., Wang, K., Weng, F.-J., Lin, Y., Wilson, M. A., and Brown, E. N. (2015). Optogenetic activation of cholinergic neurons in the PPT or LDT induces REM sleep. *Proceedings of the National Academy of Sciences of the United States of America*, 112(2):584–589. [Cited on page 61]

Vijayan, S., Ching, S., Purdon, P. L., Brown, E. N., and Kopell, N. J. (2013). Thalamocortical Mechanisms for the Anteriorization of Alpha Rhythms during Propofol-Induced Unconsciousness. *The Journal of neuroscience*, 33(27):11070–11075. [Cited on page 64]

Vijayan, S., Klerman, E. B., Adler, G. K., and Kopell, N. J. (2015). Thalamic mechanisms underlying alpha-delta sleep with implications for fibromyalgia. *Journal of Neurophysiology*, 114(3):1923–1930. [Cited on page 56]

Vijayan, S. and Kopell, N. J. (2012). Thalamic model of awake alpha oscillations and implications for stimulus processing. *Proceedings of the National Academy of Sciences of the United States of America*, 109(45):18553–18558. [Cited on page 56]

Vyazovskiy, V. V., Olcese, U., Hanlon, E. C., Nir, Y., Cirelli, C., and Tononi, G. (2011). Local sleep in awake rats. *Nature*, 472(7344):443–447. [Cited on page 62]

Wachten, S., Masada, N., Ayling, L. J., Ciruela, A., Nikolaev, V. O., Lohse, M. J., and Cooper, D. M. F. (2009). Distinct pools of cAMP centre on different isoforms of adenylyl cyclase in pituitary-derived GH3B6 cells. *Journal of Cell Science*, 123(1):95–106. [Cited on page 47]

Wang, X. J., Golomb, D., and Rinzel, J. (1995). Emergent spindle oscillations and intermittent burst firing in a thalamic model: specific neuronal mechanisms. *Proceedings of the National Academy of Sciences of the United States of America*, 92(12):5577–5581. [Cited on pages 56 and 59]

Wang, X. J. and Rinzel, J. (1992). Alternating and Synchronous Rhythms in Reciprocally Inhibitory Model Neurons. *Neural computation*, 4(1):84–97. [Cited on page 99]

Wang, Z. and Rebec, G. V. (1993). Neuronal and behavioral correlates of intrastriatal infusions of amphetamine in freely moving rats. *Brain research*, 627(1):79–88. [Cited on page 36]

Weber, F. and Dan, Y. (2016). Circuit-based interrogation of sleep control. *Nature*, 538(7623):51–59. [Cited on pages 60, 102, 103, and 104]

Weber, F., Do, J. P. H., Chung, S., Beier, K. T., Bikov, M., Doost, M. S., and Dan, Y. (2018). Regulation of REM and Non-REM Sleep by Periaqueductal GABAergic Neurons. *Nature Communications*, 9(1), 354. [Cited on page 62]

Weyand, T. G., Boudreaux, M., and Guido, W. (2001). Burst and tonic response modes in thalamic neurons during sleep and wakefulness. *Journal of Neurophysiology*, 85(3):1107–1118. [Cited on pages 54 and 108]

Whittington, M. A., Traub, R. D., Kopell, N., Ermentrout, B., and Buhl, E. H. (2000). Inhibition-based rhythms: experimental and mathematical observations on network dynamics. *International Journal of Psychophysiology*, 38(3):315–336. [Cited on page 104]

Wickham, H. (2016). ggplot2: elegant graphics for data analysis. [Cited on page 124]

Wilkinson, L. (2011). The Grammar of Graphics. In *Handbook of Computational Statistics* (pp. 375-414). Springer Berlin Heidelberg, Berlin, Heidelberg. [Cited on page 124]

Wilson, M. A. and Bhalla, U. S. (1989). GENESIS: A system for simulating neural networks. *papers.nips.cc.* [Cited on page 122]

Wongsuphasawat, K., Qu, Z., and Moritz, D. (2017). Voyager 2: Augmenting visual analysis with partial view specifications. In G. Mark (ed.) Proceedings of the 2017 CHI Conference on Human Factors in Computing Systems (CHI'17). New York: ACM. [Cited on page 124]

Yamawaki, N., Stanford, I. M., Hall, S. D., and Woodhall, G. L. (2008). Pharmacologically induced and stimulus evoked rhythmic neuronal oscillatory activity in the primary motor cortex in vitro. *Neuroscience*, 151(2):386–395. [Cited on pages 37 and 38]

Yen, C. T., Conley, M., Hendry, S. H., and Jones, E. G. (1985). The morphology of physiologically identified GABAergic neurons in the somatic sensory part of the thalamic reticular nucleus in the cat. *The Journal of neuroscience*, 5(8):2254–2268. [Cited on page 119]

Ying, S.-W., Abbas, S. Y., Harrison, N. L., and Goldstein, P. A. (2006). Propofol block of Ih contributes to the suppression of neuronal excitability and rhythmic burst firing in thalamocortical neurons. *European Journal of Neuroscience*, 23(2):465–480. [Cited on page 64]

Yu, H.-G., Lu, Z., Pan, Z., and Cohen, I. S. (2004). Tyrosine kinase inhibition differentially regulates heterologously expressed HCN channels. *Pflugers Archiv - European Journal of Physiology*, 447(4):392–400. [Cited on page 51]

Zaccolo, M. (2011). Spatial control of cAMP signalling in health and disease. *Current Opinion in Pharmacology*, 11(6):649–655. [Cited on page 47]

Zaccolo, M., De Giorgi, F., Cho, C. Y., Feng, L., Knapp, T., Negulescu, P. A., Taylor, S. S., Tsien, R. Y., and Pozzan, T. (2000). A genetically encoded, fluorescent indicator for cyclic AMP in living cells. *Nature cell biology*, 2(1):25–29. [Cited on pages 47 and 50]

CURRICULUM VITAE